ARCHITECTURES AND ALGORITHMS FOR VOLTAGE CONTROL IN POWER DISTRIBUTION SYSTEMS

BY

BRETT ANDREW ROBBINS

DISSERTATION

Submitted in partial fulfillment of the requirements
for the degree of Doctor of Philosophy in Electrical and Computer Engineering
in the Graduate College of the
University of Illinois at Urbana-Champaign, 2015

Urbana, Illinois

Doctoral Committee:

Associate Professor Alejandro D. Domínguez-García, Chair
Professor Peter W. Sauer
Associate Professor Angelia Nedich
Assistant Professor Hao Zhu

ABSTRACT

In this thesis, we propose a hierarchical control architecture for voltage in power distribution networks where there is a separation between the slow time-scale, in which the settings of conventional voltage regulation devices are adjusted, and the fast time-scale, in which voltage regulation through active/reactive power injection shaping is accomplished. Slow time-scale devices will generally be existing hardware, e.g., voltage regulation transformers, which will be dispatched at appropriate time intervals to reduce the wear on their mechanical parts. In contrast, fast time-scale devices are considered to be devices that connect to the grid through power electronics, e.g., photovoltaic (PV) installations.

In the slow time-scale control, we propose a method to optimally set the tap position of voltage regulation transformers. We formulate a rank-constrained semidefinite program (SDP), which is then relaxed to obtain a convex optimization that is solved distributively with the Alternating-Direction Method of Multipliers (ADMM). In the fast time-scale control, we propose the following schemes: (i) a feedback-based approach to regulate system voltages, and (ii) an optimization-based approach that maintains the desired operating state through a quadratic program developed from a linear distribution system model.

Finally, we showcase the operation of the two time-scale control architecture in an unbalanced three-phase distribution system. The test system in the case studies is derived from the IEEE 123-bus test system and has a high penetration of residential PV installations and electric vehicles (EVs). We provide several examples that demonstrate the interaction between the two time-scales and the impact of the proposed control on component behaviors.

To my parents, Bruce and Carole

ACKNOWLEDGMENTS

First, and foremost, I would like to thank my advisor, Professor Alejandro D. Domínguez-García. Over the past 6 years, Alejandro has served as a great mentor and a driving force behind my academic endeavors. He has seemingly unlimited patience throughout the countless drafts of papers and debates over notation, all of which has transformed my approach to learning, writing, and expressing my ideas.

I would also like to thank my thesis committee: Peter Sauer, Hao Zhu, and Angelia Nedich. Professor Sauer has always been an unofficial advisor to me in my undergraduate, graduate, and professional careers. Professor Zhu was incredibly helpful in the development of the distributed optimization algorithms presented in Chapters 3 and 5. My discussions with Professor Nedich helped me to reconsider my approach to power flow formulation and served as the basis for Chapter 5.

No graduate school experience would be complete without my academic siblings: Sairaj Dhople, Stanton "Terry" Cady, Trevor Hutchins, Kai Van Horn, Christine Chen, and Raj Bhana. I can recall endless hours of homework and discussions that provided a number of breakthroughs that led me here.

Finally, I never would have made it here if it were not for my parents. While the last decade at the University of Illinois may have followed a more scenic route, their guidance and unconditional support kept me focused on my goals.

This work was supported in part by the National Science Foundation (NSF) under grant ECCS-1135598 and CAREER Award ECCS-CAR-0954420; by ABB under project "Distributed and Resilient Voltage Control of Distributed Energy Resources in the Smart Grid" (University of Illinois contract UIeRA 2013-2955-00-00); and by the Consortium for Electric Reliability Technology Solutions (CERTS).

TABLE OF CONTENTS

LIST OF TABLES

LIST OF FIGURES

CHAPTER 1

INTRODUCTION

In this chapter, we motivate the need to introduce the two time-scale control architecture for voltage control in power distribution systems proposed in this thesis. To help contextualize the work in the thesis, we provide some relevant background material and discuss previous work. Finally, we discuss the contributions of this work and outline the thesis.

1.1 Problem Statement

The electric power infrastructure has been recognized as the most important engineering achievement of the 20th century [1]. Modern power grids are faced with significant challenges in reliability, security, environment, sustainability, and market diversity. Driven by initiatives such as the US DOE *Smart Grid*, and its European counterpart *Electricity Networks of the Future*, power distribution systems are undergoing radical transformations in structure and functionality [2, 3]. Firstly, environmental concerns advocate high-penetration levels of variable renewable generation, such as photovoltaic (PV) installations and wind turbines. Secondly, for economic interests, the loads are being increasingly diversified, encompassing deferrable or storage-based loads, e.g., plug-in hybrid electric vehicles (PHEVs) or electric vehicles (EVs). These generation and storage resources are commonly referred to as distributed energy resources (DERs). Lastly, an unprecedented level of information flow and scheduling across the whole network is envisioned by capitalizing on state-of-the-art technologies in sensing, control, and communication.

To date, the relatively small penetration of DERs in distribution systems has allowed regulations pertaining to their control to be limited to (i) maintaining a constant power factor, (ii) following scheduled dispatches from an

operator, and (iii) disconnecting from the grid when a fault occurs [4]. However, it has been reported (see, e.g., [5,6]) that increased penetration of DERs in distribution systems is likely to cause voltage problems, thus requiring additional control mechanisms on top of conventional ones, e.g., tap-changing under load (TCUL) transformers. This is due to the fact that, unlike transmission systems, typical line reactance to resistance ratios in distribution systems are such that bus voltages are much more sensitive to changes in active power injections [7,8]. In this regard, PV-based electricity generation can be highly variable and ramp up on the order of 15% of its capacity per minute across a network with intermittent cloud cover [5]. Additionally, on a clear day, a high penetration of PV installations has the potential to cause voltage rise and over-voltages from a reversal of active power flow originating from net-positive power injections. With respect to this, the University of Illinois solar decathlon house—the *Gable Home* [9]—and the *Equinox* house [10] are examples of residential PV installations capable of producing an amount of power significantly larger than its average load during peak hours of the day. Similarly, the additional power demand introduced by large-scale charging of PHEVs can potentially cause unacceptable voltage drops [11].

Voltage regulation is traditionally handled by automatically-controlled TCUL transformers, set voltage regulators (SVR), and manually-controlled fixed/switched capacitors [5, 12, 13]. However, existing equipment is not inherently designed to handle the variability introduced by the DERs, and the lifetime of these components (e.g., the switches and tap changers) could be dramatically reduced due to the increased number of operations that they may undergo [5]. A potential solution to this problem is to supplement the existing control devices and utilize the DERs to provide reactive power support for voltage regulation through the proper control of the power electronics that interface them with the grid [14–16]. In this regard, the commercial products described in [16,17] are examples of existing rooftop and pole-mount PV solutions capable of providing reactive power support; these products have wireless communication capabilities that allow them to be controlled through cellular, Ethernet, or WiMax backhaul networks.

In order to address the voltage control problem in distribution systems, we envision a two time-scale architecture that classifies voltage control devices as either slow or fast time-scale actuators, with the idea of controlling them separately. Conventional voltage regulation devices, e.g., TCUL transform-

ers and switched capacitors, would be considered slow time-scale actuators, whereas power-electronic-interfaced DERs with reactive power provision capability would be the latter. Periodically, the slow time-scale control would dispatch the associated actuators, resulting in some voltage profile [18]. This can be performed based on heuristics associated with the time of day, or the system can be monitored for contingency cases, e.g., system voltages are outside of tolerances. Then, given that fast (and uncontrolled) changes in DER active generation (consumption) might cause the voltage to deviate from the voltage profile set by the slow time-scale optimization, a second optimization or a feedback control scheme executed at regular intervals (e.g., every minute) could be utilized to determine the active/reactive power settings of the DERs.

1.2 Background

In this section, we provide a brief overview of the power flow model of a three-phase system and fundamental concepts in optimization. The ensuing chapters will further develop these topics for their specific applications.

1.2.1 Power Flow Model

Distributions systems present a particular challenge, as compared to transmission systems, when we formulate the power flow problem. Unlike transmission systems, we cannot analyze the equivalent per-phase equivalent network of the balanced network, since the distribution line segments are not transposed and contain significant coupling between the phases. The imbalances are worsened further, since the network loads are generally not balanced and can be single-, two-, or three-phase loads.

Figure 1.1 shows the unbalanced three-phase distribution line segment circuit diagram between buses i and k. We measure the phase voltages with respect to ground so that the bus voltages will be $V_{a_i} = |V_i|\angle\theta_i$, $V_{b_i} = |V_i|\angle(\theta_i - 2\pi/3)$, and $V_{c_i} = |V_i|\angle(\theta_i + 2\pi/3)$ in the balanced case. The line impedance and admittance will be $\boldsymbol{z}_{ik}, \boldsymbol{y}_{ik} \in \mathbb{C}^{3\times 3}$, which are dense matrices and are not diagonally dominant. We also have the line charging (shunt capacitance) at each end of the line given by $\frac{1}{2}\boldsymbol{b}_{ik} \in \mathbb{C}^{3\times 3}$. The development of $\boldsymbol{z}_{ik}$, $\boldsymbol{y}_{ik}$, and $\boldsymbol{b}_{ik}$ based on the system parameters is given in [7].

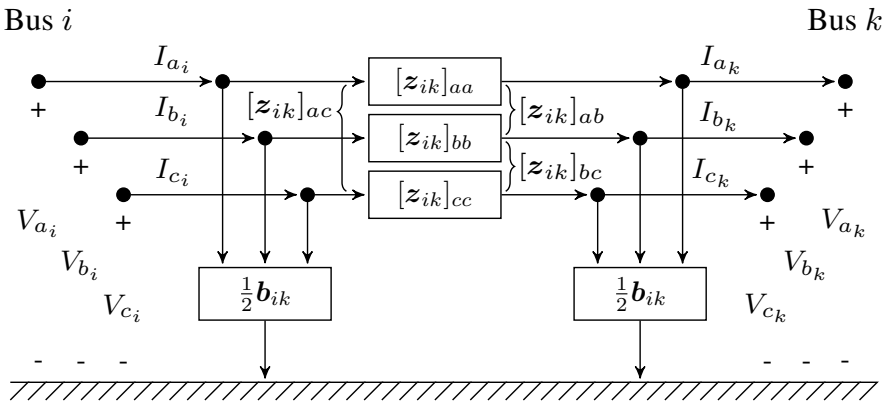

Figure 1.1: Three-phase transmission line segment.

Figure 1.2 shows the possible load configurations, which are connected between the phases in either a wye-connection or delta-connection in Figs. 1.2(a) and 1.2(b), respectively. For reasons that will be clearer later, we simplify the network to be entirely comprised of wye-connected loads. We can approximate the delta-connected loads with the following relationship:

$$\begin{bmatrix} S_a \\ S_b \\ S_c \end{bmatrix} = \frac{\sqrt{3}}{3} \begin{bmatrix} e^{-j\pi/6} & 0 & e^{-j5\pi/6} \\ -e^{-j5\pi/6} & e^{-j\pi/6} & 0 \\ 0 & -e^{-j5\pi/6} & e^{-j\pi/6} \end{bmatrix} \begin{bmatrix} S_{ab} \\ S_{bc} \\ S_{ca} \end{bmatrix}, \tag{1.1}$$

where we assume that the loads are constant power, and for numerical simulation purpose, we can initialize the loads based on an approximately balanced network. We can compute the power flowing out of bus i towards bus k as

$$\boldsymbol{S}_{i\to k} = \left(\boldsymbol{y}_{ik} \left(\boldsymbol{V}_i - \boldsymbol{V}_k \right) + \frac{1}{2} \boldsymbol{b}_{ik} \boldsymbol{V}_i \right)^* \odot \boldsymbol{V}_i, \tag{1.2}$$

where $\odot$ is the Hadamard product, e.g., the element-wise product of two matrices. Let $\mathcal{H}_i := \{i\} \cup \{k \,|\, (i,k) \in \mathcal{E}\}$ be the set of buses electrically connected to bus i. Then, we can compute the power flow at bus i as

$$\boldsymbol{S}_i^g - \boldsymbol{S}_i^d = \sum_{k \in \mathcal{H}_i} \boldsymbol{S}_{i\to k}, \tag{1.3}$$

where $\boldsymbol{S}_i^g$ and $\boldsymbol{S}_i^d$ are the complex power generation and load at bus i, respectively. The generation $\boldsymbol{S}_i^g$ includes the active power generated by the DERs, the reactive power contributions of shunt capacitors/inductions, and the reactive power support provided by controllable DERs.

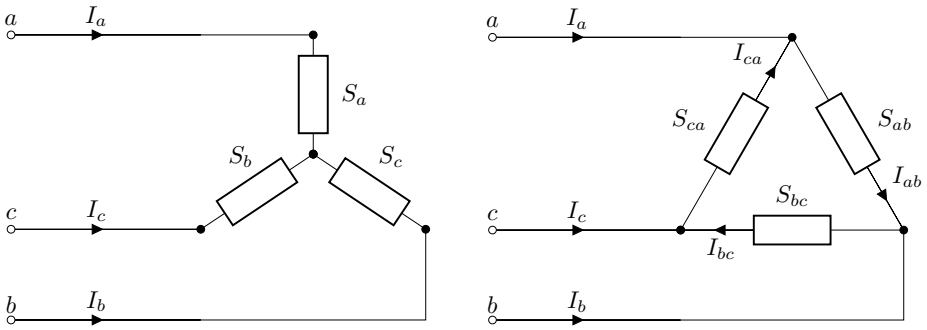

(a) Wye-connected load. (b) Delta-connected load.

Figure 1.2: Three-phase distribution system load configurations.

1.2.2 A Primer on Optimization

Throughout this thesis, we rely on a fundamental understanding of how to formulate an optimization problem and the relationship it has with its dual. Consider the equality-constrained convex optimization problem

$$\min_x f(x) \tag{1.4a}$$

such that

$$Ax = b, \tag{1.4b}$$

where $x \in \mathbb{R}^n$, $A \in \mathbb{R}^{m \times n}$, $b \in \mathbb{R}^m$, and $f : \mathbb{R}^n \to \mathbb{R}$. The objective function $f(x)$ represents some cost that we are attempting to minimize in terms of the optimization variables x, such that some algebraic constraints $Ax = b$ are met; e.g., we often minimize the system losses so that the power flow constraints of the network are satisfied.

Often, it is to our advantage to reformulate the constrained minimization problem as an unconstrained maximization problem and solve the so-called *dual* rather than the primal in (1.4). The *Lagrangian* is given by

$$\mathcal{L}(x, y) = f(x) + y^{\mathrm{T}} (Ax - b), \tag{1.5}$$

where $y \in \mathbb{R}^m$ is the dual variable that represents the penalty associated with violating a particular algebraic constraint. Then, we define the *Lagrangian Dual Function* as

$$g(y) = \inf_x \mathcal{L}(x, y) = -f^* \left(-A^{\mathrm{T}} y\right) - b^T y, \tag{1.6}$$

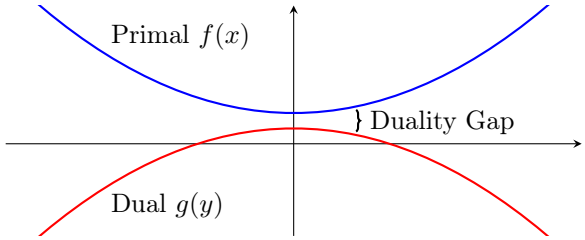

Figure 1.3: The relationship between the primal and dual functions.

where $f^*(w) = w^{\mathrm{T}}x - f(x)$, $w \in \mathbb{R}^n$ is the conjugate of the primal function $f(x)$. The dual function $g(y)$ will be a concave function whether or not the primal is convex and has the following property:

$$\max_y g(y) \leq \min_{x \in \mathcal{D}} f(x). \tag{1.7}$$

As shown in Fig. 1.3, the dual function will be a lower bound to the optimal value of the primal. However, if the primal is convex and strong duality holds, i.e., $f(x^*) = g(y^*)$ (the duality gap is zero), then we can solve for the dual and recover the primal solution with

$$x^* = \arg\min_x \mathcal{L}(x, y^*). \tag{1.8}$$

In an effort to improve robustness and the convergence of solving primal-dual problem without assumptions like strict convexity or the finiteness of $f(\cdot)$, the *Augmented Lagrangian* methods were developed. This approach incorporates an additional penalty term to the Lagrangian to become

$$\mathcal{L}_c(x, y) = f(x) + y^{\mathrm{T}}(Ax - b) + \frac{c}{2}\|Ax - b\|_2^2, \tag{1.9}$$

for some penalty parameter $c > 0$. Intuitively, if solving numerically, if we initialize far from the optimal solution, the penalty will drive the solver. As we reach the optimal solution, the penalty will become negligible and we solve for the original dual problem $g(y)$. We refer the reader to [19, 20] for further discussion on the benefits and convergence properties of the augmented Lagrangian.

1.3 Related Work

The control and optimization of DERs is generally broken down into three different categories: (i) centralized, (ii) distributed, and (iii) local (decentralized) schemes. In this thesis, we advocate the use of distributed control architectures. These control architectures offer many potential benefits over centralized ones: (i) they are more economical because they do not require a significant communication infrastructure overlay, (ii) computational requirements for the local controller are relatively low, and (iii) local information is sufficient to control the DERs. Furthermore, the proposed distributed architectures can be implemented on a single processor or parallelized across several processors to reduce the problem size and reduce the computational time in a centralized scheme.

Many (centralized) solutions to the voltage control problem in distribution networks have been proposed in [21–23]. For example, the authors in [21] propose an optimal multi-agent scheme that provides reactive power support in distribution feeders, and assumes that DERs have two-way communication with a single controller, either directly or through other DERs. In order to correct limit violations, agents are assigned to be managers or contractors that bid on reactive power contributions based on bus sensitivities. In [22], the authors partition the system buses into groups (agents) and solve local optimal power flow problems though a hierarchical chain of command structure. The authors in [23] maintain a database of limited historical observations and the corresponding solutions to a nonlinear optimal power flow problem, so as to avoid computing its solution each time.

Recently, centralized-based methods include branch flow formulations [24–26], second-order cone program (SOCP) [24, 27], and rank-relaxed semidefinite program (SDP) formulations (see e.g., [18, 28–30] and the references therein). Lately, rank-relaxed SDP-based formulations have gathered significant attention. While this approach is not guaranteed to provide a global minimum, e.g., it can fail for tightly constrained mesh networks, it has been shown that the solution to the SDP-based optimal power flow (OPF) will return a rank-1 solution for tree-structure networks under some mild conditions [29,31,32]; these structures are typical of radial distribution systems. In this case, the SDP-approach guarantees a global minimum. Then, the convex OPF can be solved with either a subgradient- or ADMM-based (Alternating

Direction Method of Multipliers) distributed algorithm [18, 29, 30, 33].

There are also several decentralized and distributed strategies that address the voltage regulation problem in distribution networks [34, 35]. The authors of these works propose a switching control scheme where the DERs are operated with a constant power factor while bus voltages are within specifications. Then, whenever there is a voltage violation, their reactive power is adjusted so that the system returns to the desired operating conditions. Otherwise, DERs can be controlled through a local scheme that consists of a local feedback controller [36, 37], or policies that are designed to maintain grid reliability [4].

1.4 Contributions and Organization of the Thesis

In this section, we provide an overview of the remaining chapters, and we discuss the main contributions of the thesis.

Chapter 2. We describe our proposed hierarchical control architecture in which we perform separate optimizations for the slow and fast time-scale control of the system devices. Slow time-scale devices will generally be existing hardware that will be dispatched at appropriate time intervals to reduce the wear on their mechanical parts. In contrast, fast time-scale devices are considered to be devices that connect to the grid through power electronics and will be used to mitigate the variability introduced by the DERs and flatten the voltage profile of the distribution network. We provide a high-level overview of the optimization and feedback control methods proposed in this thesis.

The work presented in this chapter was published in [38], and [39].

Chapter 3. In the context of the slow time-scale devices, we propose a method to optimally set the tap positions of the voltage regulation transformers in distribution systems. We cast the problem as a rank-constrained semidefinite program, in which the transformer tap ratios are captured by (i) introducing a secondary-side 'virtual' bus per transformer, and (ii) constraining the values that these virtual bus voltages can take according to the limits on the tap positions. Then, by relaxing the non-convex rank-1 constraint in the rank-constrained SDP formulation, one obtains a convex

SDP problem. The tap positions are determined as the ratio between the primary-side bus voltage and the secondary-side virtual bus voltage that result from the optimal solution of the relaxed SDP, which are then rounded to the nearest discrete tap values. To efficiently solve the relaxed SDP, we propose an ADMM-based distributed algorithm.

The work presented in this chapter was published in [18] and [40].

Chapter 4. In the context of the fast time-scale devices, we propose a decentralized feedback architecture for voltage regulation in distribution networks that relies on controlling reactive power injections provided by the DERs. A local controller on each bus of the network monitors the bus voltage and, whenever there is a voltage violation, it uses locally available information to estimate the amount of reactive power that needs to be injected into the bus in order to correct the violation. If the DERs connected to the bus can collectively provide the reactive power estimated by the local controller, they are instructed to do so. Otherwise, the local controller initiates a request for additional reactive power support from other controllers at neighboring buses through a distributed algorithm that relies on a local exchange of information among neighboring controllers. We show that the proposed architecture helps prevent voltage violations and shapes the voltage profile in radial distribution networks, even in the presence of considerable penetration of variable generation and loads.

The work presented in this chapter was published in [36].

Chapter 5. In the context of the fast time-scale devices, we propose a method to optimally set the reactive power contributions of the DERs present in distribution systems with the goal of regulating bus voltages. For the case when the network is balanced, we use the branch power flow modeling approach for radial power systems to formulate an OPF. Then, we leverage properties of the system operating conditions to relax certain nonlinear terms of this OPF, which results in a convex quadratic program (QP). To efficiently solve this QP, we propose a distributed algorithm that follows the ADMM-based approach introduced in Chapter 3. Furthermore, we include the unbalanced three-phase formulation to extend the ideas introduced for the balanced network case.

The work presented in this chapter was published in [41].

Chapter 6. In order to accurately simulate a distribution network, we develop aggregate load models for the system buses, define the active power injections of PV installations, and provide the uncontrolled/optimized EV charging schedules. Then, we incorporate the results from Chapters 2–5 to implement the two time-scale control architecture described in Chapter 2. We provide several scenarios to demonstrate the interaction between the slow and fast time-scale controls, as well as possible strategies to control the network to satisfy utility and customer control objectives.

The work presented in this chapter was published in [38] and [39].

Chapter 7. In the final chapter, we review the contributions made by this thesis. We also include insights and suggestions for future research directions.

CHAPTER 2

CONTROL ARCHITECTURE

In this chapter, we propose a hierarchical control architecture where there is a time-scale separation between the actions taken to determine the settings of conventional voltage regulation devices and the actions by which voltage regulation through reactive power injection shaping is accomplished. We provide a high-level overview of the proposed control architectures and include a bus-level reactive power management scheme.

2.1 Introduction

The introduction of distributed energy resources (DERs), e.g., plug-in hybrid electric vehicles (PHEVs) and photovoltaic (PV) installations, in distribution systems results in operational scenarios that these systems were not designed to handle. It has been reported (see, e.g., [5, 6]) that increased penetration of DERs in distribution systems is likely to cause voltage problems, thus requiring additional control mechanisms. This is due to the fact that, unlike transmission systems, typical line reactance to resistance ratios in distribution systems are such that bus voltages are much more sensitive to changes in active power injections [7, 8]. In this regard, existing equipment is not inherently designed to handle the variability introduced by DERs, and the lifetime of these components (e.g., the switches and tap changers) could be dramatically reduced due to the increased number of operations that they may undergo [5].

The current control of DERs is limited in the sense that these devices generally do not provide reactive power for voltage regulation, and they operate with local policies designed to protect the grid during severe operating conditions [4]. Interestingly, by properly controlling the power electronic grid interfaces of these DERs, they can provide reactive power support for

voltage regulation; thus, they help to mitigate the variability introduced by uncontrolled active power injections of certain types of DERs, e.g., PV installations [42]. While the proper control of the DERs is important, the coordinated efforts of conventional regulation hardware with the reactive power support supplied by the DERs provide a more complete and realistic control architecture [29, 43, 44].

2.2 Two Time-Scale Architecture

The objective of the thesis is to address the problem of voltage regulation in power distribution networks with substantial penetration of DERs; specifically, the focus is on the problem of mitigating voltage variability across the network due to fast (and uncontrolled) changes in the active power generated/consumed by DERs. To this end, we rely on the use of the power electronics interfaces of the DERs to locally provide some limited amount of reactive power. In other words, we have a limited ability to shape the active/reactive power injection profile. With respect to this, it is important to note that this ability to shape the active/reactive power injection profile, which in turn will allow us to regulate voltage across the network, is intended to supplement the action of conventional voltage regulation devices (e.g., tap-changing under-load transformers, set voltage regulators, and fixed/switched capacitors).

In practice, in order to realize the ideas above, we categorize devices as operating on either a slow or fast time-scale and control them separately. Conventional voltage regulation devices, e.g., tap-changing under load (TCUL) transformers, would be considered slow time-scale actuators, and devices with power-electronic interfaces would be considered fast time-scale actuators. We routinely perform a slow time-scale optimization to dispatch transformers and set the reference voltage that we regulate to based on the current operating conditions. This optimization is performed at regular time intervals or triggered by when some conditions are met. Then, given that fast (and uncontrolled) changes in the active generation (consumption) of the DERs might cause the voltage to deviate from this reference voltage, a second optimization or feedback control is performed at regular intervals, e.g., every minute. The time-scale separation between instances at which the set-

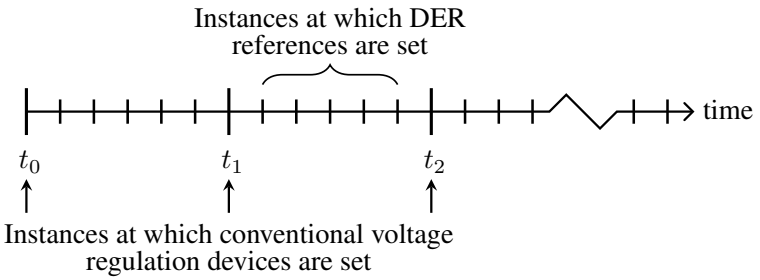

Figure 2.1: Time-scale separation between instances at which the settings of conventional voltage regulation devices are decided and the references of DERs are set.

tings of conventional devices are decided and the reference setting of DERs is graphically depicted in Fig. 2.1. The solution of this minute-by-minute optimization will provide the amount of reactive power that needs to be locally produced or consumed to track the voltage reference. In other words, the minute-by-minute optimization provides the reference values for the amount of reactive power to be collectively provided (or consumed) on each bus of the network within the next minute by reactive-power-capable DERs. These reference values are then passed to the local controllers of the DERs, which will adjust their output accordingly—note that the time-scale in which DER local controllers act (on the order of milliseconds) is much faster than the minute-to-minute optimization.

With respect to the framework described above, the slow time-scale optimization corresponds to selecting the settings of conventional devices, e.g., the tap ratios in the TCUL transformers, while the fast time-scale control adjusts the reactive power output of the DERs. As an illustrative example, Figure 2.2(a) shows the uncontrolled voltage profile for the buses plotted per phase relative to the distance from the feeder with the taps on the TCUL transformer in the neutral position and no reactive power support. In Fig. 2.2(b) we track a nominal 1 p.u. voltage magnitude with the transformer taps acting as the optimization variables. Finally, in Fig. 2.2(c) we include reactive power support along with the transformer taps in the optimization.

Next, we provide a high-level description of the control and optimization methods developed in the thesis.

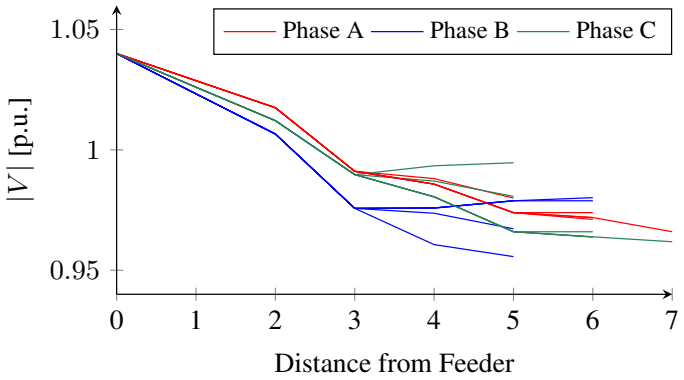

(a) Uncontrolled voltage profile.

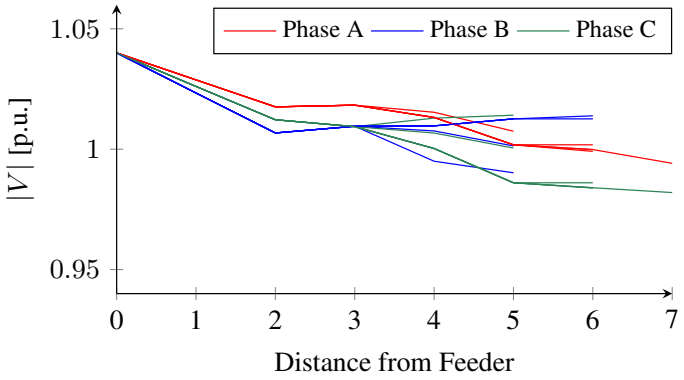

(b) Transformer taps optimized to track 1 p.u.

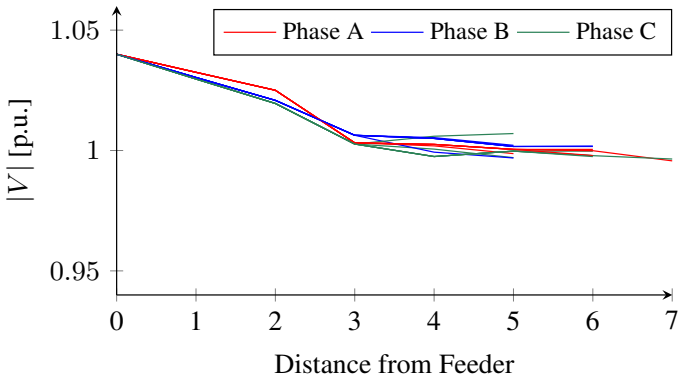

(c) Transformer taps and reactive power support optimized to track 1 p.u.

Figure 2.2: Unbalanced three-phase distribution system voltage profiles.

2.2.1 Slow Time-Scale Control

The intended purpose of the slow time-scale optimization is to (i) set the taps on the TCUL transformers, and (ii) determine a voltage profile V^r that meets some performance criteria for the fast time-scale control to regulate to. Periodically, we will redispatch the system with the slow time-scale optimization based on heuristics or monitoring for contingency cases, i.e., system voltages are outside of specification or resources are operating near their limits.

Let V denote the vector of bus voltages, a the vector of the turn ratios of the TCUL transformers, and $\tilde{q}$ the vector of the reactive power support provided by the DERs and shunt elements, which we will describe in more detail in Section 2.3. Then, for some operational objective function $C(V, a, \tilde{q})$, the slow time-scale optimization will have the form:

$$\min_{V,\, a,\, \tilde{q}} C(V, a, \tilde{q}) \tag{2.1a}$$

such that

$$\text{power flow as a function of } V,\ a, \text{ and } \tilde{q}, \tag{2.1b}$$

and

$$\text{voltage limits } \underline{V},\ \overline{V} \text{ on } V, \tag{2.1c}$$

$$\text{tap limits } \underline{a},\ \overline{a} \text{ on } a, \tag{2.1d}$$

$$\text{reactive power limits } \underline{q}^r,\ \overline{q}^r \text{ on } \tilde{q}, \tag{2.1e}$$

where we use different reactive power limits than those in the fast time-scale voltage regulation problem. We limit the amount of reactive power available in the slow time-scale optimization to provide what is equivalent to a spinning reserve in transmission systems, i.e., we do not want the DERs operating at full capacity with the initial dispatch so there is headroom to regulate up if necessary.

2.2.2 Fast Time-Scale Control

Fast time-scale devices are considered to be devices that connect to the grid through power electronics and have reactive power provision capabilities. We will leverage these devices to combat the variability introduced by the

DERs and meet system specifications throughout the distribution network. In this thesis, we perform the fast time-scale control either through a feedback control scheme or an optimization-based regulation procedure.

Feedback-Based Control

Figure 2.3 shows the closed-loop feedback control strategy we develop in Chapter 4 for tackling the voltage regulation problem. In this method, the discrete controllers independently attempt to regulate the bus voltage where they are located to V^r. In the situation that the controller fails to correct the bus voltage to within some tolerance around V^r, e.g., its local devices are at their reactive power limits, then we offer a secondary distributed control algorithm to supplement the decentralized feedback control. Note that we can keep the feedback control strictly decentralized by fixing the output of the secondary control to $\eta = 0$.

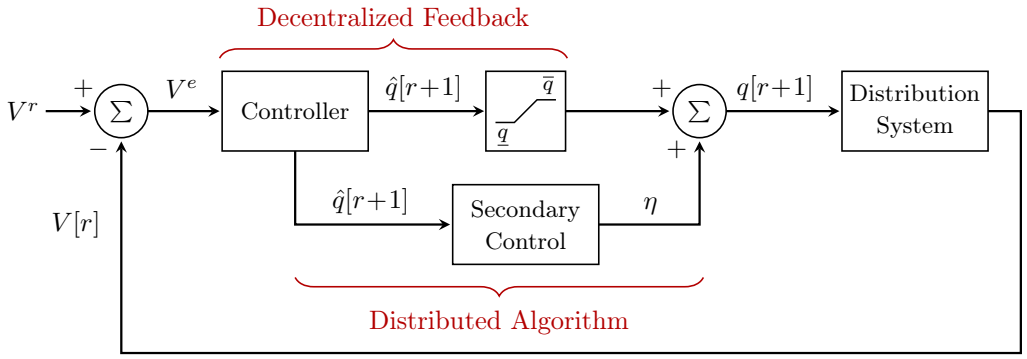

Figure 2.3: Proposed feedback control architecture.

Optimization-Based Control

Next, we consider an optimization-based approach to tackle the voltage regulation problem. The feedback-based control is simple to implement and requires very little knowledge of the system; however, correcting bus voltages with reactive power support is inherently a local problem, and the secondary control that supplements the feedback controller allocates reactive power requests based on limits and not location. Thus, an optimization-based control is well motivated.

The cost function $C(V, q)$ regulates the system voltages to the slow time-scale reference voltage, V^r, by penalizing the deviation of V from V^r. In this case, we formulate a quadratic program (quadratic objective with linear constraints) and the optimization will have the form:

$$\min_{V,\,q} C(V, q) \tag{2.2a}$$

such that

$$\text{power flow as a function of } V \text{ and } q, \tag{2.2b}$$

and

$$\text{reactive power limits } \underline{q},\, \overline{q} \text{ on } q, \tag{2.2c}$$

where $\underline{q}$ and $\overline{q}$ are the reactive power limits without considering reserve capacity for up and down regulation as in the slow time-scale optimization.

2.3 Bus-Level Reactive Power Management

In subsequent chapters, we assume that the local controller on each bus has aggregate information on the total reactive power capacity available from DERs connected to its bus, and it is responsible for reporting their reactive power limits to the high-level control and dispatching the reactive power request to the devices attached to them. This collective upper (lower) capacity limit is determined by the sum of the individual DER upper (lower) limits, which the local controller needs to obtain. In practice, this can be accomplished in a variety of ways. One possibility is to have the local controller directly communicate with each individual DER. In such a case, each DER can directly report its individual capacity limits, which can vary over time depending on the specific operating conditions of the DER. An alternative to the above approach can be implemented using a distributed algorithm that coordinates the DERs on each bus in a distributed fashion [45, 46].

Figure 2.4 shows the intended communication structure at the bus level between the local controller and the devices with reactive power provision capabilities located on bus i. We categorized the devices as either: (i) discrete shunt elements, i.e., shunt capacitors or inductors, and (ii) customer-owned power-electronic-based DERs with reactive power provision capabilities. The

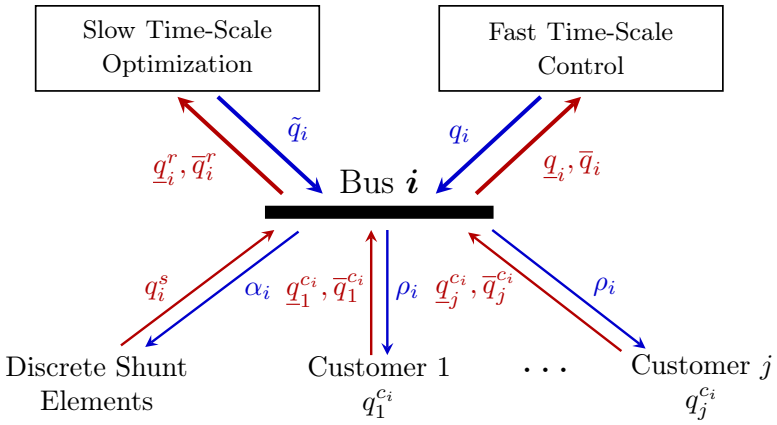

Figure 2.4: Information flow for the reactive power management at bus i.

discrete shunt elements will have some incremental reactive power value Δq_i^s p.u. that can be regulated up or down by $\alpha_i := \{\alpha_i \in \mathbb{Z} \,|\, \alpha_i \in [\underline{\alpha}_i, \overline{\alpha}_i]\}$ so that the total reactive power supplied by the shunt elements is

$$q_i^s = \alpha_i \left(\Delta q_i^s\right). \tag{2.3}$$

If the shunt elements are exclusively switched capacitors, then we have $\underline{\alpha}_i, \overline{\alpha}_i \geq 0$. In the case that we have shunt inductors, then $\underline{\alpha}_i < 0$ since inductors are perceived as added load.

Each customer j attached to bus i will supply $q_j^{c_i}$ p.u. of reactive power and their limits will be $\underline{q}_j^{c_i} \leq 0$ and $\overline{q}_j^{c_i} \geq 0$ for their net load and injections, respectively. In this thesis, we assume that the collective reactive power capability of the customers is greater than or equal to the incremental reactive power Δq_i^s of the shunt components, e.g., $\Delta q_i^s \leq \sum_j |\underline{q}_j^{c_i}|$ and $\Delta q_i^s \leq \sum_j \overline{q}_j^{c_i}$. Consequently, this implies that the aggregate reactive power support $\tilde{q}_i$, q_i provided by bus i is considered a continuous variable. There are a number of other conditions that can be considered for the control of the discrete shunt elements, i.e., limits on the number of switching actions; however, this is handled by updating the interval $[\underline{\alpha}_i, \overline{\alpha}_i]$ that defines α_i and effectively shifts the limits $\underline{q}_i, \overline{q}_i$ used in the optimizations.

Algorithm 1 outlines the dispatch procedure for the reactive power management by the local controller. First, we determine the contributions of the shunt elements based on the demand from the slow and fast time-scale controls. Then, we compute the customers' contributions that satisfy the remaining demand with the fair-splitting algorithm in Chapter 4, which de-

Algorithm 1: Bus i Reactive Power Management Control Scheme

Input : q_i
Output: α_i, ρ_i
Data: $\underline{\alpha}_i$, $\overline{\alpha}_i$, $\underline{q}_1^{c_i}$, $\ldots$, $\underline{q}_j^{c_i}$, $\overline{q}_1^{c_i}$, $\ldots$, $\overline{q}_j^{c_i}$
begin
initialize limits:

$$\underline{q}_i = \underline{\alpha}_i q_i^s + \sum_j \underline{q}_j^{c_i} \quad \text{and} \quad \overline{q}_i = \overline{\alpha}_i q_i^s + \sum_j \overline{q}_j^{c_i}$$

if $q_i \leq \underline{q}_i$ **then**
compute:

$$\alpha_i = \underline{\alpha}_i \quad \text{and} \quad \rho_i = -1$$

if $q_i \geq \overline{q}_i$ **then**
compute:

$$\alpha_i = \overline{\alpha}_i \quad \text{and} \quad \rho_i = 1$$

if $q_i < 0$ **then**
compute:

$$\alpha_i = \max\left(\underline{\alpha}_i, \left\lfloor \frac{q_i}{q_i^s} \right\rfloor\right) \quad \text{and} \quad \rho_i = -\frac{q_i - \alpha_i q_i^s}{\sum_j \underline{q}_j^{c_i}}$$

if $q_i \geq 0$ **then**
compute:

$$\alpha_i = \min\left(\overline{\alpha}_i, \left\lfloor \frac{q_i}{q_i^s} \right\rfloor\right) \quad \text{and} \quad \rho_i = \frac{q_i - \alpha_i q_i^s}{\sum_j \overline{q}_j^{c_i}}$$

return : α_i, ρ_i

termines the ratio ρ_i between demand and the available resources [42]. The reactive power commitment for each customer will be

$$q_j^{c_i} = \begin{cases} \rho_i \, \underline{q}_j^{c_i}, & \rho_i \leq 0, \\ \rho_i \, \overline{q}_j^{c_i}, & \rho_i > 0, \end{cases} \qquad \forall j, \tag{2.4}$$

and reactive power supplied by bus i will be

$$q_i = \alpha_i \left(\Delta q_i^s\right) + \sum_j q_j^{c_i}, \tag{2.5}$$

for the fast time-scale control, and similarly for $\tilde{q}_i$ for the slow time-scale optimization.

2.4 Summary

In this chapter, we provided a high-level overview of our proposed hierarchical control architecture. In Chapter 3, we formulate the optimization problem corresponding to the control of slow time-scale actuators and introduce the distributed solver that will be used throughout the thesis. Next, we describe the decentralized feedback control for the fast time-scale actuators to track the specified voltage profile from the solution to the OPF in Chapter 4. The distributed resource allocation algorithm presented in this chapter provides both a secondary control to assist the voltage regulation and dispatch reactive power at the bus level in Section 2.3. In Chapter 5, we introduce an optimal approach to handle the voltage regulation in the fast time-scale control. Finally, we demonstrate the operation of the two time-scale architecture in Chapter 6.

CHAPTER 3

SLOW TIME-SCALE: AN OPTIMIZATION-BASED APPROACH

In this chapter, we formulate an optimization problem for dispatching voltage regulation transformers (slow time-scale devices). This problem is then recast as a rank-constrained semidefinite program (SDP), which we make convex by dropping the rank constraint. This allows us to solve the problem centralized or in parallel with a distributed architecture or a central computer with a large number of cores. We can also leverage the distributed solver presented in this chapter to reduce the problem algebraically in the centralized solution.

3.1 Introduction

In power distribution systems, tap-changing under-load (TCUL) transformers are commonly used for regulating voltage. Traditionally, automatic voltage regulators (AVRs) are utilized to control the transformer tap position based on local voltage measurements (see e.g., [47, 48]). While this AVR-based control is effective in achieving local voltage regulation, it is likely not optimal in terms of achieving certain overall system operational objectives, e.g., minimizing power losses and voltage regulation from some reference value. Motivated by this, we propose a framework to determine the transformer tap ratios in distribution systems that is optimal in some sense.

To address the problem described above, we formulate an optimal power flow (OPF), where the transformer tap ratios are included as decision variables and the objective is to minimize the total power losses (although, other objectives can be accomplished as well). In the context of transmission systems, optimal transformer tap setting under the OPF framework has been investigated for decades. For example, in [49], the transformer tap positions are included as discrete variables in the OPF problem, which results in a mixed-integer program (MIP) formulation. Unfortunately, the compu-

tational complexity of this formulation grows exponentially with the number of transformers, and thus becomes intractable for large systems. To tackle this complexity issue, several papers have proposed to relax transformer tap positions to continuous optimization variables, and then round the solution to the closest discrete variables (see e.g., [49–51]). This alternative approach can yield acceptable performance without incurring the added complexity. However, all of these approaches are restricted to standard OPF formulations, and are known to potentially suffer from the same convergence issues present in traditional iterative solvers.

We formulate the OPF problem that arises in the context of voltage regulation in distribution systems as a rank-constrained semidefinite program (SDP), and subsequently obtain a convex SDP problem from the original SDP formulation by dropping the only non-convex rank-1 constraint (see, e.g., [29, 31, 32, 52]). In general, this rank relaxation is not guaranteed to attain the global minimum, in particular for mesh networks. Interestingly, it has been shown that under some mild conditions, the optimal solution for the relaxed SDP-based OPF problem turns out to be of rank 1 for tree-structured networks, which are typical of radial distribution systems [29,31,32]. In this sense, the rank relaxation scheme is actually guaranteed to attain the global optimum of the original OPF problem. In addition to handling the OPF problem, the SDP-based approach also constitutes a very promising tool to tackle the non-convexity in other monitoring and control applications in power distribution systems.

It is possible to extend the SDP-based OPF approach to include the tap ratios of TCUL transformers by introducing a virtual secondary-side bus per transformer, which in turn will result in additional constraints and decision variables [40,53,54]. However, the TCUL transformer model proposed in [54] is limited due to two issues: (i) the resulting relaxed SDP problem could fail to yield a rank-1 solution, and thus its global optimality is no longer guaranteed; and (ii) it is only applicable to balanced systems. The first issue arises since the network is equivalently broken into two disconnected parts by introducing virtual buses associated to each transformer, and the network disconnection would lead to multiple solutions of rank 2 [40]. Although an optimal rank-1 solution could be recovered in this case, the conditions for recovering rank-1 solutions are only possible for balanced systems [40, 54]. As for the second issue, it is well known that distribution systems are unbalanced;

this motivates the formulation of the three-phase OPF problem [52]. As will become more clear later on, it is impossible to enforce the phase separation between the primary- and secondary-side buses for the transformer model in [54]. To address this issue, we propose an alternative transformer model by including a highly resistive line between the primary- and secondary-side buses. The proposed method does not introduce additional complexity as compared to [54], but can successfully resolve the two aforementioned issues. Related to our approach, [55] and [28] discuss adding a very small resistance term to the model to handle a similar network disconnection issue due to the presence of ideal transformers. It is worth pointing out that such a method will maintain phase angles between primary- and secondary-side buses, but will return incorrect power transfers; hence it is not deemed effective for modeling transformers.

In order to solve the relaxed SDP problem described earlier, rather than using iterative solvers traditionally used to solve the OPF problem, we are interested in fast distributed solvers to handle the higher computational complexity introduced by the SDP formulation. Distributed methods for solving the OPF problem have been proposed in power systems in a variety of contexts (see, e.g., [29, 52, 56] and the references therein). In particular, the Alternating-Direction Method of Multipliers (ADMM) has been widely used as a simple, yet powerful technique for solving distributed convex optimization problems [20]. This method has been successfully applied in power systems for the dispatch of distributed generation and deferrable loads [52, 56], as well as state estimation [57]. We leverage the ADMM to solve the relaxed SDP-based optimal tap problem in a distributed fashion. The ability to perform the optimization tasks in parallel can dramatically reduce computation time and complexity, especially for large-scale systems [56].

The remainder of this chapter is organized as follows. Section 3.2 introduces the system model and formulates the transformer tap-setting optimization problem. In Section 3.3, we rewrite the OPF as a convex SDP, and introduce a modified transformer model that will allow us to extend this framework to an unbalanced three-phase system. The distributed solver is given in Section 3.4. Section 3.5 presents the case studies, and concluding remarks are presented in Section 3.6.

3.2 Problem Formulation

In this section, we first introduce the standard TCUL transformer model in the literature. Then, we describe the power flow formulation adopted in this chapter and formulate the per-phase optimal power flow (OPF) problem that includes the transformer tap positions as decision variables for balanced systems.

3.2.1 Standard Transformer Model

Figure 3.1(a) shows the standard model of the t^{th} TCUL transformer located on the distribution line segment (p_t, s_t) of some power distribution system. Without loss of generality, we assume that the primary side of the transformer is closest to the feeder head, and the admittance for the attached distribution line segment(s) and core losses (which are typically ignored in distribution systems [47,58]) are referred to the secondary side as $y_{p_t s_t}$. Given the tap ratio a_t, this model contains an *ideal* transformer directly connected to bus p_t and the virtual secondary-side bus s'_t such that $V_{p_t} = a_t V_{s'_t}$. The

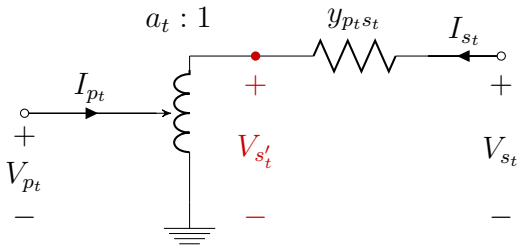

(a) Classical transformer model.

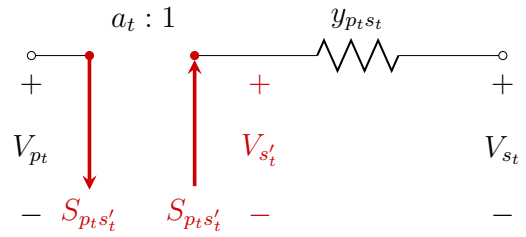

(b) Equivalent transformer model.

Figure 3.1: Tap-changing under load transformer models.

tap ratio a_t is a discrete variable that typically takes on 33 possible values $\{\tilde{a}_{-16}, \ldots, \tilde{a}_0, \ldots, \tilde{a}_{16}\}$, uniformly distributed around $\tilde{a}_0$ to create a specified range around the rated voltage of the transformer (which corresponds to $\tilde{a}_0$). For instance, the taps can move up and down 16 positions from the nominal tap ratio $\tilde{a}_0 = 1$ with each step corresponding to 5/8% p.u. change. With the typical nominal voltage at 1 p.u., the tap ratio is bounded by $\underline{a} = \tilde{a}_{-16} = 0.9$ and $\overline{a} = \tilde{a}_{16} = 1.1$ [48]. Then, the line current and bus voltage relationships for the circuit in Fig. 3.1(a), which depend nonlinearly on the tap ratio, are as follows:

$$\begin{bmatrix} I_{p_t} \\ I_{s_t} \end{bmatrix} = \begin{bmatrix} y_{p_t s_t}/a_t^2 & -y_{p_t s_t}/a_t \\ -y_{p_t s_t}/a_t & y_{p_t s_t} \end{bmatrix} \begin{bmatrix} V_{p_t} \\ V_{s_t} \end{bmatrix}. \tag{3.1}$$

Figure 3.1(b) shows an equivalent model to the one in Fig. 3.1(a) that removes the *ideal* transformer entirely and augments the network with the virtual bus s'_t. We treat the buses p_t and s'_t as though they are electrically disconnected and introduce an additional variable $S_{p_t s'_t}$ to account for the power transferred across the removed ideal transformer, e.g., buses p_t and s'_t will have a net injection of $-S_{p_t s'_t}$ and $S_{p_t s'_t}$, respectively. Unlike the model in (3.1), the primary/secondary power is independent of the tap ratio. The key advantages of this alternative model are that: (i) the tap ratio is only necessary in order to define the secondary-side bus voltage: $V_{s'_t} = V_{p_t}/a_t$, and (ii) the admittance matrix for the equivalent circuit will remain constant. Hence, in subsequent developments, we will use the primary/secondary power relationship of the alternative transformer model in Fig. 3.1(b). Note that transformers with fixed turn ratios are easily incorporated by modifying the admittance matrix Y as described by (3.1).

3.2.2 Power System Model

Consider an $n+1$ bus power system that has r TCUL transformers. Let $\mathcal{T} := \{1, \ldots, r\}$ denote the set of transformers. The set of buses incident to the primary-side of a transformer is defined as $\mathcal{N}_p := \{p_t \,|\, t \in \mathcal{T}\}$; similarly, for buses incident to the secondary side of a transformer, we have that $\mathcal{N}_s := \{s_t \,|\, t \in \mathcal{T}\}$. Additionally, the set of virtual buses (introduced in the equivalent transformer model in Fig. 3.1(b)) is defined as $\mathcal{N}_{s'} := \{s'_t \,|\, t \in \mathcal{T}\}$. We index the feeder by 0 and let the remaining m system buses belong to

the set $\mathcal{N}_b := \{1, \ldots, m\}$. Thus, the set of physical buses will be

$$\mathcal{N} = \mathcal{N}_b \cup \mathcal{N}_p \cup \mathcal{N}_s, \tag{3.2}$$

and the set of buses in the augmented network created by adding the virtual buses is

$$\mathcal{N}_a = \mathcal{N} \cup \mathcal{N}_{s'}, \tag{3.3}$$

where $|\mathcal{N}_a| = n + r$.

The edge-set describing all of the distribution line segments in the system (which could contain conductors for single-, two-, or three-phase circuits) is $\mathcal{E}_a \subseteq \{\mathcal{N}_a \cup \{0\}\} \times \{\mathcal{N}_a \cup \{0\}\}$ such that $(i,k) \in \mathcal{E}_a$ is the distribution line between buses i and k. The admittance matrix for the balanced network $Y \in \mathbb{C}^{(n+r+1)\times(n+r+1)}$ will reflect the topology of the augmented network. Furthermore, we define the set $S_{ps'} := \{S_{p_t s'_t} \,|\, t \in \mathcal{T}\}$ as the power transferred through the transformers. This balanced model will be extended to the general unbalanced three-phase case in Section 3.3.4.

Finally, in order to include the equivalent transformer model in Fig. 3.1(b), the power flow equations will be formulated depending on the type of bus as follows:

No Transformer Incident to a Bus
Consider the case when there are no transformers incident to bus i. Let $\mathcal{H}_i := \{i\} \cup \{k \,|\, (i,k) \in \mathcal{E}_a\}$ be the set of buses electrically connected to bus i, which has no transformers incident to it. Then, the power injected in bus i is

$$S_i = S_i^g - S_i^d = \sum_{k \in \mathcal{H}_i} [Y^*]_{ik} V_i V_k^*, \qquad \forall i \in \mathcal{N} \backslash \mathcal{N}_p, \tag{3.4}$$

where the generation S_i^g and load S_i^d are referenced as positive quantities.

Transformer Incident to a Bus
As shown in Fig. 3.1(b), we track the power across the transformer via $S_{p_t s'_t}$, and capture the tap ratio with the voltage relationship $V_{s'_t} = V_{p_t}/a_t$. If bus i is incident to the primary-side of a transformer, then the corresponding power flow equation becomes

$$S_{p_t} - S_{p_t s'_t} = \sum_{k \in \mathcal{H}_{p_t}} [Y^*]_{p_t k} V_{p_t} V_k^*, \qquad \forall t \in \mathcal{T}, \tag{3.5}$$

or, for the virtual secondary-side bus, we have that

$$S_{p_t s'_t} = \sum_{k \in \mathcal{H}_{s'_t}} [Y^*]_{s'_t k} V_{s'_t} V_k^*, \qquad \forall t \in \mathcal{T}. \tag{3.6}$$

Note that the secondary-side buses in $\mathcal{N}_s$ are no longer directly incident to transformers as in the circuit model in Fig. 3.1(a).

3.2.3 Transformer Tap Ratio Optimization

Next, we formulate an OPF problem that will determine the tap settings of the TCUL transformer in the system. As mentioned earlier, the discrete tap positions lead to an MIP formulation, the complexity of which grows exponentially with the number of TCUL transformers [49]. To address this issue, we relax the values that the discrete transformer tap ratio $a_t \in \{\underline{a}, \dots \overline{a}\}$ can take, and allow a_t to take values on the continuous interval $[\underline{a}, \overline{a}]$. Once the optimal a_t is obtained, it will be rounded to the closest discrete value in $\{\underline{a}, \dots, \overline{a}\}$.

Given some operational objective function $f(V, q)$, which we describe in detail later in Section 3.3.3, that is defined over the system voltages, $V \in \mathbb{C}^{n+r+1}$, the available reactive power support, $q \in \mathbb{R}^n$, and the transformer tap ratios, $a \in \mathbb{R}^r$, the OPF problem of interest can be formulated as follows:

$$\min_{V,\, a,\, S_{ps'},\, q} \; f\left(V, q\right) \tag{3.7a}$$

such that

$$V_0 = V^s, \tag{3.7b}$$

$$\sum_{k \in \mathcal{H}_i} [Y^*]_{ik} V_i V_k^* - S_i - j q_i = 0, \qquad \forall i \in \mathcal{N} \backslash \mathcal{N}_p, \tag{3.7c}$$

$$\sum_{k \in \mathcal{H}_{p_t}} [Y^*]_{p_t k} V_{p_t} V_k^* - S_{p_t} + S_{p_t s'_t} - j q_{p_t} = 0, \qquad \forall t \in \mathcal{T}, \tag{3.7d}$$

$$\sum_{k \in \mathcal{H}_{s'_t}} [Y^*]_{s'_t k} V_{s'_t} V_k^* - S_{p_t s'_t} = 0, \qquad \forall t \in \mathcal{T}, \tag{3.7e}$$

$$V_{p_t} - a_t V_{s'_t} = 0, \qquad \forall t \in \mathcal{T}, \tag{3.7f}$$

and

$$\underline{V} \leq \left|V_i\right| \leq \overline{V}, \qquad \forall i \in \mathcal{N}, \tag{3.7g}$$

$$\underline{q}_i \leq \ q_i \ \leq \overline{q}_i, \qquad \forall i \in \mathcal{N}, \tag{3.7h}$$

$$\underline{a} \leq \ a_t \ \leq \overline{a}, \qquad \forall t \in \mathcal{T}, \tag{3.7i}$$

where the feeder's voltage is fixed, i.e., $V_0 = V^s = |V^s|\angle 0$ for some constant $|V^s|$. The high granularity of the available tap positions enables the continuous tap-ratio representation approach to yield acceptable results without incurring the added complexity of a MIP formulation [49–51]. However, the optimization problem in (3.7) is still challenging due to the nonlinearity in the power flow equations, as captured by constraints (3.7c)-(3.7e). Hence, the ensuing section will introduce additional relaxations to handle these nonlinearities in the power flow model.

Note that we include the reactive power support provided by the distributed energy resources (DERs) (fast time-scale devices) in the OPF for completeness; however, we do not consider the settings of these devices as optimization variables for the case studies in Section 3.5 since this is covered extensively in [29, 31, 52]. In Chapter 6, we will incorporate these device settings into our simulations as decision variables following the framework proposed in Chapter 2.

3.3 Convex Relaxation

In this section, we first reformulate the non-convex OPF problem in (3.7) into matrix form. Then, we review a modified transformer model that we proposed in [40]; this model will allow us to handle unbalanced three-phase OPF. Finally, we use the aforementioned modified transformer model to develop the convex relaxation of the matrix-based OPF formulation in (3.7).

3.3.1 Matrix-Based OPF Formulation

The complex power injection at bus $i \in \mathcal{N}$ is given by

$$S_i = V_i \sum_{k \in \mathcal{H}_i} [Y^*]_{ik} V_k^*, \tag{3.8}$$

where $S, V \in \mathbb{C}^{n+r+1}$. We define $W \in \mathbb{C}^{(n+r+1)\times(n+r+1)}$ as

$$W = VV^H = \begin{bmatrix} V_1^2 & \cdots & V_1 V_{n+r}^* \\ \vdots & \ddots & \vdots \\ V_1^* V_{n+r} & \cdots & V_{n+r}^2 \end{bmatrix}, \tag{3.9}$$

where W is a positive semidefinite (PSD) matrix ($W \succeq \mathbf{0}$) with rank 1. Let $E_i = e_i e_i^{\mathrm{T}}$, where e_i is a vector with all entries equal to zero except the i^{th} one, which is equal to one. Then, the complex power balance equation in (3.8) is linearly related to the entries of W as follows:

$$S_i = \mathrm{Tr}\left(H_i W\right), \tag{3.10}$$

where $H_i := Y^H E_i$. Furthermore, the complex power flowing from bus i to k over line $(i,k) \in \mathcal{E}_a$ is given by

$$S_{ik} = \mathrm{Tr}\left(A_{ik} W\right), \tag{3.11}$$

where $A_{ik} := -(e_k^{\mathrm{T}} Y^H e_i) E_{ik}$ and $E_{ik} := (e_i - e_k)\, e_i^{\mathrm{T}}$.

We remove the tap ratio from the voltage relationship in (3.7f) and (3.7i) by constraining the voltage on the secondary-side of the transformer relative to the primary side, i.e.,

$$\underline{a}^2 \, |V_{p_t}|^2 \leq \left|V_{s_t'}\right|^2 \leq \overline{a}^2 \, |V_{p_t}|^2 . \tag{3.12}$$

Therefore, the equivalent matrix formulation of the problem in (3.7) is as follows:

$$\min_{W \succeq \mathbf{0},\, S_{ps'},\, q} \; f\left(W, q\right) \tag{3.13a}$$

such that

$$[W]_{00} = \left(V^s\right)^2, \tag{3.13b}$$

$$\mathrm{Tr}\left(H_i W\right) - S_i - j q_i = 0, \qquad \forall i \in \mathcal{N} \backslash \mathcal{N}_p, \tag{3.13c}$$

$$\mathrm{Tr}\left(H_{p_t} W\right) - S_{p_t} + S_{p_t s'_t} - j q_{p_t} = 0, \qquad \forall t \in \mathcal{T}, \tag{3.13d}$$

$$\mathrm{Tr}\left(H_{s'_t} W\right) - S_{p_t s'_t} = 0, \qquad \forall t \in \mathcal{T}, \tag{3.13e}$$

and

$$\underline{V}^2 \leq \; [W]_{ii} \; \leq \overline{V}^2, \qquad \forall i \in \mathcal{N}, \tag{3.13f}$$

$$\underline{q}_i \leq \; q_i \; \leq \overline{q}_i, \qquad \forall i \in \mathcal{N}, \tag{3.13g}$$

$$\underline{a}^2 \left[W\right]_{p_t p_t} \leq \; [W]_{s'_t s'_t} \; \leq \overline{a}^2 \left[W\right]_{p_t p_t}, \qquad \forall t \in \mathcal{T}, \tag{3.13h}$$

and

$$[W]_{p_t s'_t} = [W]_{s'_t p_t} \geq 0, \qquad \forall t \in \mathcal{T}, \tag{3.13i}$$

$$\mathrm{rank}(W) = 1. \tag{3.13j}$$

The constraint (3.13i) ensures that V_{p_t} and $V_{s'_t}$ have the same phase angle. Once the solution to (3.13) is obtained, the tap ratio a_t of transformer t can be determined using the bus voltage ratio as follows:

$$a_t = \sqrt{\left|V_{p_t}\right|^2 / \left|V_{s'_t}\right|^2} = \sqrt{[W]_{p_t p_t} / [W]_{s'_t s'_t}}\,. \tag{3.14}$$

3.3.2 Non-ideal Transformer Model

As will be discussed in detail in Section 3.3.3, the optimization problem in (3.13) can be relaxed to a convex one by dropping the rank-1 constraint [29, 31, 52]. For distribution networks, it has been shown that this relaxation approach would yield a rank-1 solution [29], thereby achieving the global optimum of the original problem. As pointed out in [40], the transformer model in Fig. 3.1(b) results in two electrically disconnected networks. Accordingly, it has been shown that the solution to the relaxed problem could be of higher rank, albeit with no loss of optimality as compared to the original problem. However, the higher-rank solution leads to an arbitrary phase angle differ-

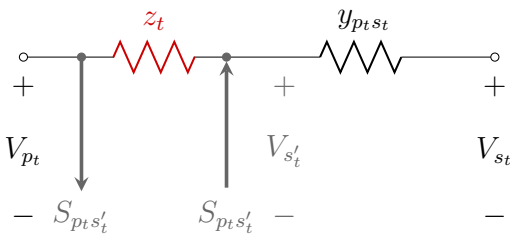

Figure 3.2: Non-ideal transformer model.

ence between the primary-side bus and downstream buses. Such phase angle ambiguity would significantly complicate the analysis of the three-phase system, since the angle separation among the three phases can no longer be enforced at the virtual secondary bus. We refer the reader to Appendix A.2 to further motivate the non-ideal transformer model.

The issue discussed here can be resolved by introducing the modified transformer model shown in Fig. 3.2, where we place an impedance z_t between p_t and s'_t of the ideal transformer introduced earlier to 'reconnect' the network. Choosing an appropriate value of z_t will ensure that the power flow in the modified model almost mimics that of an electrically disconnected network. As detailed later, this modification would help maintain the phase angle consistency on both sides of the transformer; i.e., $\theta_{p_t} \approx \theta_{s'_t}$. This is highly attractive since it allows one to solve an equivalent convex formulation of the original OPF problem in (3.7), while enforcing the correct phase shift for the transformers. This is especially important to extend the OPF framework to three-phase systems where the phase separation is lost with the disconnected network.

As discussed in detail in Section 3.5.3, we found via numerical simulations that there can be a large range of values for z_t that yield solutions that are sufficiently accurate. However, if $|z_t|$ is too small, the augmented network admittance matrix Y could be problematic as the entries corresponding to (p_t, s'_t) would become much larger than the rest of Y. Although a small $|z_t|$ maintains $\theta_{p_t} \approx \theta_{s'_t}$, the power flow through z_t will become comparable to $S_{p_t s'_t}$, and thus the system power flow would be different from the original ideal transformer model. On the other hand, if $|z_t|$ becomes too large, then the system behavior begins to mirror the original disconnected case with ideal transformers. The latter scenario will result in a solution W that has a rank greater than one. The value of $|z_t|$ needs to be chosen within a specific

range, which can vary based on the system and the gains in the cost function. Interestingly, all of our numerical simulations corroborated that a z_t with a resistance value of several orders of magnitude larger than the neighboring distribution line segments (around 2-4 orders for our test systems) yielded the best results.

Example 1 (Two-Bus Example) *Consider a simple 2-bus system with* $|V_{p_t}|\angle\theta_{p_t}$, $\left|V_{s'_t}\right|\angle\theta_{s'_t}$, *and* $z_t = r_t + jx_t$, *where bus* p_t *is the primary side of the transformer. The power loss on the line is given by*

$$\begin{aligned} S_t^l &= \frac{1}{z_t^*}\left(V_{p_t} - V_{s'_t}\right)^2 \\ &= \frac{r_t + jx_t}{r_t^2 + x_t^2}\left(|V_{p_t}|^2 + \left|V_{s'_t}\right|^2 - 2\,|V_{p_t}|\left|V_{s'_t}\right|\cos\left(\theta_{p_t} - \theta_{s'_t}\right)\right). \end{aligned} \tag{3.15}$$

Since we are not working with a phase-shifting transformer, we can simplify the expression above by assuming that $\theta_{p_t} \approx \theta_{s'_t}$. *Then, by defining the turns ratio as* $a_t = N_{p_t}/N_{s'_t}$, *we obtain that*

$$P_t^l = \frac{r_t}{r_t^2 + x_t^2}\left|V_{s'_t}\right|^2\left(a_t^2 - 2a_t + 1\right), \tag{3.16}$$

$$Q_t^l = \frac{x_t}{r_t^2 + x_t^2}\left|V_{s'_t}\right|^2\left(a_t^2 - 2a_t + 1\right), \tag{3.17}$$

where $a_t \in [0.9, 1.1]$ *for the per unit voltages. In the case studies in Section 3.5, we minimize generation of active power losses and choose* $r_t \gg 0$ *and* $x_t = 0$ *so that* Q_t^l *can be neglected.*

■

3.3.3 Rank-Relaxed Convex OPF

We apply the modifications to the transformer model as described in Section III.B and relax the rank-1 constraint in (3.13) to get a rank-relaxed convex OPF of the form:

$$\min_{W \succeq \mathbf{0},\, S_{ps'},\, q} \; f\left(W, q\right) \tag{3.18a}$$

such that

$$[W]_{00} = (V^s)^2, \tag{3.18b}$$

$$\mathrm{Tr}\left(\tilde{H}_i W\right) - S_i - jq_i = 0, \qquad \forall i \in \mathcal{N}\backslash\mathcal{N}_p, \tag{3.18c}$$

$$\mathrm{Tr}\left(\tilde{H}_{p_t} W\right) - S_{p_t} + S_{p_t s'_t} - jq_{p_t} = 0, \qquad \forall t \in \mathcal{T}, \tag{3.18d}$$

$$\mathrm{Tr}\left(\tilde{H}_{s'_t} W\right) - S_{p_t s'_t} = 0, \qquad \forall t \in \mathcal{T}, \tag{3.18e}$$

and

$$\underline{V}^2 \leq [W]_{ii} \leq \overline{V}^2, \qquad \forall i \in \mathcal{N}, \tag{3.18f}$$

$$\underline{q}_i \leq q_i \leq \overline{q}_i, \qquad \forall i \in \mathcal{N}, \tag{3.18g}$$

$$\underline{a}^2 [W]_{p_t p_t} \leq [W]_{s'_t s'_t} \leq \overline{a}^2 [W]_{p_t p_t}, \qquad \forall t \in \mathcal{T}, \tag{3.18h}$$

where $\tilde{H}$ incorporates the non-ideal transformer model and (3.13i) is dropped since the network is connected. As detailed in Appendix A.1, the rank-relaxed SDP formulation in (3.18) is guaranteed to achieve the global optimality of the non-convex tap setting problem with the rank constraint.

Next, we provide a qualitative explanation of the convex relaxation. Figure 3.3(a) shows the ellipse that results when the distribution line segment power P_{ik} from bus i to bus k is plotted against the distribution line segment power P_{ki} for fixed bus voltages and the powers parameterized relative to the phase difference across the line. The blue line along the boundary represents the

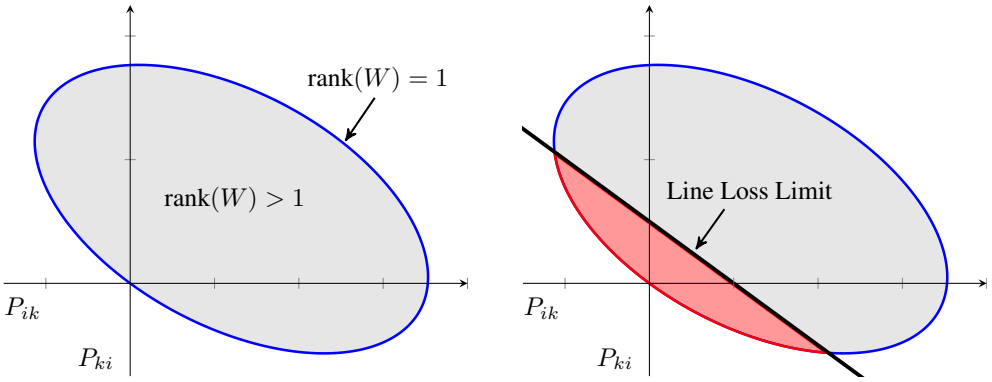

(a) Unconstrained line losses. (b) Constrained line losses.

Figure 3.3: Distribution line segment power transfers.

rank-1 constraint. The rank-relaxation allows solutions within the ellipse. We will minimize for distribution line segment losses so that the solutions to both the rank-1 and relaxed problem lie along the boundary in the second and fourth quadrants. Note that the origin represents a lossless line. Figure 3.3(b) shows how thermal limits, e.g., maximum power loss, change the solution set to the red shaded area.

The objective function $f(W, q)$ includes a term that captures system losses, which is necessary to ensure that a rank-1 solution can be obtained from the relaxed problem [29, 31, 52, 54]. It may also include additional terms to capture voltage tracking objectives and power factor targets. The discussion above can be formalized by considering an objective function of the form

$$f(W, q) = f_0(W) + \sum_i f_i(W, q), \tag{3.19}$$

where

$$f_0(W) = \sum_{i \in \mathcal{N}_a} \sum_{k \in \mathcal{H}_i} \mathrm{Re}\left\{ \mathrm{Tr}\left(\tilde{A}_{ik} W \right) \right\}, \tag{3.20}$$

which captures the total losses of all distribution line segments. The additional penalty terms in (3.19), $\sum_i f_i(W, q)$, could be chosen so as to achieve other objectives of interest; next, we discuss a few possible choices.

If a given network has considerable distributed generation, minimizing line losses may not reduce the total demand at the (sub)transmission substation. This can be easily addressed by including a penalty term in (3.19) of the form

$$f_1(W, q) = \nu \, \mathrm{Re}\left\{ \mathrm{Tr}\left(\tilde{H}_0 W \right) \right\}, \tag{3.21}$$

where ν is a positive weighting factor.

Additionally, to minimize voltage magnitude deviations from a specified nominal voltage, V_i^n, e.g., $V_i^n = 1$ p.u. for all i, we can include a penalty term in (3.19) of the form

$$f_2(W, q) = \sum_{i \in \mathcal{N}} w_i \left((V_i^n)^2 - [W]_{ii} \right)^2, \tag{3.22}$$

where $\{w_i\}$ are the positive weighting factors per bus i [30]. The weights themselves should be chosen based on: (i) the distance between the bus and the feeder, and (ii) buses that are prone to voltage violations. Intuitively,

buses near the end of the (sub)laterals should be weighted more than those near the feeder in traditional radial distribution networks with unidirectional power flow.

Next, utilities aim at operating distribution systems with a unity power factor at the feeder head. Motivated by this, the reactive power injection to the feeder head bus can be penalized by

$$f_3(W,q) = \gamma \left\| \mathrm{Im} \left\{ \mathrm{Tr} \left(\tilde{H}_0 W \right) \right\} \right\|_2^2, \tag{3.23}$$

where γ is a positive weighting factor.

Finally, we consider the costs of including reactive power support, which can be either policy driven or economic-based. In the slow time-scale control, we can penalize the reactive power contributions of the DERs to bias the optimization towards using the transformer tap positions rather than reactive power to minimize costs. The penalty will have the form

$$f_4(W,q) = \sum_{i \in \mathcal{N}} \alpha_i \left(q_i - \beta_i \right)^2, \tag{3.24}$$

where α_i is a positive weighting factor and β_i is the reactive power bias, e.g., the current settings of the switched capacitors attached to bus i can be represented with β_i.

Note that the candidate cost functions introduced are separable among all the buses; this will facilitate the development of the distributed solver as detailed soon in Section 3.4.

3.3.4 Extension to Unbalanced Three-Phase Systems

So far, we have assumed balanced operation, which reduced the system model to a per-phase equivalent; however, distribution systems are inherently unbalanced with untransposed distribution lines and have single-, two-, and three-phase radial feeds; therefore, a three-phase system extension of the ideas discussed so far is well motivated. The authors in [52] discuss extending the SDP relaxation OPF approach to unbalanced three-phase systems; our work focuses on incorporating three-phase TCUL transformers into such formulation.

For a balanced system, a rank-1 exact solution can be recovered even

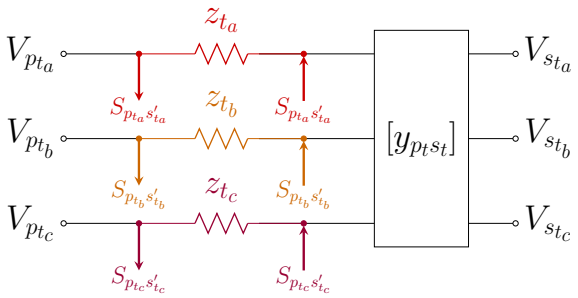

Figure 3.4: Equivalent three-phase transformer model.

though the relaxed OPF in (3.13), the formulation of which is based on the ideal transformer model in Fig. 3.1(b), has higher-rank solutions. The additional constraints on the transformer (3.13i) will ensure a zero phase angle difference between the primary- and secondary-side bus voltages of that particular phase; however, the phase angles of buses downstream of the secondary-side bus are not dependent on the primary side of the transformer. In a multi-phase network, this implies that there is no constraint that enforces the angle difference between phases, i.e., $\theta_a - \theta_b \approx 120°$. We can maintain this phase separation by:

(i) reconnecting the network by using the non-ideal transformer model that we proposed in Section 3.3.2, or

(ii) constraining the off-diagonal entries of the submatrices $\boldsymbol{W}_{p_t p_t}$ and $\boldsymbol{W}_{s'_t s'_t}$ associated with the primary and secondary sides of the transformer.

The issue with (ii) is that the constraints turn out to be highly nonlinear in $\boldsymbol{W}$, which impedes us from incorporating them into the SDP OPF formulation in (3.18); for this reason, we choose solution (i).

Consider the three-phase TCUL model in Fig. 3.4; we will follow a configuration similar to the one used for the non-ideal transformer model in Section 3.3.2. The core losses of the transformer will be neglected [47], and we will assume that each phase can independently regulate its secondary-side virtual bus voltage. This will be equivalent to a collection of three single-phase transformers (see Fig. 3.2), which are coupled by the secondary-side distribution line admittance $\boldsymbol{y}_{p_t s_t} \in \mathbb{C}^{3\times 3}$. Note that there is no mutual impedance between the primary-side bus and the virtual secondary-side virtual bus. Thus, we can optimize every tap individually and maintain the proper phase separation. We will use V_{i_a}, V_{i_b}, V_{i_c} to distinguish the voltages

phasors for each phase at bus i. We also define a vector $V_{3\phi}$ that will include the voltage phasors for all the buses in the network that has at most $3\times(n+r+1)$ elements if every bus has three-phase circuits. The bus voltage subindex allows one to maintain the notational consistency with the earlier balanced case. The only difference lies in the dimension of the counterpart vectors to accommodate the three phases. For example, the three-phase line admittance is a block $\boldsymbol{y}_{ik} \in \mathbb{C}^{3\times 3}$, as compared to $y_{ik} \in \mathbb{C}$ for the balanced cases. This way, all the analysis and problem formulation so far carries over by defining $\boldsymbol{W}_{3\phi} = \boldsymbol{V}_{3\phi}\boldsymbol{V}_{3\phi}^H$. The power flow equations will remain unchanged where we have an (in)equality constraint per phase; however, the mutual impedances of the untransposed lines makes it more complicated to compute the line losses as compared to (3.20).

Let $\tilde{\boldsymbol{e}}_i \in \mathbb{N}^{|\boldsymbol{V}_{3\phi}|}$ be the vector with all entries equal to zero except the entries corresponding to each phase present at bus i, which are set to one. Define the matrices $\boldsymbol{G}$ and $\boldsymbol{K}$ as

$$\boldsymbol{G} = \text{diag}(\tilde{\boldsymbol{e}}_1)\boldsymbol{Y}^H\text{diag}(\tilde{\boldsymbol{e}}_2) + \text{diag}(\tilde{\boldsymbol{e}}_2)\boldsymbol{Y}^H\text{diag}(\tilde{\boldsymbol{e}}_1) \tag{3.25}$$

and

$$[\boldsymbol{K}]_{ij} = \begin{cases} -1, & [\tilde{\boldsymbol{e}}_{1_p}]_i = [\tilde{\boldsymbol{e}}_{2_p}]_j = 1,\ p = \{a,b,c\} \\ 1, & i = j, \\ 0, & \text{otherwise}, \end{cases} \tag{3.26}$$

where $\tilde{\boldsymbol{e}}_{i_p}$ is the vector $\tilde{\boldsymbol{e}}_i$ conditioned on phase p, i.e., the vector contains a single nonzero entry corresponding to the entry for phase p of bus i. Thus, we update the line loss coefficient matrix $\boldsymbol{A}_{ik}$ with

$$\boldsymbol{A}_{ik} = \boldsymbol{G}\boldsymbol{K} \tag{3.27}$$

to capture the total losses across each distribution line segment.

3.4 Distributed Solver

It is well known that centralized algorithms for solving the SDP problem in (3.13) are not suitable for large systems (see, e.g., [20]). To address this issue, we propose the use of the Alternating Direction Method-of-Multipliers

(ADMM), which allows for an efficient distributed solution to the convex SDP problem in (3.18). The ADMM is proven to be a powerful distributed optimization method and offers many benefits [20]. In particular, with ADMM, the complexity of the SDP problem scales with the sub-area size rather than with the full network size, and the communication architecture is simpler than that of a centralized scheme. Suppose we partition the system into two areas; Fig. 3.5 shows a topographical view of the corresponding submatrices $W^{(1)}$, $W^{(2)}$ and the boundary conditions $W^{(1,2)} = W^{(2,1)}$ that result from these partitions. The computational complexity per iteration using the popular interior point method for our SDP problem (3.18) scales with the fourth-order in the size of matrix W, or equivalently the number of system buses (see, e.g., [59]). For large systems, small partitions will provide significant savings in the number of optimization variables as depicted by the empty off-diagonal blocks in Fig. 3.5; however, the increased number of boundary conditions will require more super-iterations for convergence to a solution.

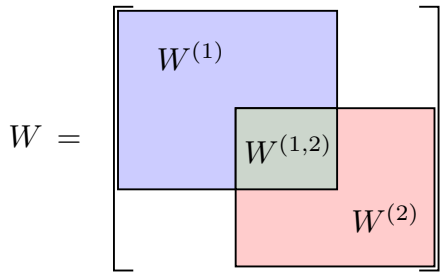

Figure 3.5: Partitioned system variables.

ADMM iteratively minimizes the augmented Lagrangian over three types of variables: (i) the *primary* variables, i.e., the bus voltages and transformer power transfers; (ii) the *auxiliary* variables that are used to enforce boundary conditions among neighboring areas; and (iii) the *multipliers* for dualizing the relaxed problem. The Lagrangian is designed to be separable relative to each type of variable so that we can cyclically minimize with respect to one variable type while fixing the others. This allows us to solve the problem distributedly and achieve convergence to the same solution obtained with a centralized solver [20].

We begin by partitioning the system into $\mathcal{P} := \{1, 2 \ldots, L\}$ areas such that $\cup_{i=1}^{L} \mathcal{A}^{(i)} = \mathcal{N}_a$, $\cap_{i=1}^{L} \mathcal{A}^{(i)} = \emptyset$, and $|\mathcal{A}^{(i)}| \geq 1$ for all i. To include the coupled buses, each area $\mathcal{A}^{(i)}$ needs to be augmented, and the extended

area is $\bar{\mathcal{A}}^{(i)} := \mathcal{A}^{(i)} \cup \{y \,|\, (x,y) \in \mathcal{E}_a, x \in \mathcal{A}^{(i)}, y \in \mathcal{A}^{(j)}, i \neq j\}$. Then, the neighbors of area $\bar{\mathcal{A}}^{(i)}$ are defined as $\mathcal{M}^{(i)} := \{j \,|\, \bar{\mathcal{A}}^{(i)} \cap \bar{\mathcal{A}}^{(j)} \neq \emptyset\}$. For area $\bar{\mathcal{A}}^{(i)}$, let $W^{(i)} \in \mathbb{C}^{|\bar{\mathcal{A}}^{(i)}| \times |\bar{\mathcal{A}}^{(i)}|}$ denote the corresponding local matrix for the outer product of the bus voltages, e.g., the $|\bar{\mathcal{A}}^{(i)}| \times |\bar{\mathcal{A}}^{(i)}|$ submatrix of W corresponding to area i.

To enforce consistency between partitions, boundary conditions are required to constrain the submatrices $W^{(i,j)} = W^{(j,i)} \in \mathbb{C}^{2\times 2}$ for single phase ($\mathbb{C}^{6\times 6}$ for three phase) associated with the overlap between neighboring areas. We define the auxiliary variables for the boundary conditions of the local optimization as $E^{(i,j)}, F^{(i,j)} \in \mathbb{R}^{2\times 2}$ (similarly $\mathbb{R}^{6\times 6}$ for the three-phase case). These variables $E^{(i,j)}$ ($F^{(i,j)}$) are used to enforce the real (imaginary) part of the submatrix equality boundary condition on bus voltages. Note that without the auxiliary variables, our problem would not be separable with respect to each $W^{(i)}$.

Example 2 (Two Area Example) *Consider the four bus, two area, single-phase example shown in Fig. 3.6. Area 1 will have* $\mathcal{A}^{(1)} = \{1,2\}$ *and* $\bar{\mathcal{A}}^{(1)} = \{1,2,3\}$ *so that* $W^{(1)} \in \mathbb{C}^{3\times 3}$. *Similarly, area 2 will have* $\mathcal{A}^{(2)} = \{3,4\}$ *and* $\bar{\mathcal{A}}^{(2)} = \{2,3,4\}$ *so that* $W^{(2)} \in \mathbb{C}^{3\times 3}$. *The overlap between areas is* $\bar{\mathcal{A}}^{(1)} \cap \bar{\mathcal{A}}^{(2)} = \{2,3\}$ *and* $W^{(1,2)} = W^{(2,1)} \in \mathbb{C}^{2\times 2}$.

■

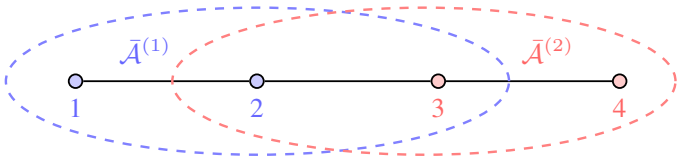

Figure 3.6: Two area partition example.

For each area we also define $\mathcal{B}^{(i)}$, which captures the set of sub-matrices that satisfy the local power flow and voltage constraints described in (3.18c)-(3.18h) for area $\bar{\mathcal{A}}^{(i)}$. Given that all of the cost functions in Section 3.3.3 are separable per area, we can rewrite the global minimization problem in (3.18) as

$$\min_{W^{(i)} \succeq \mathbf{0}, q^{(i)}} \quad \sum_{i \in \mathcal{P}} f^{(i)}\left(W^{(i)}, q^{(i)}\right) \tag{3.24a}$$

such that

$$W^{(i)} \in \mathcal{B}^{(i)}, \ \forall i \in \mathcal{P}, \tag{3.24b}$$

and

$$\mathrm{Re}\left\{W^{(i,j)}\right\} - E^{(i,j)} = 0, \qquad \forall j \in \mathcal{M}^{(i)}, \tag{3.24c}$$

$$\mathrm{Im}\left\{W^{(i,j)}\right\} - F^{(i,j)} = 0, \qquad \forall j \in \mathcal{M}^{(i)}, \tag{3.24d}$$

where

$$E^{(i,j)} - E^{(j,i)} = 0, \qquad \forall j \in \mathcal{M}^{(i)}, \tag{3.24e}$$

$$F^{(i,j)} - F^{(j,i)} = 0, \qquad \forall j \in \mathcal{M}^{(i)}. \tag{3.24f}$$

We leverage the relations in (3.24e) and (3.24f) when formulating the update rules of the distributed algorithm, but they are not enforced directly in the optimization problem. Note that the primary- and virtual secondary-side buses of a transformer cannot reside in two different areas. In our system model, we assume that the transformer t is attached at p_t, and that $\{p_t, s'_t\}$ are effectively the same physical bus; thus, its behavior is completely captured by $\mathcal{B}^{(i)}$ where $p_t \in \mathcal{A}^{(i)}$, and the boundary conditions will be enforced between buses s'_t and s_t.

3.4.1 Augmented Lagrangian

Let $\Gamma^{(i,j)}, \Lambda^{(i,j)} \in \mathbb{R}^{2\times 2}$ denote the Lagrange multipliers associated with the equality constraints in (3.24c) and (3.24d), respectively, where $c > 0$ is the penalty coefficient. The augmented Lagrangian function for (3.24) is as follows:

$$\begin{aligned}
\mathcal{L}_c(W, q, E, F, \Gamma, \Lambda) = \\
&\sum_{i\in\mathcal{P}}\Bigg\{ f^{(i)}\big(W^{(i)}, q^{(i)}\big) + \sum_{k\in\mathcal{M}^{(i)}} \Bigg[\mathrm{Tr}\Big(\Gamma^{(i,j)^{\mathrm{T}}} \Big(\mathrm{Re}\Big\{W^{(i,j)}\Big\} - E^{(i,j)} \Big) \Big) \\
&+ \frac{c}{2} \left\| \mathrm{Re}\Big\{W^{(i,j)}\Big\} - E^{(i,j)} \right\|_F^2 + \mathrm{Tr}\Big({\Lambda^{(i,j)}}^{\mathrm{T}} \Big(\mathrm{Im}\Big\{W^{(i,j)}\Big\} - F^{(i,j)} \Big) \Big) \\
&+ \frac{c}{2} \left\| \mathrm{Re}\Big\{W^{(i,j)}\Big\} - F^{(i,j)} \right\|_F^2 \Bigg] \Bigg\},
\end{aligned} \tag{3.25}$$

which is clearly separable amongst the three groups of variables such that

$$\mathcal{L}_c(\cdot) = \sum_{i \in \mathcal{P}} \mathcal{L}_c^{(i)}(\cdot). \tag{3.26}$$

Then, we can cyclically optimize the augmented Lagrangian $\mathcal{L}_c(\cdot)$ with respect to one of the groups of variables while holding the others constant with the following three-step update rule for the k^{th} iteration:

[S1.] *Primal Variables Update:* We take the infimum of $\mathcal{L}_c(\cdot)$ with respect to the primal variables, and update them as

$$W^{(i)}[k] = \underset{W^{(i)} \in \mathcal{B}^{(i)},\, W^{(i)} \succeq \mathbf{0},\, q^{(i)}}{\arg\min} \mathcal{L}_c^{(i)} \left(W^{(i)}, q^{(i)} \right), \tag{3.27}$$

which is dependent of the dual variables $\Gamma^{(i,j)}[k-1]$ and $\Lambda^{(i,j)}[k-1]$, and the boundary conditions $E^{(i,j)}[k-1]$ and $F^{(i,j)}[k-1]$.

[S2.] *Auxiliary Variables Update:* Recall that $E^{(i,j)} = E^{(j,i)}$ and $F^{(i,j)} = F^{(j,i)}$, also note that $\Lambda^{(i,j)} = -\Lambda^{(j,i)}$; then

$$\nabla_{E^{(i,j)}} \mathcal{L}_c \left(W^{(i,j)}, E^{(i,j)} \right) = \mathrm{Re} \left\{ W^{(i,j)} + W^{(j,i)} \right\} - 2E^{(i,j)} = 0, \tag{3.28}$$
$$\nabla_{F^{(i,j)}} \mathcal{L}_c \left(W^{(i,j)}, F^{(i,j)} \right) = \mathrm{Im} \left\{ W^{(i,j)} + W^{(j,i)} \right\} - 2F^{(i,j)} = 0. \tag{3.29}$$

We update the auxiliary variables with

$$E^{(i,j)}[k] = \frac{1}{2} \mathrm{Re} \left\{ W^{(i,j)}[k] + W^{(j,i)}[k] \right\}, \tag{3.30}$$
$$F^{(i,j)}[k] = \frac{1}{2} \mathrm{Im} \left\{ W^{(i,j)}[k] + W^{(j,i)}[k] \right\}, \tag{3.31}$$

for $j \in \mathcal{M}^{(i)}$.

[S3.] *Multipliers Update:* The gradient for the $\mathcal{L}(\cdot)$ with respect to the dual variables is

$$\nabla_{\Gamma^{(i,j)}} \mathcal{L}_c^{(i)} \left(W^{(i,j)}, E^{(i,j)} \right) = \mathrm{Re} \left\{ W^{(i,j)} \right\} - E^{(i,j)}, \tag{3.32}$$
$$\nabla_{\Lambda^{(i,j)}} \mathcal{L}_c^{(i)} \left(W^{(i,j)}, F^{(i,j)} \right) = \mathrm{Im} \left\{ W^{(i,j)} \right\} - F^{(i,j)}. \tag{3.33}$$

We initialize all the multipliers to zero; then, we solve the dual variables using an ascent method and apply (3.30)–(3.31). Thus, for $j \in \mathcal{M}^{(i)}$,

the update rules for the dual variables are

$$\Gamma^{(i,j)}[k]=\Gamma^{(i,j)}[k-1]+\frac{c}{2}\mathrm{Re}\left\{W^{(i,j)}[k]-W^{(j,i)}[k]\right\}, \tag{3.34}$$

$$\Lambda^{(i,j)}[k]=\Lambda^{(i,j)}[k-1]+\frac{c}{2}\mathrm{Im}\left\{W^{(i,j)}[k]-W^{(j,i)}[k]\right\}. \tag{3.35}$$

Note that it follows naturally that $\Gamma^{(i,j)} = -\Gamma^{(j,i)}$ and $\Lambda^{(i,j)} = -\Lambda^{(j,i)}$.

Although Steps S1-S3 are formulated for the per-phase equivalent of a balanced network, they can easily be extended to solve unbalanced three-phase systems as well by accounting for all phase voltages per bus.

3.5 Case Studies

In this section, we illustrate the ability of the distributed, ADMM-based algorithm proposed in Section 3.4 to optimally set TCUL tap positions for both single- and three-phase cases of a 15-bus network. We also demonstrate the effectiveness of the algorithm on the IEEE 123-bus test system [58]. In all our studies, the voltage magnitude inequality constraints for all cases are limited to 1 p.u. $\pm$ 4.8%, rather than the common $\pm$ 5% to account for discrepancies associated with rounding to nearest discrete tap position.

We performed the simulations in MATLAB using the CVX package [60] with the symmetric cone solver SeDuMi [61]. This software package was used to solve the centralized problem and to update the primal variables $W^{(1)}, \ldots, W^{(L)}$ in Step S1 of the distributed algorithm.

While in Section 3.3.3 we provided several penalty terms for different performance objectives, the cost function used in the case studies in Sections 3.5.1 and 3.5.2 only considers the distribution line losses as defined in (3.20), i.e., $f(W) = f_0(W)$.

3.5.1 15-Bus Distribution System

We begin with the 15-bus network shown in Fig. 3.7, which we derived from the IEEE 13-bus—a three-phase, unbalanced distribution system, (see, e.g., [47, 58]). The system has a three-phase voltage regulation transformer between buses 650 and 632. The rest of the system contains single-, two-, and

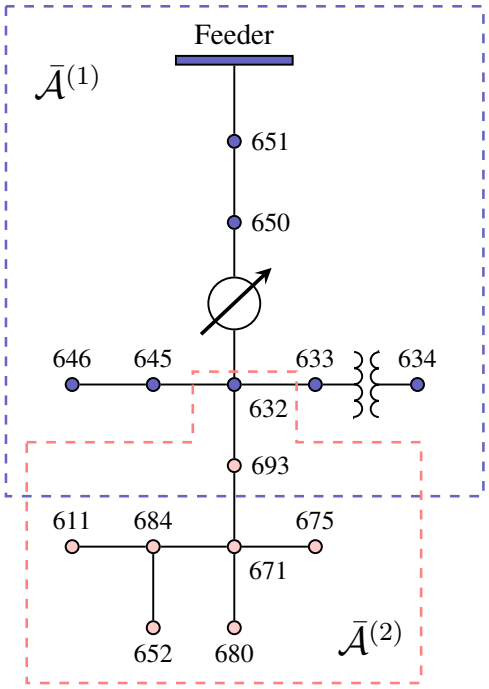

Figure 3.7: 15-bus unbalanced distribution system.

three-phase sublaterals. Buses 650 and 651 were added between the feeder and the transformer so that the transformer was not directly connected to the slack bus. Bus 693 was added to account for the distributed load along line (632, 671), and bus 692 was removed since it corresponds to a closed switch connected between buses 671 and 675.

In Fig. 3.7, busses are color coded for areas $\mathcal{A}^{(1)}$ and $\mathcal{A}^{(2)}$; the extended areas $\bar{\mathcal{A}}^{(1)}$ and $\bar{\mathcal{A}}^{(2)}$ are distinguished by the dashed lines circling the areas. The overlap occurs at buses 632 and 693 where $W^{(1,2)} \in \mathbb{C}^{2\times 2}$ for the 14-bus balanced case and $\boldsymbol{W}^{(1,2)} \in \mathbb{C}^{6\times 6}$ for the following three-phase case.

Per-Phase Equivalent Results

For the balanced system, we isolate phase C from Fig. 3.7 since it is the dominant phase of the 15-bus network, and create a 14-bus balanced case that excludes bus 652 from the network topology since phase C is not present on that bus. The results obtained using: (i) a centralized algorithm, (ii) our distributed algorithm, and (iii) an exhaustive search, where we enumerate all of the possible tap ratio combinations are shown in Table 3.1. All three methods return the same optimal tap position. The exhaustive search uses

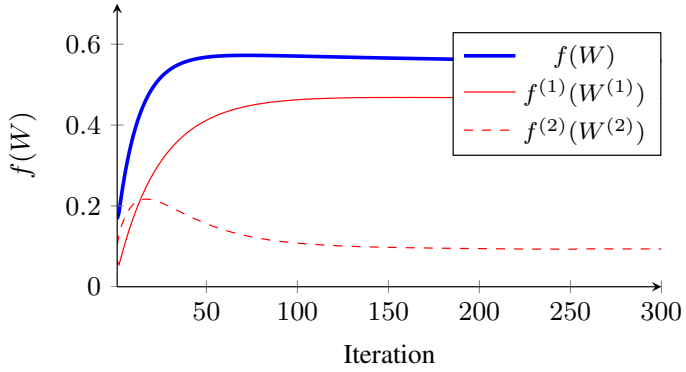

(a) Local cost functions.

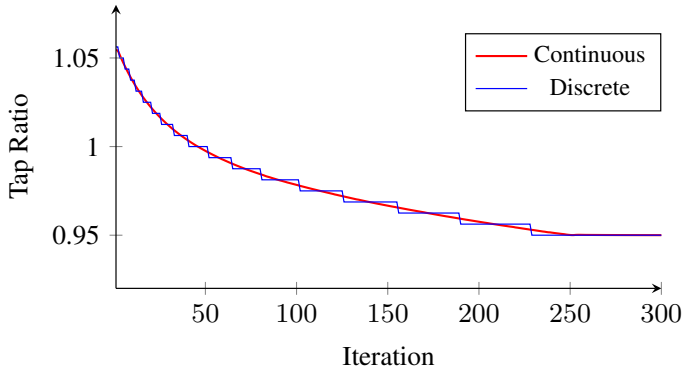

(b) TCUL transformer tap position.

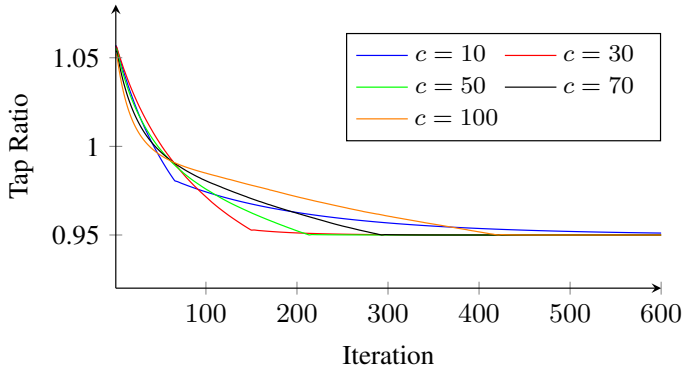

(c) Convergence for various penalty parameters.

Figure 3.8: 14-bus, per-phase equivalent distributed optimization results.

Table 3.1: 14-Bus Balanced Network Results

	Centralized OPF	Distributed OPF	Exhaustive Search
$f(W)$	0.559	0.466, 0.094	0.554
$\lvert V_{p_t}\rvert$	1.007	1.007	1.007
$\lvert V_{s'_t}\rvert$	1.060	1.060	–
$\lvert V_{s_t}\rvert$	1.048	1.048	1.048
$S_{p_t s'_t}$	$11.05 + j4.01$	$11.04 + j4.01$	–
S_t	0.005	0.005	–
Tap	-8	-8	-8
CPU Time	0.8 s	–	0.1 s

an ideal transformer model, and the difference in the cost function $f(W)$ compared to the other two methods is due to the loss S_t through the non-ideal transformer model. Figures 3.8(a) and 3.8(b) show the evolution of the area cost functions and the corresponding tap ratio for $c = 60$. Notice that the optimal position occurs near iteration 250 where the global $f(W)$ remains relatively unchanged after iteration 125, so there are several tap ratios that will result in acceptable solutions. Figure 3.8(c) shows the effect of changing the penalty parameter c. For the 14-bus network, the fastest convergence occurs when $c \approx 30$.

Unbalanced Three-Phase System Results

In the centralized case, the 15-bus, unbalanced three-phase system problem will have 1763 optimization variables since $\boldsymbol{W} \in \mathbb{C}^{41\times 41}$. In contrast, the distributed case has a 21.8% reduction for a combined total of 1379 variables (910 for area 1 and 469 for area 2). The results for the unbalanced three-phase case are listed in Table 3.2 with the progress of the distributed algorithm displayed in Fig. 3.9. The solutions to the relaxed problem (incorporating the non-ideal transformer model) obtained with the centralized and distributed solvers yielded the same tap positions of $\{-7, -8, -6\}$. The exhaustive search solution yielded a different result for phase A, with the final

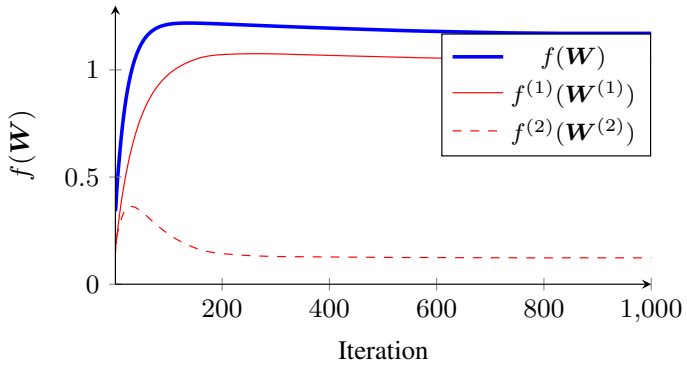

(a) Local cost functions.

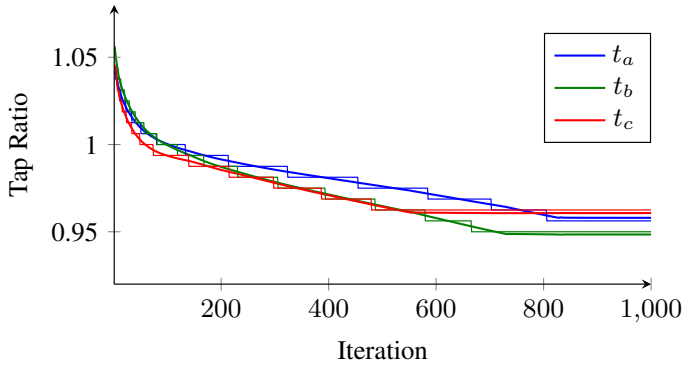

(b) TCUL transformer tap positions.

Figure 3.9: 15-bus, three-phase distribution optimization results.

tap positions being $\{-6, -8, -6\}$. However, if we check the centralized and distributed result by solving the power flow equations, we find the solution to be acceptable. Similar to the balanced case, there are several solutions around the selected tap positions with nearly the same costs for the objective function.

From the results in Table 3.1, we can see that the exhaustive search method for a single tap resulted in a faster computation than the relaxed centralized problem, with CPU times of 0.1 s versus 0.8 s, respectively. In the three-phase case, the added computational complexity introduced by the dimensional increase associated with the additional phases resulted in an increase of the CPU time for the exhaustive search solution to 107.2 s, while the relaxed centralized case increased slightly to 2.0 s. The ADMM-based solution that we proposed was tested using a serial implementation on a single-core; thus, we intentionally did not include the CPU time for this case. We refer the reader to [20, 52, 56] for computational benefits of ADMM.

Table 3.2: Unbalanced Three-Phase 15-Bus Network Results

	Centralized OPF	Distributed OPF	Exhaustive Search	Power Flow
$f(\boldsymbol{W})$	1.170	1.047, 0.123	1.170	1.167
$\lvert\boldsymbol{V}_{p_t}\rvert$	1.028 1.017 1.023	1.028 1.017 1.023	1.028 1.017 1.023	1.028 1.017 1.023
$\lvert\boldsymbol{V}_{s'_t}\rvert$	1.073 1.073 1.064	1.073 1.073 1.064	– – –	– – –
$\lvert\boldsymbol{V}_{s_t}\rvert$	1.048 1.044 1.043	1.048 1.044 1.043	1.043 1.042 1.041	1.050 1.042 1.041
$\boldsymbol{S}_{p_t s'_t}$	$8.5 + j4.1$ $9.6 + j4.7$ $9.8 + j3.3$	$8.5 + j4.1$ $9.6 + j4.7$ $9.8 + j3.3$	– – –	– – –
$\boldsymbol{S}_t$	0.004	0.004	–	–
Tap	-7, -8, -6	-7, -8, -6	-6, -8 , -6	-7, -8, -6
CPU Time	2.0 s	–	107.2 s	–

3.5.2 Unbalanced Three-Phase 123-Bus Distribution System

Figure 3.10 shows the one-line diagram for the IEEE 123-bus, three-phase distribution system, which includes four three-phase voltage regulation transformers [58]; we also divide the system into six areas. This is a comprehensive system that is mostly unbalanced and contains overhead/underground distribution line segments with single-, two-, and three-phase branches. We set the voltage at the feeder to 1.01 p.u. so that there are 18 buses experiencing an under-voltage with the worst being 0.937 p.u. on bus 118. Note that for this particular case, we did not include results for an exhaustive search of the transformer tap settings since the number of combinations with the hardware available is 33^9. Therefore we cannot obtain a solution in a reasonable amount of time. In contrast, the centralized convex relaxation took 71.5 s of CPU time to reach the solution.

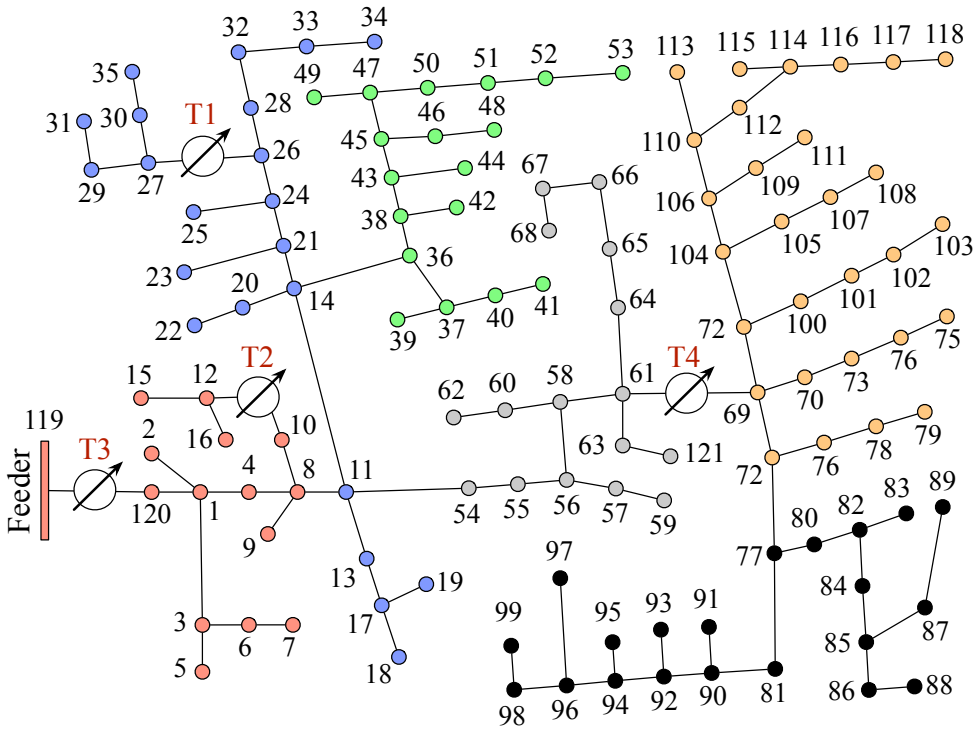

Figure 3.10: Partitioned IEEE 123-bus distribution system.

In this case, we have that $\boldsymbol{W} \in \mathbb{C}^{259\times 259}$ and the centralized relaxed OPF has 268,854 optimization variables. The centralized algorithm yielded a solution in which the tap positions are set to the neutral position, i.e., position 0, for regulators T1 and T2; are set to $\{-5,-1,-3\}$ for regulator T3; and are set to $\{-2,-1,-1\}$ for regulator T4. The minimum voltage is raised to 0.985 p.u. and the network losses are 0.8286 p.u. The bus voltage error between the continuous and the rounded discrete tap positions has an average of 6.63×10^{-4} p.u. and a standard deviation of 0.0017 p.u. with a maximum error of 0.0029 p.u.

In contrast, the distributed algorithm results in 59,436 optimization variables, which is a 77.89% reduction from the centralized scheme. The distributed method returned slightly different results for the tap positions: regulators T1 and T2 taps are set to the neutral position, regulator T3 taps are set to $\{-4,-1,-2\}$, and regulator T4 taps are set to $\{0,1,0\}$. The minimum voltage in this configuration is 0.965 p.u. on bus 118. However, the minimum computed network losses for this configuration are 0.8303 p.u., which

represents a 0.3% difference from the centralized result. For this particular network and loading, the tap positions of regulator T3 impact the network conditions the most since this transformer is connected to the feeder. As the number of transformers on the network increases, there could be multiple solutions that minimize the cost function.

3.5.3 Impact of the Choice of z_t

Next, we explore the impact of the z_t on the solution of the 15-bus, unbalanced three-phase optimization; the results are captured in Figs. 3.11–3.14. In each figure, the thick red vertical line represents the resistance of the neighboring distribution line segments. The vertical lines to the left and right represent values of z_t that are an order of magnitude less and two orders of magnitude larger than that of the neighboring distribution line segments, respectively.

The objective function for this particular case is of the form

$$f(\boldsymbol{W}) = f_0(\boldsymbol{W}) + \sum_{i \in \mathcal{N}} (1 - [\boldsymbol{W}]_{ii})^2 \,, \tag{3.36}$$

where the summation term penalizes the voltage deviations from 1 p.u. Figure 3.11 shows the optimization variables $S_{p_t s'_t}$ for the power transferred through the transformer and the phase difference $\theta_{p_t} - \theta_{s'_t}$ between the primary and secondary sides of the transformer versus the impedance of z_t. In Fig. 3.12 we plot the power transferred through z_t and the rank of the $\boldsymbol{W}$ returned from the convex optimization. In Fig. 3.13 we show cost function $f(\boldsymbol{W})$ and the normalized percent error

$$e\left(\boldsymbol{W}, \boldsymbol{V}(\boldsymbol{a}_t)\right) = 100 \sqrt{\sum_{i \in \mathcal{N}} \left(\frac{\sqrt{[\boldsymbol{W}]_{ii}} - |V_i(\boldsymbol{a}_t)|}{|V_i(\boldsymbol{a}_t)|} \right)^2} \,, \tag{3.37}$$

which is determined by the difference between the voltage magnitudes recovered from $\boldsymbol{W}(z_t)$ and the voltage magnitudes shown in Fig. 3.14 that are computed from the power flow with rounded discrete tap positions.

In Section 3.3.2, we proposed to choose $|z_t|$ several orders of magnitude larger than the impedance of the adjacent distribution line segments. For the 15-bus system, the optimization solution tends to match the power flow

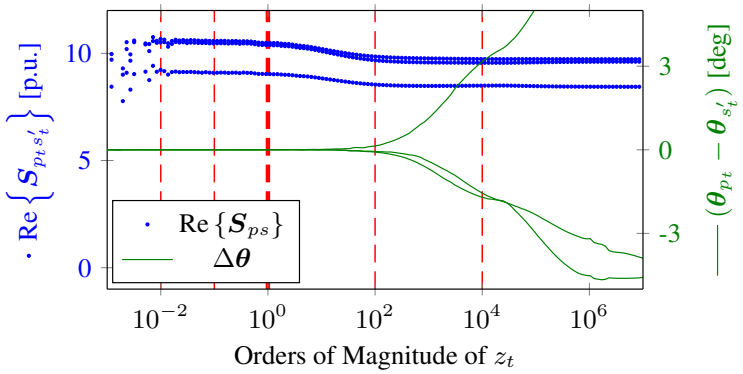

Figure 3.11: Power transferred through $\boldsymbol{S}_{p_t s_t'}$ and phase mismatch between p_t and s_t' versus $|z_t|$.

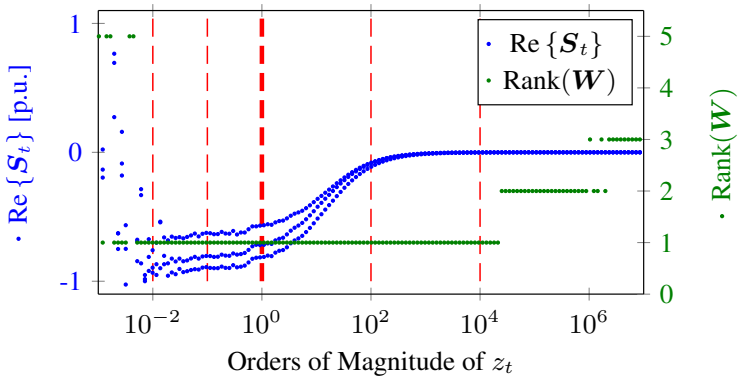

Figure 3.12: Power transferred through z_t and the rank of $\boldsymbol{W}$.

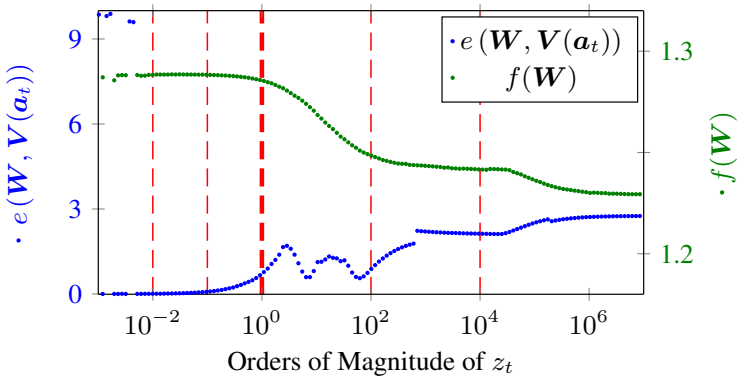

Figure 3.13: Normalized percentage of the voltage error and the objective function in the form $f(\boldsymbol{W}) = f_0(\boldsymbol{W}) + f_2(\boldsymbol{W})$.

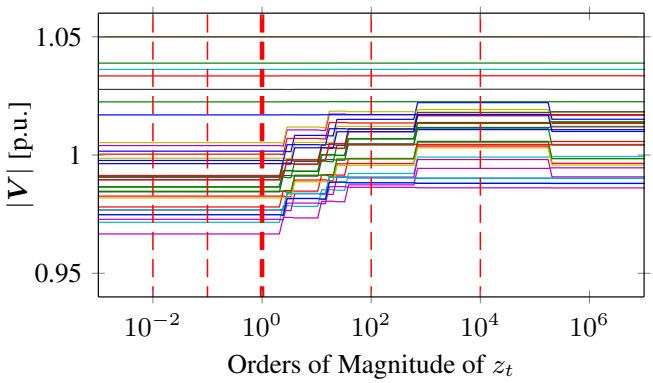

Figure 3.14: Power flow results for bus voltages from rounded tap positions.

results better for small values of z_t; the desired results were captured when z_t is chosen such that $|z_t|$ is two to four orders of magnitude larger than the magnitude of the impedance of neighboring distribution lines. Within this interval, the power transferred through z_t converges to zero and the system values in the optimization converge to a steady-state. We also see that the rank of $\boldsymbol{W}$ is still one with a subtle discrepancy in the angle difference across the transformer of less than 3 degrees and a normalized voltage magnitudes error of less than 2% between the power flow results and the resulting $\boldsymbol{W}(z_t)$. After four orders of magnitude difference, the system behaves as the disconnected case and we are no longer able to accurately recover the solution. Note that these results are for this specific case. In other scenarios we have found that $|z_t|$ approximately two orders of magnitude larger than the neighboring distribution line segments is a good choice for an initial value.

3.6 Summary

In this chapter, we developed a method to optimally set, via a distributed ADMM-based algorithm, tap positions of voltage regulation transformers in distribution systems. We demonstrated the applicability of this method via numerical examples involving single- and three-phase test systems.

CHAPTER 4

FAST TIME-SCALE: A FEEDBACK-BASED APPROACH

In this chapter, we provide a feedback control scheme for tracking a specified voltage profile by controlling the reactive power injections provided by fast time-scale actuators, i.e., reactive power capable distributed energy resources (DERs). A local controller on each bus of the network monitors the bus voltage and, whenever there is a voltage violation, it uses locally available information to estimate the amount of reactive power that needs to be injected into the bus in order to correct the violation. If the DERs connected to the bus can collectively provide the reactive power estimated by the local controller, they are instructed to do so; otherwise, we introduce a secondary distributed control to supplement the primary control when certain resources hit their limits. This distributed 'fair-splitting' algorithm is also utilized for bus-level reactive power management discussed in Chapter 2.

4.1 Introduction

Our proposed feedback control scheme consists of two stages. In the first stage, the voltages at certain buses in the network are monitored by a local controller. If the local controller at a particular bus senses that its voltage is above or below certain thresholds imposed by performance specifications (e.g., $\pm 5\%$ around a nominal value [4]), it will first estimate the amount of reactive power that should be injected into the bus to clear the voltage violation. This estimate is obtained by using the sensitivity of the bus voltage magnitude to changes in reactive power injections in the same bus. Then, if the DERs directly connected to the bus can provide the estimated reactive power, they will be instructed to do so; otherwise, they will output their maximum/minimum capacity. In the second stage, the difference in reactive power between the local controller estimate and what the DERs connected to

the bus can provide will be requested from other buses that have additional capacity. Through a distributed algorithm that only requires an exchange of information among neighboring controllers (e.g., through wireless or power line communications), each local controller calculates its fair contribution to meet the additional request. The proposed algorithm for DER control has similarities with consensus algorithms that have been studied extensively in the field of control (e.g., see [62] and the references therein).

The remainder of this chapter is organized as follows. Section 4.2 provides the distribution system model used for control design purposes, and the communication network model used to describe the exchange of information between local controllers. The proposed two-stage feedback control scheme is presented in Section 4.3, while Section 4.4 illustrates its operation on an 8-bus network and Section 4.5 shows its operation with the two time-scale architecture. Concluding remarks are presented in Section 4.6.

4.2 System Model

In this section, we develop a power distribution system model, which is used in Section 4.3 to design the feedback control system; this model describes the evolution of bus voltage magnitudes as active and reactive power injections change over time. Additionally, we introduce the network communication model that describes the exchange of information between the local controllers that are geographically dispersed throughout the electrical network.

4.2.1 Power Distribution Network

Consider a distribution system with $n+1$ buses indexed by $i = 0, 1, \ldots, n$. At time instants $r = 0, 1, \ldots,$ the voltage magnitude and angle of bus i are denoted by $V_i[r]$ and $\theta_i[r]$, respectively. We assume that bus 0 is the feeder and will be treated as an infinite bus; therefore, $V_0[r]$ and $\theta_0[r]$ remain constant for all r. The remaining n buses are considered to be PQ buses. Let $V[r] = [V_1[r], V_2[r], \ldots, V_n[r]]^T$ denote the vector of bus voltage magnitudes and $\theta[r] = [\theta_1[r], \theta_2[r], \ldots, \theta_n[r]]^T$ denote the vector of bus voltage angles (both $V_0[r]$ and $\theta_0[r]$ are omitted). At time instant r, let $P_i[r]$ and $Q_i[r]$ be the active and reactive power injections in bus i, respectively; the corresponding

active and reactive power injection vectors at the PQ buses are denoted by $P[r] = [P_1[r], P_2[r], \ldots, P_n[r]]^T$ and $Q[r] = [Q_1[r], Q_2[r], \ldots, Q_n[r]]^T$. We define $\Delta V[r] = V[r+1] - V[r]$ and $\Delta\theta[r] = \theta[r+1] - \theta[r]$ as the vectors describing small variations in voltage magnitudes and angles between times r and $r+1$; while variations in active and reactive power injections at PQ buses are defined as $\Delta P[r] = P[r+1] - P[r]$ and $\Delta Q[r] = Q[r+1] - Q[r]$. Then,

$$\begin{bmatrix} \Delta P[r] \\ \Delta Q[r] \end{bmatrix} = \begin{bmatrix} H & N \\ K & L \end{bmatrix} \begin{bmatrix} \Delta\theta[r] \\ \Delta V[r] \end{bmatrix}, \tag{4.1}$$

where

$$H = \left[\frac{\partial P_i}{\partial \theta_j}\right], N = \left[\frac{\partial P_i}{\partial V_j}\right], K = \left[\frac{\partial Q_i}{\partial \theta_j}\right], L = \left[\frac{\partial Q_i}{\partial V_j}\right].$$

[Note that all of the partial derivatives defining the entries of H, N, K, and L are evaluated at $V[r]$, $\theta[r]$, $P[r]$, $Q[r]$, and therefore H, N, K, and L are functions of r; however, in the remainder, we suppress the argument for ease of notation.]

A standard assumption used in the analysis of transmission systems is that the entries of H, L are much larger than the entries of N, K. This effectively decouples (4.1) so that variations in active power injections primarily affect bus voltage angles, whereas variations in reactive power injections directly affect bus voltage magnitudes. This is a consequence of the fact that the per unit reactance to the per unit resistance ratio of transmission lines, commonly referred to as "x/r ratio", is large [63]. In the case of a distribution system, this assumption is not valid since the transmission line x/r ratios are much lower [7]. As a result, in distribution systems, bus voltages are much more sensitive to changes in active power than typically observed in transmission systems.

In our setting, $\Delta P[r]$ describes the changes in active power injections that arise from DERs, e.g., PV rooftop installations and PHEVs, and represents an external "disturbance" over which we do not have control. These injections will have a noticeable impact on the network voltage profile. To mitigate the effect of $\Delta P[r]$ on system voltages, we assume that we have control over $\Delta Q[r]$. We are interested in the effect that uncontrolled variations in active power and controlled variations in reactive power injections have on bus voltage magnitudes. Assuming that H is invertible, then it follows from

(4.1) that $\Delta\theta[r] = -H^{-1}N\Delta V[r] + H^{-1}\Delta P[r]$, and

$$\begin{aligned}\Delta V[r] &= (L - KH^{-1}N)^{-1}(\Delta Q[r] - KH^{-1}\Delta P[r]) \\ &= S\Delta Q[r] + w[r],\end{aligned} \tag{4.2}$$

where $S \equiv (L - KH^{-1}N)^{-1}$ is assumed to be invertible, and $w[r] \equiv -(L - KH^{-1}N)^{-1}KH^{-1}\Delta P[r]$ captures the effect of uncontrolled variations in active power injections on bus voltage magnitude. Now, by unwrapping (4.2), the recurrence relation that describes how the bus voltage magnitudes evolve with time is given by

$$V[r+1] = V[r] + S\Delta Q[r] + w[r]. \tag{4.3}$$

Although we did not make it explicit, the matrix S is in general a function of r. On the other hand, the variations of S with r are relatively small for a wide range of operating conditions [63]. In this regard, we verified that the entries of S typically remain within 3% of their average value for a wide range of operating conditions for the test systems.

4.2.2 Network Communication

It is assumed that certain buses of the electrical network have a local controller that can monitor the bus voltage and make local control decisions based on the exchange of information with a subset of other controllers. Some of these controllers may be located at buses that are directly connected to the bus of the given controller, but, in general, the exchange of information between the n controllers can be arbitrary. It is convenient to capture this exchange of information between local controllers by a *directed graph* $\mathcal{G}_d = \{\mathcal{V}, \mathcal{E}\}$, where $\mathcal{V} = \{1, 2, ..., n\}$ represents the set of vertices (nodes, which represent the controllers), and $\mathcal{E} \subseteq \mathcal{V} \times \mathcal{V}$ represents the set of directed edges, i.e., $(j, i) \in \mathcal{E}$ when node j can receive information from node i. By convention, we assume that self-loops are not contained in $\mathcal{E}$. All of the nodes that can send information to node j are said to be the in-neighbors of node j and are represented by the set $\mathcal{N}_j^- = \{i \in \mathcal{V} : (j, i) \in \mathcal{E}\}$. The cardinality of $\mathcal{N}_j^-$ is called the in-degree of node j and is denoted by $\mathcal{D}_j^-$. The nodes that can receive information from node j are called its out-neighbors and are represented by the set $\mathcal{N}_j^+ = \{l \in \mathcal{V} : (l, j) \in \mathcal{E}\}$; the out-degree of

node j is $\mathcal{D}_j^+$. A directed graph is considered *strongly connected* if any two vertices $i, j \in \mathcal{V},\ i \neq j$, can be joined by a path that starts at node i and ends at node j.

4.3 Two-Stage Feedback Control Scheme

In this section, we first provide an overview of the proposed two-stage feedback control scheme. Then we formulate each of the stages that comprise the architecture and analyze their stability and convergence properties.

4.3.1 Overview

Figure 4.1 shows the timeline for the operation of the two stages. Without loss of generality, assume that at each bus j of the network, there is a local controller that monitors the bus voltage magnitude V_j. At fixed time instants $r = \lfloor k/k_0 \rfloor,\ k = 0, 1, \ldots$, for some sufficiently large k_0 (to be precisely defined later), each local controller executes the first stage. In this stage, if the local controller on bus j detects a voltage violation, i.e., V_j is outside specifications, it estimates the amount of reactive power that, if injected (or consumed) in bus j, will correct the violation; then, if the DERs connected to bus j collectively have the capacity to inject (or consume) the estimated reactive power request, the controller instructs these DERs to do so. Otherwise, the local controller will execute the second stage by initiating a request for an additional amount of reactive power to be injected in other buses of the network to help clear its voltage violation. This request is relayed by the local controller to other neighboring local controllers through a distributed iterative algorithm that ensures that nodes with available reactive power capacity will provide additional support.

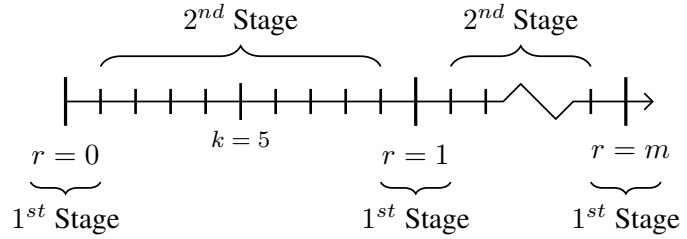

Figure 4.1: Timeline for the execution of the first and second control stages.

The second stage exploits the sensitivity of V_j to reactive power injections in neighboring buses and has a net effect of a globally homogeneous raising (or lowering) of all the bus voltages. This effect is similar to the one that results from adjusting the taps on a TCUL transformer or a SVR in the sense that it affects all bus voltages; however, there are some differences. In particular, the action of a TCUL, or a VR, will *uniformly* raise (or lower) the voltage across the network. In the two-stage control architecture, the reactive power injections in bus j will primarily affect the voltage at this bus and the voltages at buses downstream of it (in a radial system), with the effect attenuating as we move towards the feeder. It is important to note that the proposed voltage control architecture is not intended to replace current voltage control systems, but rather to supplement their action while (i) minimizing their usage by handling faster voltage variations due to changes in renewable-based power injections, and (ii) having them intervene only during extreme circumstances rather than minor, possibly temporary, violations.

4.3.2 First Stage

At time instants $r = 0, 1, \ldots$, the local controller located on bus j measures the voltage $V_j[r]$. If it detects a voltage violation (i.e., $V_j[r] \notin [\underline{V}_j, \overline{V}_j]$, where $\overline{V}_j$ and $\underline{V}_j$ are bus j's upper and lower voltage limits, respectively), then the local controller will estimate the amount of additional reactive power $\rho_j[r]$ needed to clear the violation. In the first stage, we assume that the controller at bus j does not have voltage information for other buses available. Therefore, the estimate of $\rho_j[r]$ is given by

$$\rho_j[r] = \begin{cases} \dfrac{\alpha}{s_{jj}}(\underline{V}_j - V_j[r]), & V_j[r] < \underline{V}_j, \\ 0, & \underline{V}_j \leq V_j[r] \leq \overline{V}_j, \\ \dfrac{\alpha}{s_{jj}}(\overline{V}_j - V_j[r]), & \overline{V}_j < V_j[r], \end{cases} \tag{4.4}$$

where $\alpha > 0$ is some constant (to be made precise later) and $s_{jj} = \partial V_j / \partial Q_j$. Thus, if the DERs connected to each bus j collectively have the capacity (with respect to their previous demand) to provide $\rho_j[r]$, then the net change in reactive power injections for all of the nodes in the network is given by $\Delta Q[r] \equiv \rho[r]$, where $\rho[r] = [\rho_1[r], \rho_2[r], \ldots, \rho_n[r]]^T$ (assuming that the re-

active power consumed by loads does not substantially change). Next, we provide a condition on the value that α must take to ensure the stability of the closed-loop system that results from applying $\Delta Q[r] \equiv \rho[r]$ to (4.3).

Choice of α for Stability

Note from (4.4) that, by defining

$$V_j^{ref}[r] = \begin{cases} \underline{V}_j, & V_j[r] < \underline{V}_j, \\ V_j[r], & \underline{V}_j \leq V_j[r] \leq \overline{V}_j, \\ \overline{V}_j, & \overline{V}_j < V_j[r], \end{cases} \tag{4.5}$$

we can write

$$\Delta Q[r] \equiv \rho[r] = \alpha D \left(V^{ref}[r] - V[r] \right), \tag{4.6}$$

where $V^{ref}[r] = [V_1^{ref}[r], [V_2^{ref}[r], \ldots, V_n^{ref}[r]]^T$, $\alpha > 0$, and D is a diagonal matrix with $d_{ii} = 1/s_{ii}$. Then, by substituting (4.6) into (4.3), we get

$$V[r+1] = (I - \alpha SD)\, V[r] + \alpha SD V^{ref}[r] + w[r], \tag{4.7}$$

with $V^{ref}[r]$ as defined in (4.5), from where it is easy to see that $V^{ref}[r]$ is bounded for all r. Also, from the definition of $w[r]$ in (4.3), it is obvious that $w[r]$ is also bounded for all r.

Then, since the system (4.7) is a linear time-invariant system driven by bounded inputs $V^{ref}[r]$ and $w[r]$, ensuring the stability of this system, i.e., that $V[r]$ remains bounded for all r, is equivalent to ensuring that the system is internally stable (see, e.g., [64]), i.e., the eigenvalues of $(I - \alpha SD)$ must lie within the unit circle. This can be accomplished by choosing α such that

$$\alpha < \alpha_c = \min_i \left\{ \frac{2\,\mathrm{Re}\{\lambda_i\}}{|\lambda_i|^2} \right\}, \tag{4.8}$$

where $\lambda_i = \mathrm{Re}\{\lambda_i\} + j\,\mathrm{Im}\{\lambda_i\}$ denotes the i^{th} eigenvalue of SD. The derivation of (4.8) is included in Appendix C.1.

Remark: The developments above assume a fixed electrical network configuration that results in a single S; however, the control system should be able to adapt to configuration changes (potentially resulting in different S's) and ensure that the system in (4.7) is stable for all possible configurations. In this regard, we envision that the local controller at each bus j could have a database, calculated off-line, with the value of s_{jj} and α corresponding to each network configuration. Then, upon a change in configuration, the local controllers would be notified, and they would update α and the s_{jj}'s accordingly.

■

Practical Considerations for Implementation

The action of (4.6) on the system dynamics as defined by (4.3), which results in (4.7), is equivalent to those of a discrete-time integrator. Thus, whenever there is a voltage violation at bus j, the action of the first stage controller will asymptotically drive the voltage V_j to either $\overline{V}_j$ or to $\underline{V}_j$ depending on the nature of the violation. In practice, it is desirable that the first stage stops iterating after a finite number of steps r_0. In order to achieve this, in (4.4), we replace $\overline{V}_j$ by $\overline{V}_j - \varepsilon_1$ and $\underline{V}_j$ by $\underline{V}_j + \varepsilon_1$ for some $\varepsilon_1 > 0$ small. The result is such that, for any $\varepsilon_1 > 0$, there is some finite r_0 such that $V_j[r] \in [\underline{V}_j, \overline{V}_j]$ for all $r \geq r_0$ and all j; thus the controller action stops after r_0 steps.

In all our numerical experiments, we verified that letting $\alpha = 1/n$ (where n is the number of buses in the network with the feeder omitted) be the default gain satisfies the condition in (4.8). This choice of α may not necessarily result in the shortest settling time; however, it helps prevent overshoots if several local controllers are acting simultaneously. In this regard, we have observed that S is in general a full matrix the entries of which are usually on the same order of magnitude, except for those associated with buses that are farthest apart; i.e., buses at the end of a sublateral have a low voltage sensitivity with respect to injections into buses near the feeder, and vice versa. This implies that injections of reactive power at any bus affect (to varying degrees) all other bus voltages throughout the network. Furthermore, for typical distribution system line parameter values, the column and row sums of SD are typically well below $1.5n$, so scaling the contribution of each bus by

$1/n$ ensures that the spectral radius of SD is less than 2 [65]. This accounts for the worst-case scenario in which all the buses are subject to either under-voltage or over-voltage violations. Finally, it is worth noting that the local controllers can easily estimate n using a distributed algorithm similar to the one to be described in Section 4.3.3.

4.3.3 Second Stage

If the reactive power estimate $\rho_j[r]$ is within the limits that the DERs connected to bus j can provide for all j, then the second stage is not required at step r. Otherwise, the second stage compensates for the capacity constraint violations from the first stage by adjusting every node's contributions to globally raise, or lower, bus voltages across the network. This is accomplished through a distributed algorithm that relies on a local exchange of information among neighboring controllers. We assume that the graph that describes the exchange of information between local controllers is strongly connected, but not necessarily complete, i.e., it is not necessarily the case that each node can communicate directly with every other node in the graph.

Let $\underline{q}_j$, $\overline{q}_j$, where $\underline{q}_j \leq 0 \leq \overline{q}_j$, be the total lower and upper limits on the amount of reactive power that DERs at bus j can provide. Let $q_j[r]$ be the amount of reactive power provided by the DERs connected to bus j at instant r.[1] Then, assuming that $\underline{q}_j \leq q_j[r] \leq \overline{q}_j \ , \forall j$, the total estimated reactive power to be provided by node j is

$$\hat{q}_j[r+1] = q_j[r] + \rho_j[r], \tag{4.9}$$

where $\rho_j[r]$ is the estimate from (4.4). Then, if $\underline{q}_j \leq \hat{q}_j[r+1] \leq \overline{q}_j \ , \forall j$, the second stage is not necessary, i.e., every node j can provide itself the amount of reactive power estimated in the first stage. Otherwise, whenever $\hat{q}_j[r+1] \geq \overline{q}_j$ or $\hat{q}_j[r+1] \leq \underline{q}_j$, for some j (which means that at least one node cannot correct its voltage violation by itself), the buses that have additional capacity will calculate the amount of reactive power they need to provide

[1] In (4.3), we defined $\Delta Q_j[r] = Q_j[r+1] - Q_j[r]$, where $Q_j[r]$ is the *total* reactive power injection (with appropriate sign) in bus j that arises from both DERs and loads, i.e., $Q_j[r] = q_j[r] + q_j^L$, where q_j^L denotes the (uncontrolled) reactive power injection arising, e.g., from loads, which is assumed to remain constant, i.e., $\Delta Q[r] = Q[r+1] - Q[r] = q[r+1] - q[r]$.

in an attempt to raise the voltage in the network through the distributed iterative algorithm described next.

Second Stage 'Fair-Splitting' Algorithm

Let $\mathcal{G} = \{\mathcal{V}, \mathcal{E}\}$ be a strongly connected directed graph describing the exchange of information between local controllers. Each node $j \in \mathcal{V}$ maintains three auxiliary variables $\mu_j[k]$, $\overline{\nu}_j[k]$, and $\underline{\nu}_j[k]$, and updates them to $\mu_j[k+1]$, $\overline{\nu}_j[k+1]$, and $\underline{\nu}_j[k+1]$, respectively, via a weighted linear combination of their previous $\mu_j[k]$, $\overline{\nu}_j[k]$, and $\underline{\nu}_j[k]$, respectively, and those of its in-neighbors, i.e., $\{\mu_i[k] \mid i \in \mathcal{N}_j^-\}$, $\{\overline{\nu}_i[k] \mid i \in \mathcal{N}_j^-\}$, and $\{\underline{\nu}_i[k] \mid i \in \mathcal{N}_j^-\}$, respectively; specifically,

$$\mu_j\left[k+1\right] = \sum_{i \in \{\mathcal{N}_j^-\} \cup \{j\}} \frac{1}{1+\mathcal{D}_i^+} \mu_i\left[k\right], \tag{4.10}$$

$$\overline{\nu}_j\left[k+1\right] = \sum_{i \in \{\mathcal{N}_j^-\} \cup \{j\}} \frac{1}{1+\mathcal{D}_i^+} \overline{\nu}_i\left[k\right], \tag{4.11}$$

$$\underline{\nu}_j\left[k+1\right] = \sum_{i \in \{\mathcal{N}_j^-\} \cup \{j\}} \frac{1}{1+\mathcal{D}_i^+} \underline{\nu}_i\left[k\right], \tag{4.12}$$

where $\mathcal{D}_i^+$ is the out-degree of node i. Each node j sets its initial conditions in (4.10)–(4.12) respectively to

$$\mu_j[0] = \begin{cases} \hat{q}_j[r+1] - \overline{q}_j, & \hat{q}_j[r+1] > \overline{q}_j, \\ \hat{q}_j[r+1] - \underline{q}_j, & \hat{q}_j[r+1] < \underline{q}_j, \\ 0, & \text{otherwise}, \end{cases} \tag{4.13}$$

$$\overline{\nu}_j[0] = \begin{cases} \overline{q}_j - \hat{q}_j[r+1], & \hat{q}_j[r+1] < \overline{q}_j, \\ 0, & \hat{q}_j[r+1] \geq \overline{q}_j, \end{cases} \tag{4.14}$$

$$\underline{\nu}_j[0] = \begin{cases} \underline{q}_j - \hat{q}_j[r+1], & \hat{q}_j[r+1] > \underline{q}_j, \\ 0, & \hat{q}_j[r+1] \leq \underline{q}_j. \end{cases} \tag{4.15}$$

Then, at every step k, for each j such that $\underline{\nu}_j[k] \neq 0$ or $\overline{\nu}_j[k] \neq 0$, the corresponding local controller computes

$$\eta_j[k] = \begin{cases} \dfrac{\mu_j[k]}{\underline{\nu}_j[k]}\underline{\nu}_j[0], & \mu_j[k] < 0, \\ \\ \dfrac{\mu_j[k]}{\overline{\nu}_j[k]}\overline{\nu}_j[0], & \mu_j[k] \geq 0, \end{cases} \tag{4.16}$$

where $\eta_j[k]$ will asymptotically converge to

$$\eta_j = \begin{cases} \dfrac{\sum_{i=1}^n \mu_i[0]}{\sum_{i=1}^n \underline{\nu}_i[0]}\underline{\nu}_j[0], & \lim_{k\to\infty} \mu_j[k] < 0, \\ \\ \dfrac{\sum_{i=1}^n \mu_i[0]}{\sum_{i=1}^n \overline{\nu}_i[0]}\overline{\nu}_j[0], & \lim_{k\to\infty} \mu_j[k] \geq 0; \end{cases} \tag{4.17}$$

the derivation of this result can be found in Appendix C.2 and is the ratio consensus algorithm from [66].

From (4.17), it is obvious that $\sum_{j=1}^n \eta_j = \sum_{j=1}^n \mu_j[0]$, i.e., the total amount of reactive power (including both positive and negative contributions) that constrained nodes cannot provide remains asymptotically constant. Also, $\eta_j \leq \overline{\nu}_j[0]$ if $\lim_{k\to\infty} \mu_j[k] \geq 0$ and $\eta_j > \underline{\nu}_j[0]$ if $\lim_{k\to\infty} \mu_j[k] < 0$. Finally, bus j adjusts its reactive power contribution to

$$q_j[r+1] = \begin{cases} \overline{q}_j, & \hat{q}_j[r+1] + \eta_j > \overline{q}_j, \\ \underline{q}_j, & \hat{q}_j[r+1] + \eta_j < \underline{q}_j, \\ \hat{q}_j[r+1] + \eta_j, & \text{otherwise.} \end{cases} \tag{4.18}$$

From the developments above, it follows that the additional reactive power to be requested in the second stage will either be a net injection or a net consumption. In this regard, it is reasonable to assume that a distribution network will typically experience one type of voltage violation at any given moment. Simultaneous over- and under-voltage violations would imply that the distribution system lines have substantial losses, which is unlikely in real systems; however, we assume that this is a possibility. Thus, each node j maintains $\overline{\nu}_j[k]$ and $\underline{\nu}_j[k]$, and computes the appropriate solution in (4.17) once $\mu_j[k]$ converges.

Effect of Network Connectivity on Convergence Speed

For any strongly connected graph $\mathcal{G} = \{\mathcal{V}, \mathcal{E}\}$ describing the exchange of information between local controllers, the steady-state solution of the distributed algorithm in (4.17) is independent of $\mathcal{G}$. However, for a given size of the vertex set $\mathcal{V}$, the connectivity between the nodes as described by $\mathcal{E}$, which determines the weights in (4.10)—(4.12), affects the convergence speed of the distributed algorithm. In this regard, by letting $\mu[k] = [\mu_1[k], \mu_2[k], \ldots, \mu_n[k]]^T$, $\overline{\nu}[k] = [\overline{\nu}_1[k], \overline{\nu}_2[k], \ldots, \overline{\nu}_n[k]]^T$, and $\underline{\nu}[k] = [\underline{\nu}_1[k], \underline{\nu}_2[k], \ldots, \underline{\nu}_n[k]]^T$, and defining a matrix $P = [p_{ji}]$, with

$$p_{ji} = \begin{cases} \frac{1}{1+\mathcal{D}_j^+}, & j = i, \\ \frac{1}{1+\mathcal{D}_i^+}, & j \neq i,\ (j,i) \in \mathcal{E}, \\ 0, & j \neq i,\ (j,i) \notin \mathcal{E}, \end{cases} \tag{4.19}$$

then, we can write the iterations in (4.10)—(4.12) in matrix form (as in (C.1)—(C.3) in Appendix C.2). The matrix P is column stochastic and has the same sparsity structure (except for the diagonal entries) as the adjacency matrix of $\mathcal{G}$. Furthermore, since $\mathcal{G}$ is strongly connected, the matrix P is primitive [65]. Now, it is well-known (see, e.g., [65]) that, for some accuracy level ε_0, the second largest eigenvalue modulus $|\lambda_2|$ of P determines the number of iterations k_0 after which $\|\mu[k] - \mu\|_\infty \leq \varepsilon_0$ and $\|\overline{\nu}[k] - \overline{\nu}\|_\infty \leq \varepsilon_0$ ($\|\underline{\nu}[k] - \underline{\nu}\|_\infty \leq \varepsilon_0$), $\forall k \geq k_0$.

In general, the more connected the graph, the faster the algorithm converges, i.e., the smaller k_0 is; however, in order to make a quantitative statement, it is necessary to check the value of $|\lambda_2|$. On the other hand, there are results in the spectral graph theory literature (see, e.g., [67]) that establish upper bounds on $|\lambda_2|$ in terms of the number of nodes and the diameter of $\mathcal{G}$, e.g., the maximum shortest path between any two nodes. In order to determine the execution time of the algorithm, we need to fix the time τ_0 for completing each iteration. In this regard, we have shown in [68] that using commercial off-the-shelf hardware, we can complete an iteration step τ_0 within 10 to 40 ms; should the hardware be designed specifically for this application, the iteration step time τ_0 might be decreased even further. Then, given τ_0 and k_0, the actual time it takes for the distributed algorithm to converge is $\tau_1 = k_0\tau_0$, which in turn determines the minimum time between actions of the first stage.

4.4 Example: 8-bus Distribution System

Consider the 8-bus system shown in Fig. 4.2; operational requirements specify that bus voltage magnitudes must lie within $\pm 5\%$ of 1 p.u. at all times. Line impedance data, system loading data, and the aggregated reactive power capacity limits of the DERs can be found in Appendix C.3, from which the matrices S and D in (4.7) can be obtained. Then, given S and D, and following the notation in (4.8), we obtain that $\alpha_c = 0.4$, thus, for the first stage, the gain α of each local controller needs to be chosen so that $\alpha < \alpha_c$.

4.4.1 Second Stage Implementation

We consider the two communication network topologies displayed in Fig. 4.3. Topology 1 (Fig. 4.3(a)) mirrors the physical network with undirected communication links between the controllers of any two buses that are electrically connected by a line. In Topology 2 (Fig. 4.3(b)), we add bidirectional communication links between nodes 1 & 7 and nodes 5 & 7, as well as make the links between nodes 1 & 2 and nodes 4 & 5 directional (directed from 1 to 2, and from 4 to 5, respectively). For each topology, the matrix P, with entries as defined in (4.19), is given in Appendix C.3. We assume that each iteration of the distributed algorithm requires $\tau_0 = 10$ ms, which is consistent with the experimental findings in [68] (see also discussion in Section 4.3.3). For an accuracy level of $\varepsilon_0 = 10^{-3}$, the algorithm needs $k_0 = 39$ iterations to converge when implemented over Topology 1, and $k_0 = 17$ iterations when implemented over Topology 2. Thus, the time that it takes for the algorithm to converge is 0.39 s for Topology 1 and 0.17 s for Topology 2.

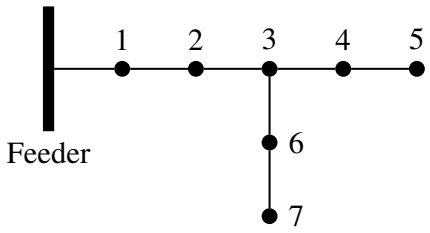

Figure 4.2: 8-bus system: electrical network graph.

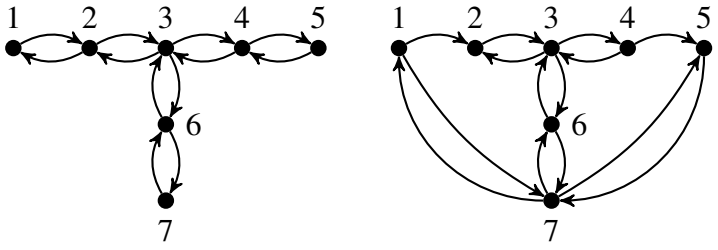

(a) Topology 1. (b) Topology 2.

Figure 4.3: 8-bus system: communication network graphs.

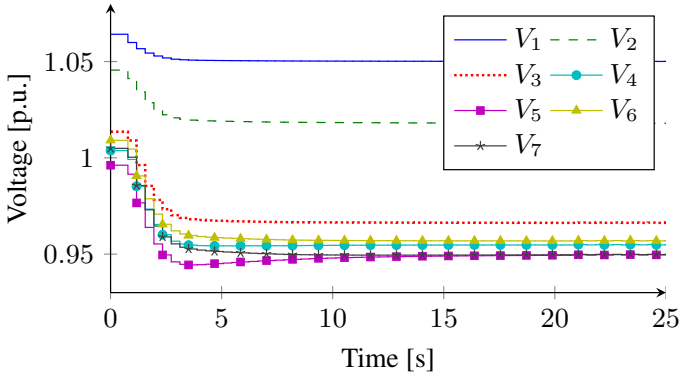

(a) Voltage response.

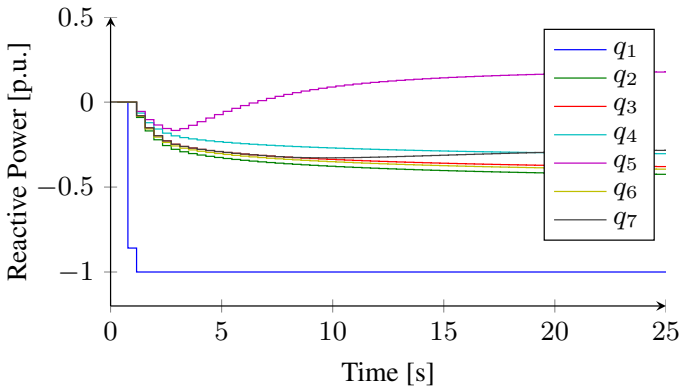

(b) Reactive power support.

Figure 4.4: 8-bus system: response to over-voltage.

4.4.2 System Response for Different Scenarios

Next, we illustrate the operation of the voltage control architecture for both over-voltage and under-voltage violations. Additionally, for the under-voltage violation, and assuming different values of α and ε_1, we study the time it takes for the control system to correct this violation.

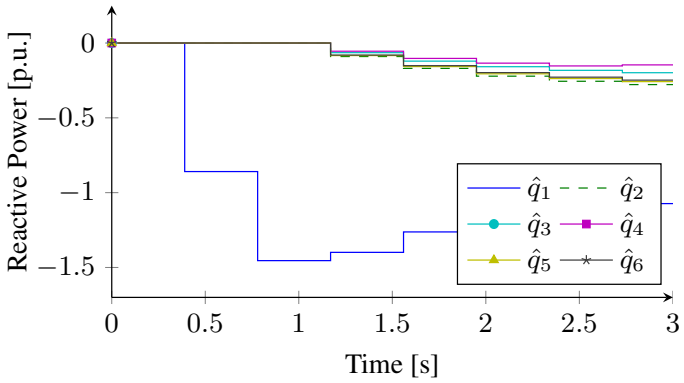

(a) First stage control $\hat{q}$.

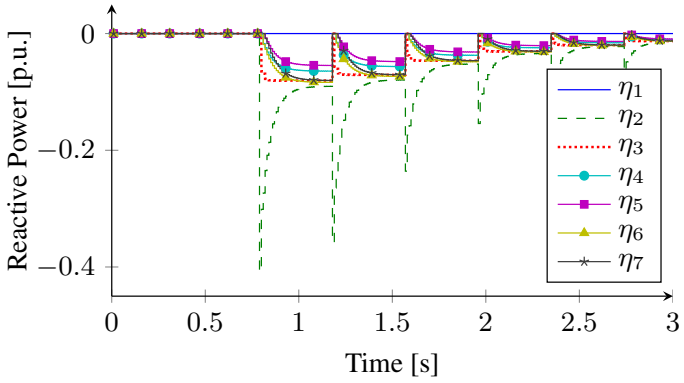

(b) Second stage control η.

Figure 4.5: 8-bus system: first and second stage response to over-voltage.

Feeder Over-Voltage

We consider a scenario in which bus 1 is subject to an over-voltage violation; this could potentially arise if there is a severe over-voltage in the transmission network and the transformers at the substation could no longer adjust their taps to lower the bus voltages. In this case, we assume the feeder's voltage is $1.08\angle 0$ p.u., which results in $V_1 = 1.0642$ p.u. We set the gain of each controller to be $\alpha = 0.3 < \alpha_c = 0.4$. When the second stage is implemented over the network in Fig. 4.3(a), the evolution of the voltage profile in the network is displayed in Fig. 4.4(a) for the first 25 s. The corresponding evolution of reactive power injections that result from the combined action of first and second stages is displayed in Fig. 4.4(b), whereas the individual responses of both stages are displayed in Fig. 4.5 for the first 3 s. In this case, the first stage controller in bus 1 tries to fix the voltage violation by demanding local consumption of reactive power. As can be seen in Fig. 4.4(b), this results in

the reactive power provided by bus 1 reaching its minimum capacity within 1 s. Then, the action of the second stage makes the local controllers in the other buses react in order to bring down the voltage magnitude of bus 1, thus reactive power starts being consumed in these nodes. This causes an under voltage violation in buses 5 and 7. However, the violation is corrected by subsequent actions of the controllers, and the voltage in all buses is restored to values within ±5% of 1 p.u. after approximately 15 s.

Sublateral Under-Voltage

In this case, the feeder voltage is set to $0.98\angle 0$ p.u., which results in under-voltages on buses 2 through 7, with the lowest voltage magnitude of 0.8830 p.u. on bus 5. For the first stage, we set the gain of each local controller to be $\alpha = 0.22$. Figure 4.6(a) shows the evolution of the voltage profile in all

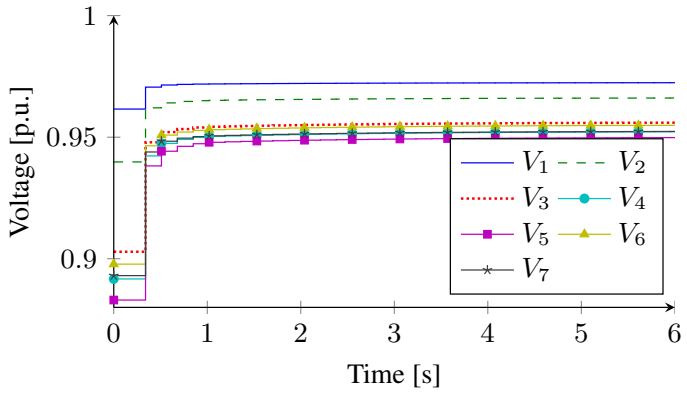

(a) Voltage response.

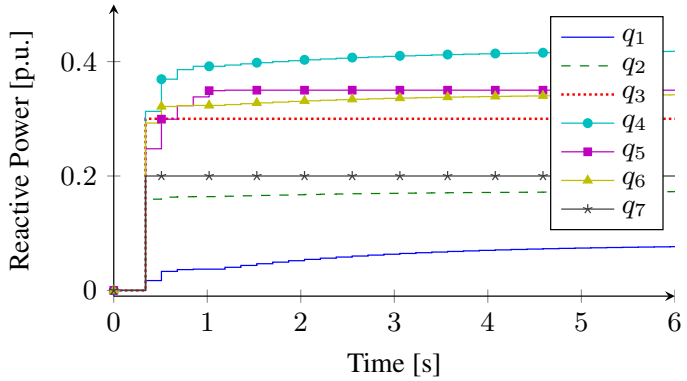

(b) Reactive power support.

Figure 4.6: 8-bus system: system response to under-voltage.

Table 4.1: 8-Bus System: Settling Time for Parameter Values

Accuracy	Controller Gain	Topology	
ε_1	α	Time 1 [s]	Time 2 [s]
10^{-2}	$1/n$	1.17	0.51
	0.22	0.39	0.17
	α_c	0.39	0.17
10^{-3}	$1/n$	5.46	2.38
	0.22	2.34	1.02
	α_c	0.39	0.17
10^{-4}	$1/n$	9.36	4.08
	0.22	4.68	2.04
	α_c	0.39	0.17

nodes when the second stage is implemented over the network in Fig. 4.3(b). In this case, we can see that it takes about 2.1 s to bring the bus voltage magnitudes within the levels specified by operational requirements ($\pm 5\%$ of 1 p.u.). Figure 4.6(b) shows, as time evolves, the reactive power injections on each of the buses that result from the combined actions of first and second stages. In this figure, we can see that the local controllers on buses 2 through 7 swiftly begin to demand reactive power so as to raise their bus voltages. On the other hand, since bus 1 is initially within its voltage limits, the reactive power injection on this bus does not start until other buses reach their reactive power capacity limits. Then, the second stage starts demanding reactive power from any bus that has available capacity, which includes bus 1; thus, the evolution of q_1 is determined by the action of the second stage.

For both communication topologies, Table 4.1 compares the settling times for different values of ε_1 and α. From Table 4.1 and Fig. 4.7, it is clear that the system response is always faster when the second stage is implemented using the communication topology in Fig 4.3(b), where Fig. 4.7 compares the first two intervals of the second stage for Figs. 4.3(a) and 4.3(b), respectively. Additionally, the time it takes for the system to correct a violation can be substantially decreased by choosing α closer to its critical value.

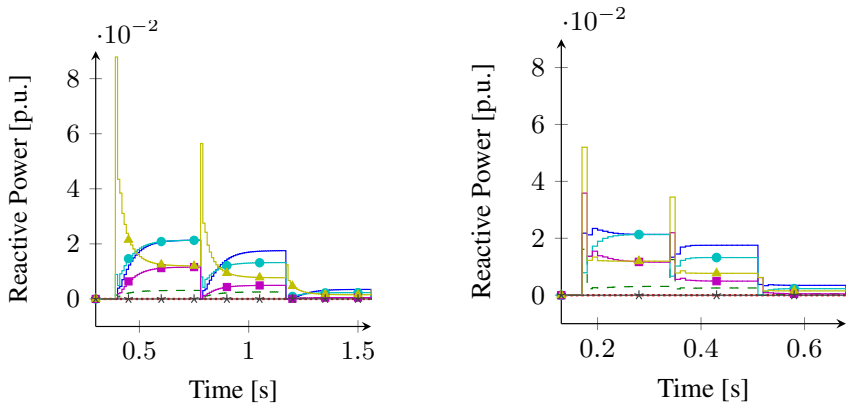

(a) η for Topology 1.

(b) η for Topology 2.

Figure 4.7: 8-bus system: distributed algorithm response to under-voltage.

4.5 Case Study: Two Time-Scale Control

In this section, we demonstrate the interaction between the slow time-scale control scheme presented in Chapter 3, and the fast time-scale control scheme developed in this chapter. We will periodically run the OPF in the slow time-scale control to establish the voltage profile that the fast time-scale control will track. In the slow time-scale control we run two cases: (i) the transformer taps are the only decision variables, and (ii) both the transformer taps and reactive power support are decision variables.

We perform the simulation 15-bus unbalanced three-phase distribution system listed in Appendix E.1. We run the two time-scale control architecture for 400 seconds. The slow time-scale control solves the OPF every 200 seconds, while the controllers for the fast time-scale control sample every second.

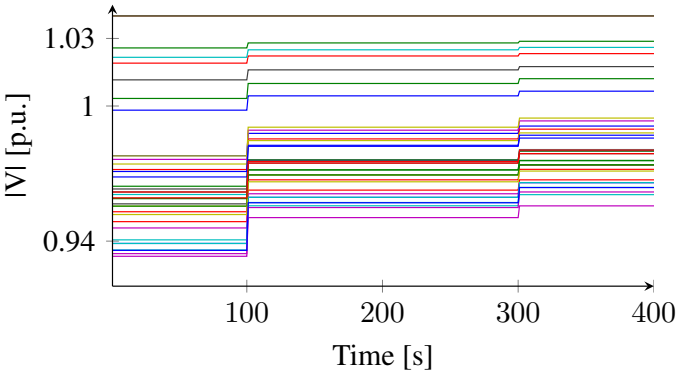

Figure 4.8: Uncontrolled voltage response.

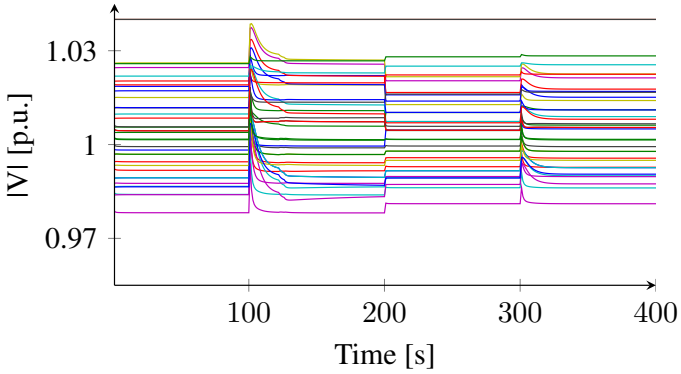

(a) Controlled voltage response.

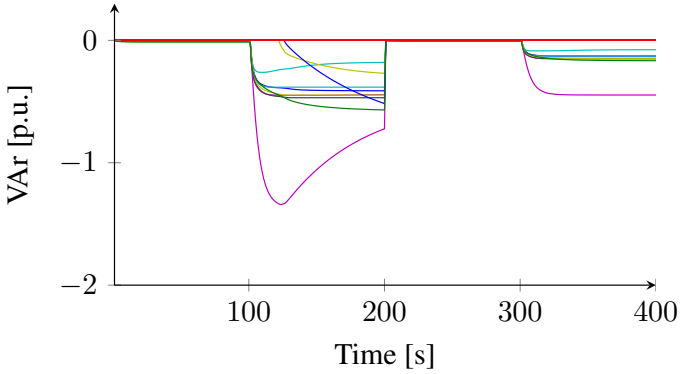

(b) DER reactive power support.

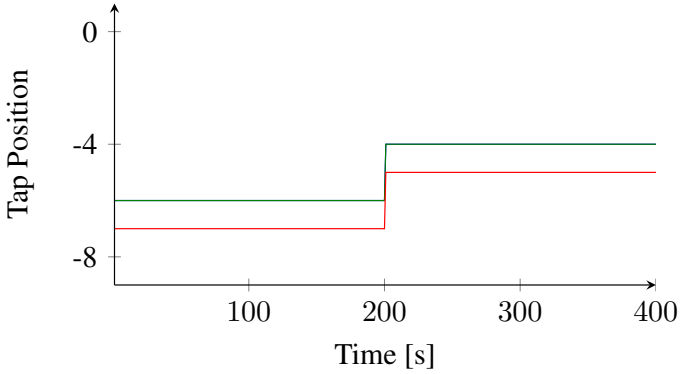

(c) TCUL transformer tap positions.

Figure 4.9: 15-bus, three-phase results with transformer taps only dispatched by slow time-scale control.

In the slow time-scale optimization described in Chapter 3, we dispatch the system to track $V_i^r = 1$ p.u. for all i and the weights w_i are proportional to the distance bus i is from the feeder.

We begin the simulation with the loads at 120% of their specified values. At $t = 100$ s and $t = 300$ s, we change the loads to 105% and 100% of their specified values, respectively. The feeder is set to have a balanced three-phase voltage of 1.04 p.u. The uncontrolled voltage response to the loading is shown in Fig. 4.8. The additional load causes several buses near the end of the sublaterals to experience under voltages with the remaining bus voltages dispersed throughout the acceptable voltage magnitude range of 1 ± 0.05 p.u.

In Fig. 4.9 we show the evolution of the two time-scale control with the decision variables for the slow time-scale control the transformer taps only. The controlled voltage response is shown in Fig. 4.9(a) with the reactive power support and tap positions shown in Figs. 4.9(b) and 4.9(c), respectively. The slow time-scale control is able to keep the bus voltages well within $\pm 3\%$ of 1 p.u.; however, the fast time-scale control is unable return bus voltages to the profile established in the initial dispatch of the transformers due to the significant change in the load. Consequently, the transformers are redispatched at $t = 200$ s. The fast time-scale control is able to return the bus voltages to their desired values with the load change that occurs at $t = 300$ s.

In Fig. 4.10 our decision variables for the slow time-scale control are both the transformer taps and the reactive power support q_i with limited minimum/maximum reactive power capacities $\underline{q}_i$ and $\overline{q}_i$, respectively. Limiting the available capacity of the reactive power support in the slow time-scale control is equivalent to providing a spinning reserve to ensure there will be resources available to track the desired voltage profile specified with the fast time-scale control. The controlled voltage response, reactive power support, and tap positions are shown in Figs. 4.10(a), 4.10(b), and 4.10(c), respectively. Compared to the previous case, the slow time-scale control favors dispatching reactive power to regulate the bus voltages. Clearly, this approach produced an initially voltage profile tighter around 1 p.u.; however, the fast time-scale struggles to track the voltage profile as well. Similar to the first case, the significant change in load at $t = 100$ s requires a new optimal dispatch and the fast time-scale control is able to track the voltage profile for the smaller load change at $t = 300$ s.

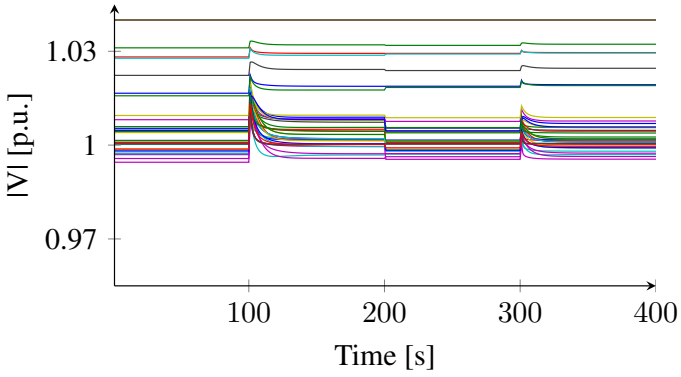

(a) Controlled voltage response.

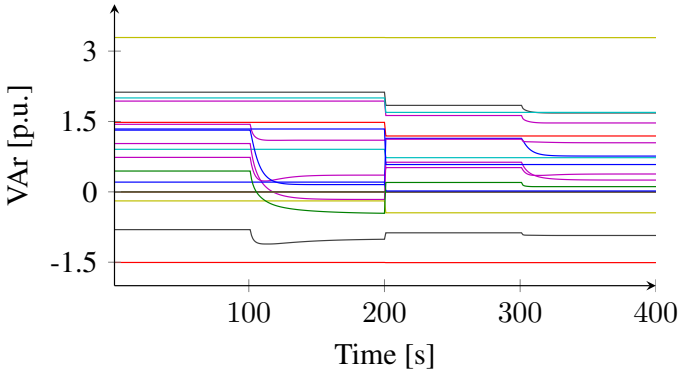

(b) DER reactive power support.

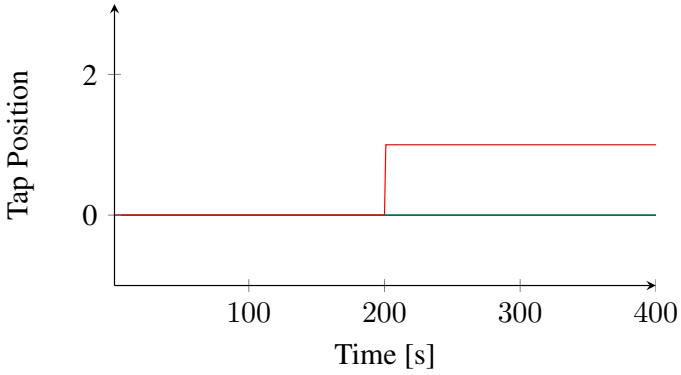

(c) TCUL transformer tap positions.

Figure 4.10: 15-bus, three-phase results with both transformer taps and reactive power dispatched by slow time-scale control.

4.6 Summary

This chapter demonstrates the ability of DERs to shape the voltage profile in distribution networks with reactive power support. The case study in Section 4.5 demonstrates the ability of the method to correct voltage violations, but as demonstrated, it has limited voltage tracking capabilities and is suboptimal. While the second stage can supplement the primary control of the first stage, correcting bus voltages is more of a local problem than the two-stage architecture is designed to handle. To address these concerns, we pursue the optimization-based approach provided in the next chapter.

CHAPTER 5

FAST TIME-SCALE: AN OPTIMIZATION-BASED APPROACH

In this chapter, we propose a fast time-scale control scheme that optimally sets the reactive power contributions of distributed energy resources (DERs) present in distribution systems with the goal of regulating bus voltages. We use the branch power flow modeling approach for radial power systems to formulate an optimal power flow (OPF) problem. Then, we leverage properties of the system operating conditions to relax certain nonlinear terms of this OPF, which results in a convex quadratic program (QP). Furthermore, we provide a distributed algorithm to efficiently solve this QP; this algorithm is based on the Alternating Direction Method of Multipliers (ADMM).

5.1 Introduction

We formulate the voltage regulation problem for a balanced network as a quadratic program (QP) around the operating point determined by the procedure that we proposed in Chapter 3, which optimally sets voltage regulation transformers and provides limited reactive power support. To this end, we leverage a variant of the branch flow model formulation known as the DistFlow (see, e.g., [69–71]). This will allow us to make similar simplifications to those made by the authors of [25,26], and formulate a problem that has linear constraints with a quadratic cost function, which is a convex problem around a particular operating point. Then, we extend the aforementioned formulation for balanced systems to the unbalanced three-phase case by using a similar approach to the linear approximation mentioned in [27]. Finally, in order to efficiently solve these QP problems, we propose a distributed algorithm, based on the Alternating Direction Method of Multipliers (ADMM) [20].

The DistFlow is a well-established method that recursively solves the power flow for strictly radial systems; it was originally proposed in [69–71]. The au-

thors in [24] extended this concept to include branches for both tree networks and mesh networks. This power flow formulation has a distinct advantage in that the bus phase angles are irrelevant for a balanced network (described by its per-phase equivalent) since they are expressed as line power flows and voltage magnitudes. Unfortunately, the power flow and voltage constraints have a nonlinear power loss term that makes the problem non-convex. The authors in [24, 33] provide a lower bound on the losses with a second-order cone program (SOCP). In this case, the solution to the SOCP relaxation is exact when equality on the lower bound is satisfied. Recently, by neglecting the nonlinear terms, the authors of [25, 26] used the DistFlow to formulate a convex quadratic optimal power flow (OPF) to determine the reactive power support provided by inverters in systems with high penetration of PV installations. Our approach in this chapter approximates the nonlinear terms as constants that are periodically updated based on the desired operating point since we found that the loss terms, in general, cannot be entirely neglected. Unlike the SOCP-based OPF, the intended purpose of the fast time-scale control is to maintain the globally optimal solution from the slow time-scale optimization, rather than finding a global minimum for the entire solution space.

The remainder of this chapter is organized as follows. In Section 5.2, we introduce the system model and formulate the voltage regulation problem. In Section 5.3, we rewrite the OPF as a convex QP and extend the per-phase equivalent formulation to the unbalanced three-phase case. The proposed ADMM-based distributed solver is formulated in Section 5.4. Section 5.5 presents the case studies and concluding remarks are presented in Section 5.6.

5.2 Problem Formulation

In this section, we introduce the power flow model used to formulate an OPF, the solution of which handles the voltage regulation problem.

5.2.1 Branch Power Flow Formulation

Consider an $n+1$ bus power distribution system with a tree topology, i.e., a radial network without loops between the branches. We index the feeder by 0, and let the elements in the set $\mathcal{N} := \{1, 2, \ldots, n\}$ index the remaining n buses of the system. The edge-set that represents the set of distribution line segments (which could contain conductors for single-, two-, or three-phase circuits) is denoted by $\mathcal{E} \subseteq \{\mathcal{N} \cup \{0\}\} \times \{\mathcal{N} \cup \{0\}\}$, with $(i,k) \in \mathcal{E}$ if there is a distribution line segment between buses i and k, where bus i is closest to the feeder; i.e., in our notation the edges are directed so that $(i,k) \in \mathcal{E} \Rightarrow (k,i) \notin \mathcal{E}$. The impedance for the distribution line segment (i,k) is given by $z_{ik} = r_{ik} + jx_{ik}$. We ignore line charging (shunt capacitance) since lines in distribution systems are typically so short that this admittance can be neglected [47]. The demand at bus k is denoted by $p_k^d + jq_k^d$.

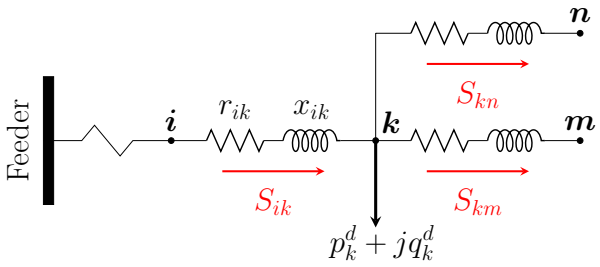

Figure 5.1: Distribution line segment power flows.

Consider the circuit shown in Fig. 5.1; we formulate the voltage drop and power flow equations between buses i and k using the notation and orientation shown in the figure. In [47], the power flow in distribution systems is computed through a series of forward and backward sweeps. In the forward sweep, the distribution line currents are computed from the end of the radial lines up to the feeder with the bus voltages fixed to some initial value. Then, the currents are fixed and the bus voltages are computed in the backward sweep using the correct feeder bus voltage. We mimic this branch flow

approach by computing the power transferred through the distribution line segment (i,k) from the downstream line power flows, and we determine the voltage of k in terms of the upstream bus i.

Let $\mathcal{H}_k := \{j \,|\, (k,j) \in \mathcal{E}\}$ be the set of buses downstream of bus k (e.g., in Fig. 5.1 we have $\mathcal{H}_k = \{m,n\}$); then, the total power $S_{ik} \in \mathbb{C}$ transferred through the distribution line segment (i,k) is

$$S_{ik} = \sum_{j \in \mathcal{H}_k} S_{kj} + s_k^d + z_{ik} \frac{|S_{ik}|^2}{|V_i|^2}, \tag{5.1}$$

where the line power flow S_{ik} is always determined relative to the sending end voltage, $V_i = |V_i| \angle \theta_i$, of the distribution line segment. Similar to the backward sweep, we compute the voltage of bus k based on the upstream bus i by using

$$V_k = V_i - z_{ik} \frac{P_{ik} - jQ_{ik}}{V_i^*}, \tag{5.2}$$

where the feeder's voltage is fixed, i.e., $V_0 = V^s = |V^s| \angle 0$, for some constant $|V^s|$. We can remove the dependence on the phase angles in (5.2) by taking the product of each side of (5.2) with its conjugate. Thus, the branch model of the power flow equations for an $n+1$ bus network are given by

$$V_0 = V^s, \tag{5.3a}$$

$$|V_k|^2 = |V_i|^2 - 2\left(r_{ik}P_{ik} + x_{ik}Q_{ik}\right) + |z_{ik}|^2 \frac{|S_{ik}|^2}{|V_i|^2}, \tag{5.3b}$$

$$P_{ik} = \sum_{j \in \mathcal{H}_k} P_{kj} + p_k^d + r_{ik} \frac{|S_{ik}|^2}{|V_i|^2}, \tag{5.3c}$$

$$Q_{ik} = \sum_{j \in \mathcal{H}_k} Q_{kj} + q_k^d + x_{ik} \frac{|S_{ik}|^2}{|V_i|^2}, \tag{5.3d}$$

for all $(i,k) \in \mathcal{E}$. This is a natural extension of the DistFlow model originally proposed in [69, 70], which formulates the line power transfer (5.3c)–(5.3d) so that the power flow can be solved recursively for a strictly radial system. The updated expressions in (5.3c)–(5.3d) are designed to handle branches in a tree network and are similar to the branch flow approach proposed in [24] to accommodate mesh networks.

5.2.2 Voltage Regulation Problem

In Chapter 3, we performed a slow time-scale optimization to fix transformer tap positions so as to establish a voltage magnitude reference, $V^r \in \mathbb{R}^n$, that meets certain operational specifications for the system, i.e., minimize system losses, flatten the voltage profile, or achieve some power factor correction target. Then, bus voltages can be regulated to V^r during the inter-dispatch time periods by controlling the reactive power contributions of the aggregated DERs connected to the system buses. Ideally, we would like to determine the amount of reactive power support needed to track V^r as the load fluctuates; however, there may exist no feasible solution given the current operating conditions and the lower and upper reactive power limits on the reactive power capable DERs, $\underline{q}, \overline{q}$, respectively. Thus, we perform an optimization to minimize the voltage deviations from V^r.

Let $\mathcal{N} = \mathcal{N}_c \cup \mathcal{N}_u$, $\mathcal{N}_c \cap \mathcal{N}_u = \emptyset$, where $\mathcal{N}_c$ and $\mathcal{N}_u$ are, respectively, the sets of buses that have controllable and uncontrolled reactive power resources. We define q_k to be the total reactive power contributions of the DERs connected to $\mathcal{N}_c$. Then, we can perform the following optimization

$$\min_{\boldsymbol{V}} \sum_{k=1}^{n} w_k \left(|V_k|^2 - (V_k^r)^2 \right)^2 \tag{5.4a}$$

such that, for all $(i,k) \in \mathcal{E}$,

$$V_0 = V^s, \tag{5.4b}$$

$$|V_k|^2 = |V_i|^2 - 2\left(r_{ik}P_{ik} + x_{ik}Q_{ik}\right) + |z_{ik}|^2 \frac{|S_{ik}|^2}{|V_i|^2}, \qquad k \in \mathcal{N}, \tag{5.4c}$$

$$P_{ik} = \sum_{j \in \mathcal{H}_k} P_{kj} + p_k^d + r_{ik}\frac{|S_{ik}|^2}{|V_i|^2}, \qquad k \in \mathcal{N}, \tag{5.4d}$$

$$Q_{ik} = \sum_{j \in \mathcal{H}_k} Q_{kj} + q_k^d + x_{ik}\frac{|S_{ik}|^2}{|V_i|^2} - q_k, \qquad k \in \mathcal{N}_c, \tag{5.4e}$$

$$Q_{ik} = \sum_{j \in \mathcal{H}_k} Q_{kj} + q_k^d + x_{ik}\frac{|S_{ik}|^2}{|V_i|^2}, \qquad k \in \mathcal{N}_u, \tag{5.4f}$$

and

$$\underline{q}_k \leq q_k \leq \overline{q}_k, \qquad k \in \mathcal{N}_c. \tag{5.4g}$$

The weighting term $w_k > 0$ in (5.4a) can be chosen based on heuristics, e.g., larger penalties will be given to buses that are most susceptible to voltage violations. We can incorporate the fixed transformer tap positions by replacing $|V_i|^2$ in (5.4c)–(5.4f) with $|V_i|^2 / a_{ik}^2$, where a_{ik} is the per-unit turns ratio of the voltage regulator connected to the upstream bus i. The benefit of the branch flow approach is that we are able to remove all dependencies on the phase angles; however, the problem is still nontrivial due to the nonlinear terms in the equality constraints. Hence, in the ensuing section we will discuss how to relax the OPF in (5.4).

5.3 Convex Relaxation

In this section, we make the necessary relaxations to reformulate the OPF problem in (5.4) as a convex quadratic program (QP) with linear constraints. Then, we develop the equivalent formulation for the three-phase unbalanced case.

5.3.1 Relaxed OPF for Balanced Systems

The approach to voltage regulation proposed in this chapter implies that we dispatch reactive capable DERs so as to minimize voltage deviations with respect to the reference voltage profile, V^r, that results from the latest dispatch using the method proposed in Chapter 3. If the fast time-scale optimization fails to guarantee some performance specifications, then the slow time-scale resources are redispatched. Consequently, changes in the quadratic power loss terms in (5.4) are negligible for small variations in line currents, and therefore we can replace these terms with the following constant:

$$c_{ik}\left(V^r\right) = \frac{\left|S_{ik}(V^r)\right|^2}{\left|V_i^r\right|^2}, \qquad (i,k) \in \mathcal{E}, \tag{5.5}$$

which is computed after every slow time-scale optimization is solved.

We found experimentally for the systems in Section 5.5 that, for mild loading conditions, the nonlinear loss terms in (5.4), as given in (5.5), generally remained constant, and in some instances, they can be neglected. For example, the nonlinear term in the voltage relationship (5.4c) was found to be

3-4 orders of magnitude smaller than the other terms and could be considered negligible, which is consistent with the results in [25,26]. The nonlinear terms in the power flow constraints (5.4d) were found to be 2-4 orders of magnitude smaller than the line power flows. Despite the relative size of these terms, we found that the optimization results were more accurate compared to a nonlinear OPF when we treated them as constants (as determined by (5.5)), rather than ignoring them. In particular, the reactive power constraint (5.4e)–(5.4f) can be very sensitive to the value of c_{ik} under heavy active power loading and significant reactive power support. For example, $P_{ik} >> Q_{ik}$ implies that $S_{ik} \propto P_{ik}$ becomes large and the reactive power Q_{ik} diminishes since q_k is perceived as a *negative* load.

Now that (5.5) is treated as a constant, the OPF problem in (5.4) simplifies to a QP. The power flow constraints in (5.4d)–(5.4f) do not depend on bus voltages, and the square of the voltage magnitudes in (5.4a)–(5.4c) can be replaced by the variables $U_i = |V_i|^2$ and $U_i^r = (V_i^r)^2$. Thus, the equivalent problem has a quadratic cost function with linear constraints, and can be formulated as follows:

$$\min_{U} \sum_{k=1}^{n} w_k \left(U_k - U_k^r\right)^2 \tag{5.6a}$$

such that, for all $(i,k) \in \mathcal{E}$,

$$U_0 = |V^s|^2, \tag{5.6b}$$

$$U_k = U_i - 2\left(r_{ik}P_{ik} + x_{ik}Q_{ik}\right) + |z_{ik}|^2 c_{ik}\left(V^r\right), \qquad k \in \mathcal{N}, \tag{5.6c}$$

$$P_{ik} = \sum_{j \in \mathcal{H}_k} P_{kj} + p_k^d + r_{ik} c_{ik}\left(V^r\right), \qquad k \in \mathcal{N}, \tag{5.6d}$$

$$Q_{ik} = \sum_{j \in \mathcal{H}_k} Q_{kj} + q_k^d + x_{ik} c_{ik}\left(V^r\right) - q_k, \qquad k \in \mathcal{N}_c, \tag{5.6e}$$

$$Q_{ik} = \sum_{j \in \mathcal{H}_k} Q_{kj} + q_k^d + x_{ik} c_{ik}\left(V^r\right), \qquad k \in \mathcal{N}_u, \tag{5.6f}$$

and

$$\underline{q}_k \le q_k \le \overline{q}_k, \qquad k \in \mathcal{N}_c. \tag{5.6g}$$

Next, we discuss additional approaches to improve the linear approximation of the c_{ik}'s.

5.3.2 Extension to Unbalanced Three-Phase Systems

Up to this point, we have only considered the case when the phases are balanced; however, distribution systems are inherently unbalanced with untransposed distribution line segments, and have single-, two-, and three-phase radial feeds. Therefore, extending the ideas discussed thus far to unbalanced three-phase systems is well motivated [27, 52]. Unfortunately, the coupling between phases for the system voltages in (5.6c) requires additional approximations to simplify the unbalanced case to a QP problem.

For each $(i,k) \in \mathcal{E}$, let

$$\boldsymbol{V}_k = \boldsymbol{V}_i - \boldsymbol{z}_{ik}\left[(\boldsymbol{P}_{ik} - j\boldsymbol{Q}_{ik}) \oslash \boldsymbol{V}_i^*\right], \tag{5.7}$$

where $\boldsymbol{V}_i = [V_{i_a}, V_{i_b}, V_{i_c}]^{\mathrm{T}}$, $\boldsymbol{V}_k = [V_{k_a}, V_{k_b}, V_{k_c}]^{\mathrm{T}}$, $\boldsymbol{P}_{ik} = [P_{ik_a}, P_{ik_b}, P_{ik_c}]^{\mathrm{T}}$, $\boldsymbol{Q}_{ik} = [Q_{ik_a}, Q_{ik_b}, Q_{ik_c}]^{\mathrm{T}}$, and $\boldsymbol{z}_{ik} \in \mathbb{C}^{3\times 3}$, and $\oslash$ and $\odot$ denote the element-wise division and multiplication, respectively. [This is essentially an extension of (5.2) to the three-phase case.]

Unlike the per-phase equivalent case, multiplying by the complex conjugate of both sides of (5.7) will not remove the dependence on $\boldsymbol{\theta}$. This is due to the fact that there is a coupling between the phases at bus i that arises from the cross-products of the three-phase equations for the phase voltages and line currents. To address this, we have observed that the voltage magnitudes between the phases are similar, i.e., $|V_{i_a}| \approx |V_{i_b}| \approx |V_{i_c}|$, and that the phase unbalances on each bus are not very severe, so we assume that the voltages are nearly balanced. This enables us to approximate the phase differences at bus i as

$$\begin{aligned} \cos\left(\theta_{i_a} - \theta_{i_b}\right) &= \cos\left(e^{j2\pi/3} + \alpha\right) \\ &= -\frac{1}{2}\cos\left(\alpha\right) - \frac{\sqrt{3}}{2}\sin\left(\alpha\right) \approx -\frac{1}{2}, \end{aligned} \tag{5.8}$$

and

$$\begin{aligned} \sin\left(\theta_{i_a} - \theta_{i_b}\right) &= \sin\left(e^{j2\pi/3} + \alpha\right) \\ &= \frac{\sqrt{3}}{2}\cos\left(\alpha\right) - \frac{1}{2}\sin\left(\alpha\right) \approx \frac{\sqrt{3}}{2}, \end{aligned} \tag{5.9}$$

where α represents the relative phase unbalance, which is sufficiently small [27]. We can update the voltage magnitude constraint in (5.6c) for the un-

balanced case with

$$|\boldsymbol{V}_k|^2 = |\boldsymbol{V}_i|^2 - 2\left(\tilde{\boldsymbol{r}}_{ik}\boldsymbol{P}_{ik} + \tilde{\boldsymbol{x}}_{ik}\boldsymbol{Q}_{ik}\right) + \boldsymbol{c}^v_{ik}, \tag{5.10}$$

where

$$\boldsymbol{a} = \begin{bmatrix} 1 & e^{-j2\pi/3} & e^{j2\pi/3} \end{bmatrix}^{\mathrm{T}}, \tag{5.11}$$

$$\tilde{\boldsymbol{r}}_{ik} = \mathrm{Re}\left\{\boldsymbol{a}\boldsymbol{a}^{\mathrm{H}}\right\} \odot \boldsymbol{r}_{ik} + \mathrm{Im}\left\{\boldsymbol{a}\boldsymbol{a}^{\mathrm{H}}\right\} \odot \boldsymbol{x}_{ik}, \tag{5.12}$$

$$\tilde{\boldsymbol{x}}_{ik} = \mathrm{Re}\left\{\boldsymbol{a}\boldsymbol{a}^{\mathrm{H}}\right\} \odot \boldsymbol{x}_{ik} - \mathrm{Im}\left\{\boldsymbol{a}\boldsymbol{a}^{\mathrm{H}}\right\} \odot \boldsymbol{r}_{ik}, \tag{5.13}$$

and

$$\boldsymbol{c}^v_{ik}(\boldsymbol{V}^r) = \left[\boldsymbol{z}_{ik}\big(\boldsymbol{S}^*_{ik}(\boldsymbol{V}^r) \oslash \boldsymbol{V}^*_i(\boldsymbol{V}^r)\big)\right] \odot \left[\boldsymbol{z}^*_{ik}\big(\boldsymbol{S}_{ik}(\boldsymbol{V}^r) \oslash \boldsymbol{V}_i(\boldsymbol{V}^r)\big)\right], \tag{5.14}$$

for all $(i,k) \in \mathcal{E}$.

The line flow expressions in (5.6d)–(5.6g) for the balanced case will translate directly to the unbalanced problem formulation since the coupling is captured by the nonlinear distribution line losses, which we treat as some constants, $\boldsymbol{c}^p_{ik}, \boldsymbol{c}^q_{ik}$, for the active and reactive line power flows, respectively. Specifically, for the unbalanced case, we update the power loss constant of the distribution line segment $(i,k) \in \mathcal{E}$ with

$$\boldsymbol{c}^s_{ik}(\boldsymbol{V}^r) = \left[\boldsymbol{S}_{ik}\left(\boldsymbol{V}^r\right) \oslash \boldsymbol{V}_i(\boldsymbol{V}^r)\right] \odot \left(\boldsymbol{V}_i(\boldsymbol{V}^r) - \boldsymbol{V}_k(\boldsymbol{V}^r)\right), \tag{5.15}$$

and separate the real and imaginary components as

$$\boldsymbol{c}^p_{ik}(\boldsymbol{V}^r) = \mathrm{Re}\left\{\boldsymbol{c}^s_{ik}(\boldsymbol{V}^r)\right\}, \text{ and } \boldsymbol{c}^q_{ik}(\boldsymbol{V}^r) = \mathrm{Im}\left\{\boldsymbol{c}^s_{ik}(\boldsymbol{V}^r)\right\}. \tag{5.16}$$

We express the unbalanced three-phase voltage regulation QP-based OPF as

$$\min_{\boldsymbol{U}} \sum_{k=1}^{n} \left\|\boldsymbol{w}_k \odot \left(\boldsymbol{U}_k - \boldsymbol{U}^r_k\right)\right\|_2^2 \tag{5.17a}$$

such that, for all $(i,k) \in \mathcal{E}$,

$$\boldsymbol{U}_0 = |\boldsymbol{V}^s| \odot |\boldsymbol{V}^s|, \tag{5.17b}$$

$$\boldsymbol{U}_k = \boldsymbol{U}_i - 2\left(\tilde{\boldsymbol{r}}_{ik}\boldsymbol{P}_{ik} + \tilde{\boldsymbol{x}}_{ik}\boldsymbol{Q}_{ik}\right) + \boldsymbol{c}^v_{ik}(\boldsymbol{V}^r), \qquad k \in \mathcal{N}, \tag{5.17c}$$

$$\boldsymbol{P}_{ik} = \sum_{j \in \mathcal{H}_k} \boldsymbol{P}_{kj} + \boldsymbol{p}^d_k + \boldsymbol{c}^p_{ik}(\boldsymbol{V}^r), \qquad k \in \mathcal{N}, \tag{5.17d}$$

$$\boldsymbol{Q}_{ik} = \sum_{j \in \mathcal{H}_k} \boldsymbol{Q}_{kj} + \boldsymbol{q}^d_k + \boldsymbol{c}^q_{ik}(\boldsymbol{V}^r) - \boldsymbol{q}_k, \qquad k \in \mathcal{N}_c, \tag{5.17e}$$

$$\boldsymbol{Q}_{ik} = \sum_{j \in \mathcal{H}_k} \boldsymbol{Q}_{kj} + \boldsymbol{q}^d_k + \boldsymbol{c}^q_{ik}(\boldsymbol{V}^r), \qquad k \in \mathcal{N}_u, \tag{5.17f}$$

and

$$\underline{\boldsymbol{q}}_k \leq \boldsymbol{q}_k \leq \overline{\boldsymbol{q}}_k, \qquad k \in \mathcal{N}_c. \tag{5.17g}$$

Note that this will reduce to (5.6) for a balanced system.

5.3.3 Accuracy of the Linearized System

We found that the constant in (5.5) based on the initial optimal dispatch was accurate for modest variations in active power; however, it does not properly reflect the operating conditions as the system deviates significantly away from the initial operating point. In this case, we can maintain the linear constraints in the QP-based OPF in (5.6) and improve its accuracy by doing the following:

(i) we can recompute the c_{ik}'s in (5.5) based on the current distribution line segment power flows P_{ik_o}, Q_{ik_o} and the regulation voltage U_i^r, or

(ii) estimate a linear approximation of the nonlinear terms in (5.4) based on the current distribution line segment power flows $P_{ik} + jQ_{ik}$ and the set-point voltage V^r.

The nonlinearity in (5.4c)–(5.4f) for the distribution line segment $(i,k) \in \mathcal{E}$ attached to bus i is given by

$$h_i\left(P_{ik}, Q_{ik}, U_i\right) = \frac{P_{ik}^2 + Q_{ik}^2}{U_i}, \tag{5.18}$$

where (5.5) is equivalent to $c_{ik}(V^r) = h_i\left(P_{ik}(V^r), Q_{ik}(V^r), (V_i^r)^2\right)$. We define the approximated nonlinear terms as

$$c_{ik}^v(P_{ik}, Q_{ik}) = |z_{ik}|^2 h_i\left(P_{ik}, Q_{ik}, U_i^r\right), \tag{5.19a}$$

$$c_{ik}^p(P_{ik}, Q_{ik}) = r_{ik} h_i\left(P_{ik}, Q_{ik}, U_i^r\right), \tag{5.19b}$$

$$c_{ik}^q(P_{ik}, Q_{ik}) = x_{ik} h_i\left(P_{ik}, Q_{ik}, U_i^r\right), \tag{5.19c}$$

for the voltage, active power, and reactive power equality constraints, respectively. We can linearize (5.18) around the operating point (P_o, Q_o, U^r) with

$$h_i(P_{ik}, Q_{ik}, U_i^r) \approx \frac{1}{U_i^r}\left[2P_{ik_o}P_{ik} + 2Q_{ik_o}Q_{ik} - P_{ik_o}^2 - Q_{ik_o}^2\right]. \tag{5.20}$$

The active power behaves as a disturbance to the network and we compensate by controlling the reactive power injections to regulate to U^r. Consequently, the branch power flow constraints in the optimization depend on the line power flows and not the bus voltages since we regulate the system to the desired set-point; therefore, (5.20) does not have a dependence on U. We refer the reader to Appendix D for the unbalanced three-phase linear fit of the nonlinear terms $\boldsymbol{c}_{ik}^v$, $\boldsymbol{c}_{ik}^p$, and $\boldsymbol{c}_{ik}^q$.

Consider the curves shown in Fig. 5.2. In each of the subfigures, we show the behavior of the nonlinear terms and their approximated values as the active powers are varied from their rated values. Figures 5.2(a) and 5.2(b) confirm the intuition discussed in Section 5.3.1 that the magnitudes of c_{ik}^v and c_{ik}^p are small and remain relatively constant compared to the bus voltages and active power constraints, respectively. As shown in Fig. 5.2(c), accuracy of the solution to the OPF in (5.6) depends largely on the reactive power constraint. For large deviations away from the rated load, the constant approximation $c_{ik}^q(V^r)$ is not accurate; however, we can improve this approximation with the approach in (i) above by recomputing $c_{ik}^q(P, Q) = x_{ik} h_i(P, Q, U^r)$ every time we run the fast time-scale optimization. Furthermore, we can improve the accuracy for large changes in active power by replacing the constants c_{ik}^v, c_{ik}^p, and c_{ik}^q with the linear equations in (5.19) as suggested by (ii), where the coefficients can be updated with the current distribution line power flows and reference voltage. We provide a simple case study to demonstrate the various approximations of the nonlinear terms in Section 5.5.2.

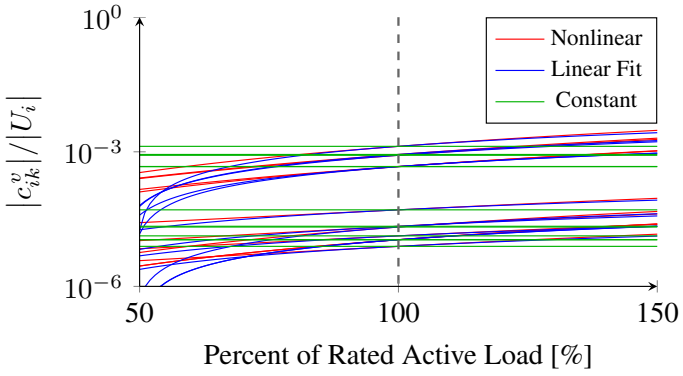

(a) Voltage nonlinear term.

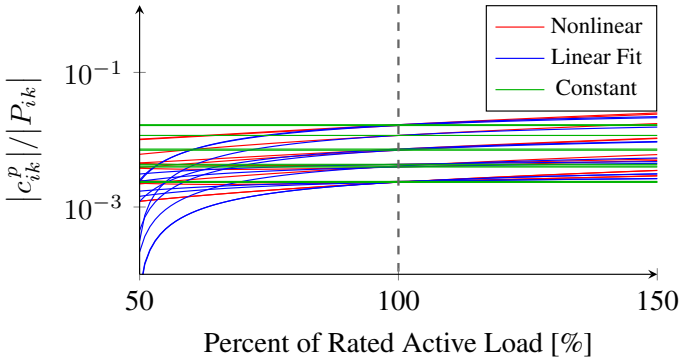

(b) Active power nonlinear term.

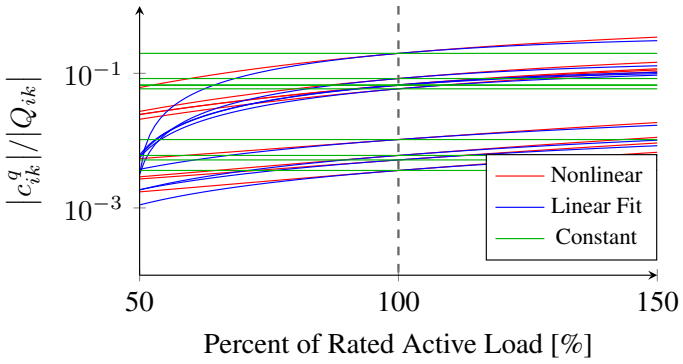

(c) Reactive power nonlinear term.

Figure 5.2: A comparison of the nonlinear terms with respect to the active power loads.

5.4 Distributed Algorithm

As we mentioned earlier, there are several advantages that motivate the use of a distributed algorithm to solve the QP-based OPF in Section 5.3; in this section, we propose the use of ADMM to develop such an algorithm. ADMM has been proven to be a powerful solution to develop distributed

algorithms [20]; in particular, with ADMM, the complexity of the OPF problem scales with the sub-area size rather than with the full network size, and the communication architecture is simpler than that of a centralized scheme. ADMM iteratively minimizes the augmented Lagrangian over three types of variables: (i) the *primary* variables, i.e., the bus voltages and line power flows; (ii) the *auxiliary* variables that are used to enforce boundary conditions among neighboring areas; and (iii) the *multipliers* for dualizing the relaxed problem. The Lagrangian is designed to be separable relative to each type of variable so that we can cyclically minimize with respect to one variable type while fixing the others. This allows us to solve the problem distributedly and asymptotically converge to the same minimum costs obtained with a centralized solver [20].

For each node, let $\mathcal{B}^{(k)}$ denote the set that captures the voltage and local power flow constraints described in (5.6b)–(5.6g). We define the auxiliary variables $\overline{U}_i$, $\overline{P}_{ik}$, $\overline{Q}_{ik}$ for the boundary conditions on the upstream bus voltages and line power flows, respectively. The global minimization problem can be formulated as follows:

$$\min_{U} \sum_{k=1}^{n} w_k \left(U_k - U_k^r\right)^2 \tag{5.21a}$$

such that

$$\left\{U^{(k)},\, P^{(k)}, Q^{(k)}\right\} \in \mathcal{B}^{(k)}, \qquad k \in \mathcal{N}, \tag{5.21b}$$

and

$$U_i^{(k)} - \overline{U}_i = 0, \qquad (i,k) \in \mathcal{E},\, i \neq 0, \tag{5.21c}$$
$$U_i^{(i)} - \overline{U}_i = 0, \qquad (i,k) \in \mathcal{E},\, i \neq 0, \tag{5.21d}$$
$$P_{ik}^{(k)} - \overline{P}_{ik} = 0, \qquad (i,k) \in \mathcal{E},\, i \neq 0, \tag{5.21e}$$
$$P_{ik}^{(i)} - \overline{P}_{ik} = 0, \qquad (i,k) \in \mathcal{E},\, i \neq 0, \tag{5.21f}$$
$$Q_{ik}^{(k)} - \overline{Q}_{ik} = 0, \qquad (i,k) \in \mathcal{E},\, i \neq 0, \tag{5.21g}$$
$$Q_{ik}^{(i)} - \overline{Q}_{ik} = 0, \qquad (i,k) \in \mathcal{E},\, i \neq 0. \tag{5.21h}$$

Note that we follow the per-phase formulation in (5.21) corresponding to a balanced system.

Let $\lambda^u_{ik}, \lambda^p_{ik}, \lambda^q_{ik} \in \mathbb{R}$ denote the Lagrangian multipliers associated with the equality constraints (5.21c)–(5.21d), (5.21e)–(5.21f), and (5.21g)–(5.21h), respectively. Then, the augmented Lagrangian is of the form

$$\mathcal{L}_c(\cdot) = \sum_{k \in \mathcal{N}} \mathcal{L}_c^{(k)}(\cdot), \tag{5.22}$$

where $c > 0$ is the penalty coefficient, with the $\mathcal{L}_c^{(k)}(\cdot)$'s defined as

$$\begin{aligned}
\mathcal{L}_c^{(k,0)} &\left(U^{(k)}, P^{(k)}, Q^{(k)}, \overline{U}, \overline{P}, \overline{Q}, \lambda^u, \lambda^p, \lambda^q\right) = \\
&w_k \left(U_k^{(k)} - U_k^r\right)^2 + \sum_{j \in \mathcal{H}_k} \Bigg[\lambda^u_{kj} \left(\overline{U}_k - U_k^{(k)}\right) \\
&\qquad + \lambda^p_{kj} \left(\overline{P}_{kj} - P_{kj}^{(k)}\right) + \lambda^q_{kj} \left(\overline{Q}_{kj} - Q_{kj}^{(k)}\right) \Bigg] \\
&+ \frac{c}{2} \sum_{j \in \mathcal{H}_k} \left[\left(\overline{U}_k - U_j^{(k)}\right)^2 + \left(\overline{P}_{kj} - P_{kj}^{(k)}\right)^2 + \left(\overline{Q}_{kj} - Q_{kj}^{(k)}\right)^2 \right],
\end{aligned} \tag{5.23}$$

and

$$\begin{aligned}
\mathcal{L}_c^{(k)} &\left(U^{(k)}, P^{(k)}, Q^{(k)}, \overline{U}, \overline{P}, \overline{Q}, \lambda^u, \lambda^p, \lambda^q\right) = \\
&\mathcal{L}_c^{(k,0)} \left(U^{(k)}, P^{(k)}, Q^{(k)}, \overline{U}, \overline{P}, \overline{Q}, \lambda^u, \lambda^p, \lambda^q\right) \\
&+ \lambda^u_{ik} \left(U_i^{(k)} - \overline{U}_i\right) + \lambda^p_{ik} \left(P_{ik}^{(k)} - \overline{P}_{ik}\right) + \lambda^q_{ik} \left(Q_{ik}^{(k)} - \overline{Q}_{ik}\right) \\
&+ \frac{c}{2} \left[\left(U_i^{(k)} - \overline{U}_i\right)^2 + \left(P_{ik}^{(k)} - \overline{P}_{ik}\right)^2 + \left(Q_{ik}^{(k)} - \overline{Q}_{ik}\right)^2 \right].
\end{aligned} \tag{5.24}$$

The augmented Lagrangian given in (5.23) is specific for the bus directly downstream of the feeder, i.e., bus k such that $(0, k) \in \mathcal{E}$. In this particular case, there are no upstream boundary conditions on bus voltage or line power flows since the feeder voltage is fixed; consequently, a local optimization will not be performed at the feeder. The Lagrangian for the remaining buses, as given in (5.24), contains additional terms for the upstream voltage and line flows of $k \in \mathcal{N}$. Then, we can cyclically optimize the augmented Lagrangian $\mathcal{L}_c^{(k)}(\cdot)$ with respect to one of the groups of variables, while holding the others constant with the following three-step update rule for the r^{th} iteration:

[S1.] *Local Optimization:* We take the infimum of $\mathcal{L}_c(\cdot)$ with respect to the primal variables, and update them as

$$U^{(k)}[r] = \underset{\left\{U^{(k)},P^{(k)},Q^{(k)}\right\}\in\mathcal{B}^{(k)}}{\arg\min} \mathcal{L}_c^{(k)}(\cdot), \tag{5.25}$$

which is dependent on the Lagrangian multipliers and auxiliary variables from the previous iteration $r-1$.

[S2.] *Auxiliary Variable Update:* We determine the update rules for the auxiliary variables by solving

$$\nabla_{\overline{U}_i}\mathcal{L}_c(\cdot) = \nabla_{\overline{P}_{ik}}\mathcal{L}_c(\cdot) = \nabla_{\overline{Q}_{ik}}\mathcal{L}_c(\cdot) = 0. \tag{5.26}$$

The update rules for the auxiliary variables will be

$$\overline{U}_i[r] = \frac{1}{2}\left(U_i^{(k)} + U_i^{(i)}\right), \tag{5.27}$$

$$\overline{P}_{ik}[r] = \frac{1}{2}\left(P_{ik}^{(k)} + P_{ik}^{(i)}\right), \tag{5.28}$$

$$\overline{Q}_{ik}[r] = \frac{1}{2}\left(Q_{ik}^{(k)} + Q_{ik}^{(i)}\right), \tag{5.29}$$

for all $(i,k) \in \{\mathcal{E}\backslash(0,j)\}$.

[S3.] *Multipliers Update:* We determine the update rules for the Lagrangian multipliers by taking the gradient of $\mathcal{L}_c^{(k)}(\cdot)$ and utilizing a dual ascent. The update rules for multipliers will be

$$\lambda_{ik}^{u}[r] = \lambda_{ik}^{u}[r\text{-}1] + \frac{c}{2}\left(U_i^{(k)}[r] - U_i^{(i)}[r]\right)^{\mathrm{T}}, \tag{5.30a}$$

$$\lambda_{ik}^{p}[r] = \lambda_{ik}^{p}[r\text{-}1] + \frac{c}{2}\left(P_{ik}^{(k)}[r] - P_{ik}^{(i)}[r]\right)^{\mathrm{T}}, \tag{5.30b}$$

$$\lambda_{ik}^{q}[r] = \lambda_{ik}^{q}[r\text{-}1] + \frac{c}{2}\left(Q_{ik}^{(k)}[r] - Q_{ik}^{(i)}[r]\right)^{\mathrm{T}}. \tag{5.30c}$$

Note that in Step S3, we use a single dual variable for each boundary condition on a distribution line segment rather than two (one for each subproblem) and account for this through a sign difference between upstream and downstream buses.

5.5 Case Studies

We begin this section by illustrating the ability of the QP-based OPF to optimally track the system voltage in a 15-bus unbalanced three-phase test system, and compare the results to those obtained with the SDP formulation in Chapter 3. Then, we show the results for the ADMM-based algorithm proposed in Section 5.4. We performed the simulations in MATLAB using the CVX package [60], which was employed to solve the centralized problem and to update the primal variables $\boldsymbol{U}, \boldsymbol{P}, \boldsymbol{Q}$ in Step S1 of the distributed algorithm.

First, we will perform the slow time-scale optimization described in Chapter 3 to set the transformer tap positions and initialize the regulation voltage $\boldsymbol{U}^r$ based on the rated loads. We set the reference voltage in the slow time-scale to $\boldsymbol{V}_k^r = \mathbf{1}$ for all k, and the weighting term, w_k, to a positive value that is a function of the bus distance from the feeder. This effectively flattens the voltage profile and will penalize the deviation from 1 p.u. for the buses furthest from the feeder the most.

The SDP-based OPF for the voltage regulation will have the form

$$\min_{W \succeq \mathbf{0}} \; f_0\left(\boldsymbol{W}\right) + \sum_{k \in \mathcal{N}} w_k \left\| \boldsymbol{U}_k^r - \operatorname{diag}(\boldsymbol{W}_{kk}) \right\|^2 \tag{5.31a}$$

such that

$$\operatorname{Tr}\left(\tilde{\boldsymbol{H}}_k \boldsymbol{W}\right) - \boldsymbol{S}_k - j\boldsymbol{q}_k = \mathbf{0}, \qquad \forall k \in \mathcal{N}_c, \tag{5.31b}$$

$$\operatorname{Tr}\left(\tilde{\boldsymbol{H}}_k \boldsymbol{W}\right) - \boldsymbol{S}_k = \mathbf{0}, \qquad \forall k \in \mathcal{N}_u, \tag{5.31c}$$

and

$$\underline{\boldsymbol{q}}_k \leq \boldsymbol{q}_k \leq \overline{\boldsymbol{q}}_k, \qquad \forall k \in \mathcal{N}_c, \tag{5.31d}$$

where $w_k = 10^4$ for all k and $\boldsymbol{W}_{kk} \in \mathbb{C}^{3\times 3}$ is the submatrix associated with bus k. It is necessary for w_k to be large in (5.31) to ensure that the solution to the OPF is tracking $\boldsymbol{U}^r$ since the line losses $f_0(\boldsymbol{W})$ are approximately four orders of magnitude larger than the voltage penalty term. Note that we use different limits for the reactive power in (5.31d) for regulation problem from the initialization procedure. We limit the amount of reactive power available during the initialization procedure to provide what is equivalent to

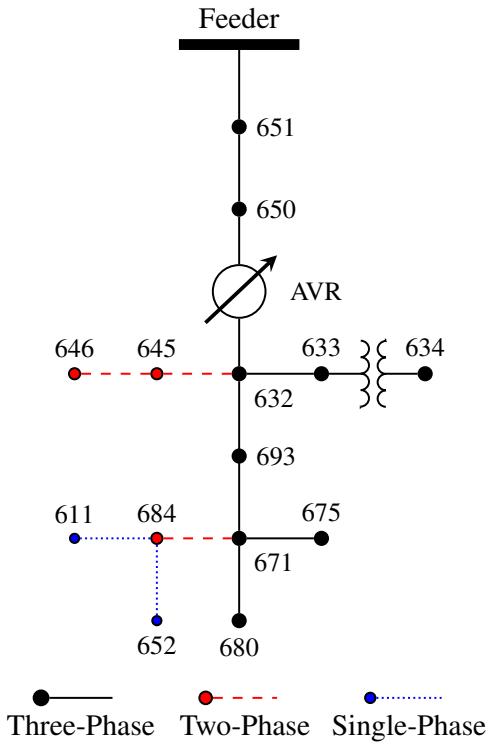

Figure 5.3: 15-bus unbalanced distribution system.

a spinning reserve in transmission systems, i.e., we do not want the DERs operating at full capacity with the initial dispatch so there is headroom to regulate up if necessary.

5.5.1 15-Bus Unbalanced Three-Phase Results

We begin with the 15-bus network shown in Fig. 5.3, which we derived from the IEEE 13-bus—an unbalanced three-phase distribution system, (see, e.g., [47, 58]). The system has a three-phase voltage regulation transformer between buses 650 and 632. The rest of the system contains single-, two-, and three-phase sublaterals. Buses 650 and 651 were added between the feeder and the transformer so that the transformer was not directly connected to the feeder. Bus 693 was added to account for the distributed load along line $(632, 671)$, and bus 692 was removed since it corresponds to a closed switch connected between buses 671 and 675. In all of the simulations, the feeder is balanced with a voltage magnitude of 1.03 p.u.

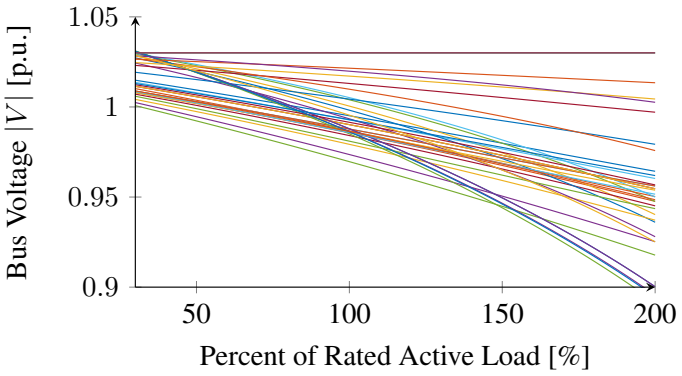

Figure 5.4: Uncontrolled bus voltage magnitudes.

The loads will naturally vary over time, but we are particularly interested in variations of active power injection (positive or negative) due to renewable-based generation and uncontrolled load from storage-capable devices (e.g., PHEV). In the simulations, we hold the reactive power constant and vary the active power from 30% to 200% of the rated load. The uncontrolled voltage response to the load curve is shown in Fig. 5.4. The lowest voltage is 0.97 p.u. at the rated load. At 200% loading, the system voltages drop to as low as 0.892 p.u.

We compared three different optimization schemes: (i) the SDP-based OPF, (ii) the QP-based OPF, and (iii) the QP-based OPF with the constants in (5.14) and (5.16) recalculated based on the current operating conditions.[1] The results for the SDP-based OPF are shown in Fig. 5.5. We ran the OPF in (5.31) to determine the optimal reactive power support shown in Fig. 5.5(b) and the resulting voltage waveform in Fig. 5.5(a). In this case, the voltages are maintained within the original bounds of 0.97 and 1.03 p.u.

Figure 5.6 contains the results for the QP-based OPF described in Section 5.3 with the constants c_{ik} (as defined in (5.5)) computed with the solution of the initial optimal dispatch, which sets the voltages that we need to regulate to. In this case, the relaxed problem improves the bus voltage significantly compared to the uncontrolled case. The results from 30% to 150% of the rated active power are very similar with all of the bus voltages within [0.97, 1.03] p.u. Under significant loading, the voltages drop to as

[1]Note that we do not include the results for the linear fit suggested in Section 5.3.3. For this particular case, the sampled QP-based OPF is equivalent since we gradually change the load. In Section 5.5.2, we provide an example to illustrate the advantages of the QP-based approach with a constant, sampled constant, and linear fit.

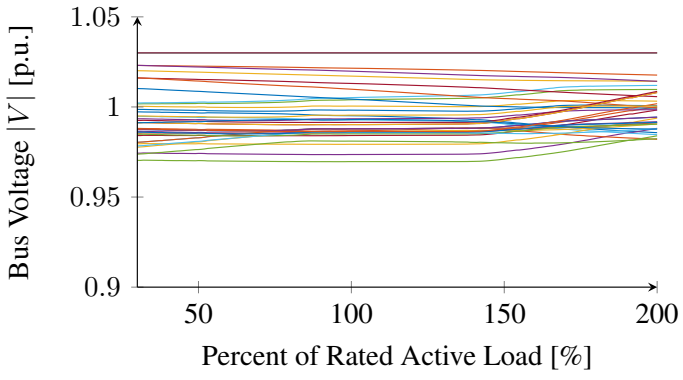

(a) Voltage magnitudes.

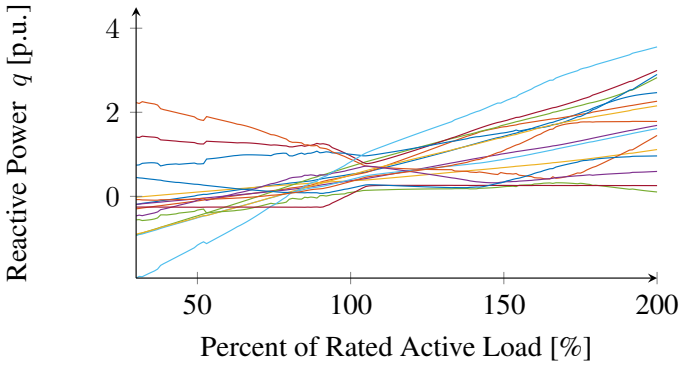

(b) Reactive power.

Figure 5.5: SDP-based optimal control of bus voltage magnitudes with reactive power support.

low as 0.953 p.u., which is still within the desired operating specifications of 1±0.05 p.u.

Lastly, in Fig. 5.7, we show the results for the QP-based OPF with the constants in (5.14) and (5.16) calculated based on the sampled operating conditions when the optimization is performed. The results are comparable to those of the SDP-based OPF with all voltages contained within [0.968, 1.03] p.u. We found that resampling the line current constant c_{ik} actually improved the results of the QP-based OPF since $P_{ik} >> Q_{ik}$ with significant reactive power support.

While the SDP-based approach has an advantage over the QP-based approach in a wider range of operating points, we have shown that the QP-based OPF will produce similar results with less of a computational burden. In the 15-bus system, there are 38 unique phases to track (not every bus has all three phases), so the SDP-based OPF will have approximately 5200 optimization

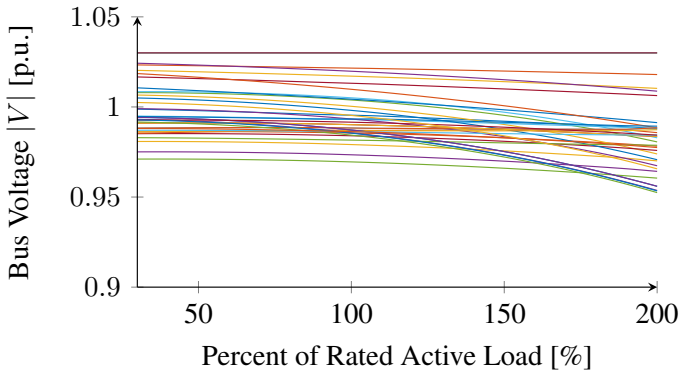

(a) Voltage magnitudes.

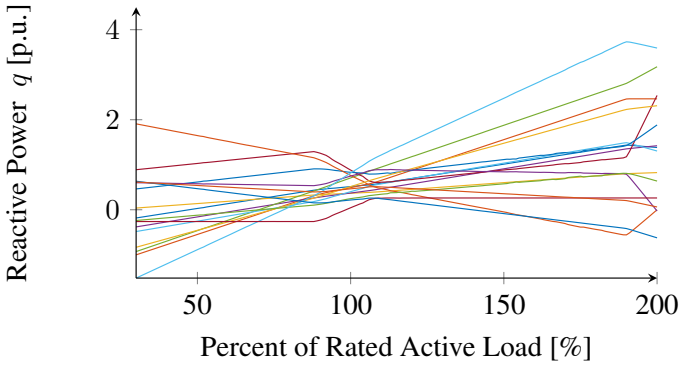

(b) Reactive power.

Figure 5.6: QP-based optimal control of bus voltages with reactive power support.

variables with a positive semidefinite constraint on $\boldsymbol{W}$. Also, the number of variables will grow exponentially with respect to the number of buses. The method proposed in this chapter will have approximately 150 optimization variables and grows linearly. Figure 5.8 compares the cost function for each approach given by

$$\left\|\boldsymbol{V}^2 - \boldsymbol{U}^r\right\|_2^2. \tag{5.32}$$

We see that the results obtained with the SDP-based approach are better than those obtained with the QP-based one with the original constants and comparable to those obtained with the QP-based OPF with the resampled constants.

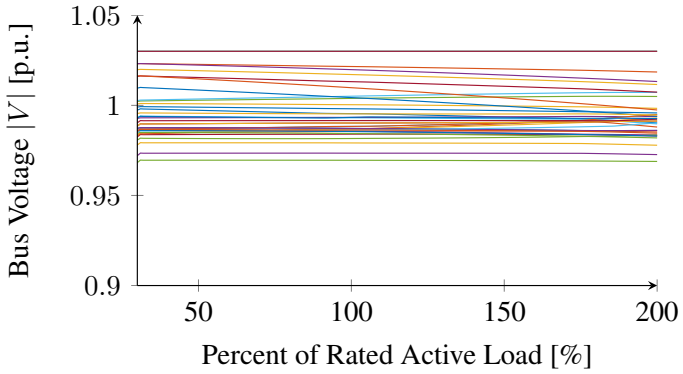

(a) Voltage magnitudes.

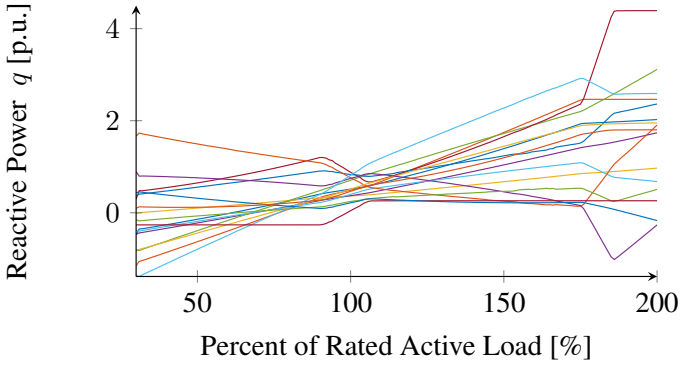

(b) Reactive power.

Figure 5.7: Sampled QP-based optimal control of bus voltages with reactive power support.

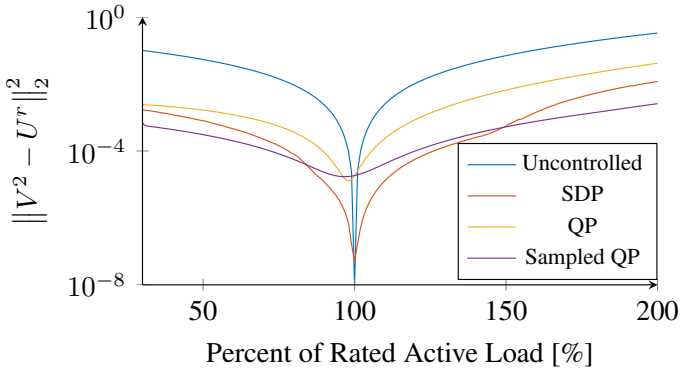

Figure 5.8: Relative costs for each control method.

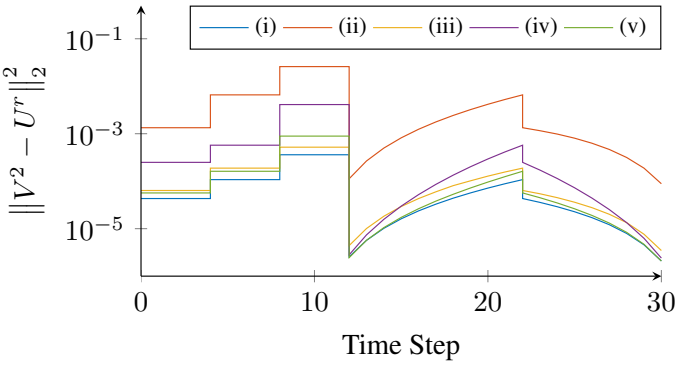

Figure 5.9: Voltage deviations based on the method used to approximate the nonlinear terms.

5.5.2 Nonlinear Term Approximations

Throughout most of this chapter, we linearize the power flow constraints by treating the nonlinear terms as constants. Then, in Section 5.3.3, we discuss how we can improve the accuracy of the linear model by resampling the constants based on the current operation condition or use a linear curve to approximate the nonlinear terms (rather than treat them as constants). In this section, we compare the accuracy of the linear approximation using these techniques. Figure 5.9 shows the ability of the fast time-scale optimizations to regulate bus voltages with an arbitrary active power load profile. The curves represent the following:

(i) This curve shows the results using the SDP-based OPF described in (5.31). This approach represents the base case to compare against since it considers the nonlinear system.

(ii) The results for the OPF described (5.6), where we the compute the constants c_{ik}^v, c_{ik}^p, and c_{ik}^q based on the operating point (P_o, Q_o, V^r) from the initial dispatch by the slow time-scale control.

(iii) In this case, we recompute constants based on the current point and the regulation voltage V^r. Ideally, we should be able to regulate to V^r, but the systems losses will change since the distribution line segment power flows are directly proportional to the system loads.

(iv) This curve represents the first-order approximation of the system losses that we described in (5.19), where $c_{ik}^v(P_{ik}, Q_{ik})$, $c_{ik}^p(P_{ik}, Q_{ik})$, and $c_{ik}^q(P_{ik}, Q_{ik})$ are a function of the line flows and initialized based on the slow time-scale dispatch (P_o, Q_o, V^r).

(v) In this optimization, we combine the concepts in (iii)–(iv) and we reinitialize the coefficients of the linear approximation based on the current operating conditions (P, Q, V^r) rather than the initial point (P_o, Q_o, V^r).

The nonlinear SDP-based OPF in (i) provides a lower bound with the constants in (ii) as an upper bound for the accuracy of the optimizations. The first-order approximation in (iv) does improve the solution compared to estimating c_{ik}^v, c_{ik}^p, and c_{ik}^q as constants (ii); however, updating the system model based on the current operating conditions improves the accuracy of the linear system models in (iii) and (v) dramatically.

5.5.3 ADMM-Based Distributed Solution

Next, we perform a single optimization with the distributed algorithm described in Section 5.4 on the 15-bus three-phase distribution system and compare it against the optimizations in Section 5.5.1. For this particular system, we set the weighting term to be $w_k = 100$ for all k, instead of $w_k = 1$ as in the centralized cases. This was necessary so that the voltage deviations in the cost function would have the same order of magnitude as the power flow penalties in the local augmented Lagrangian. Our stopping criterion is

$$\|\boldsymbol{U}[r] - \boldsymbol{U}[r-1]\|_\infty < \varepsilon, \tag{5.33}$$

where we continue to run the distributed algorithm until the last bus voltage converges to within the tolerance ε [p.u.]. We found that $\varepsilon = 1\text{e}{-5}$ p.u. was an appropriate choice in terms of speed and accuracy. Furthermore, we updated the constants relative to the current operating conditions, since these are known quantities sampled at the current operating point. Figure 5.10 and Table 5.1 show the convergence results for several values of c. The system converged the fastest for $c = 55$; however, increasing the penalty parameter to $c = 60$ caused the algorithm to diverge.

For this simulation, we initialize the reference voltage with the rated loads. Then, we created an under-voltage situation by increasing the system loads to 130% of their rated values, which drops the lowest bus voltage from 0.970 to 0.938 p.u. Figure 5.11 shows the evolution of the distributed optimization for $c = 55$ with the local augmented Lagrangians in Fig. 5.11(a), the bus

Table 5.1: Convergence of the Distributed Algorithm

OPF	c	Iterations	$\left\|\boldsymbol{V}^2\text{-}\boldsymbol{U}^r\right\|_2^2$
SDP		-	1.4e-4
QP		-	2.0e-3
Sampled QP		-	3.2e-4
Distributed QP	15	2281	3.0e-3
	30	1650	1.7e-3
	45	1383	1.0e-3
	55	1278	7.6e-4
	60	-	-

voltages in Fig. 5.11(b), and the reactive power support shown in Fig.5.11(c). The cost function for the distributed algorithm returned results that were on the same order of magnitude as those obtained with the centralized solvers in Section 5.3. We already demonstrated that the SDP approach scales exponentially with the system size and the QP-based OPF will scale linearly; however, the key advantage of the distributed solver is that the complexity of the local problem will remain constant (approximately 10 to 50 optimization variables), regardless of system size.

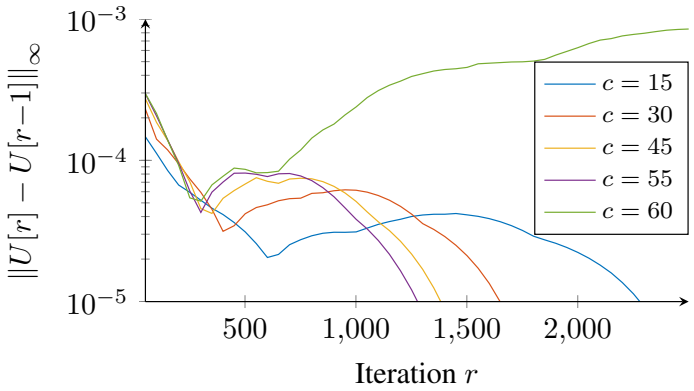

Figure 5.10: Impacts of the choice of the penalty parameter c.

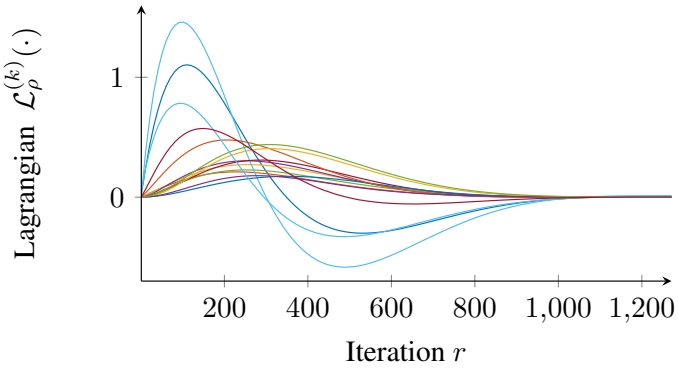

(a) Local Lagrangians at each bus.

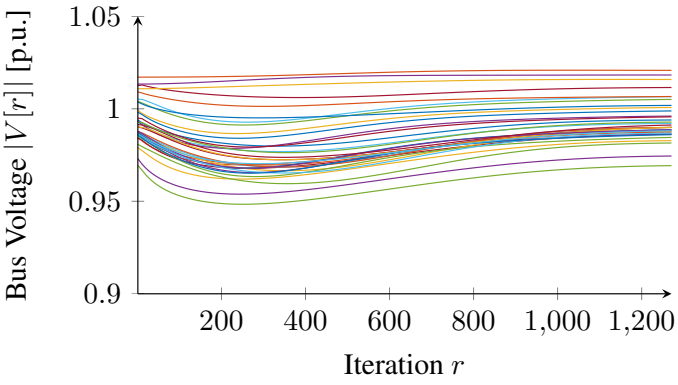

(b) Voltage magnitudes.

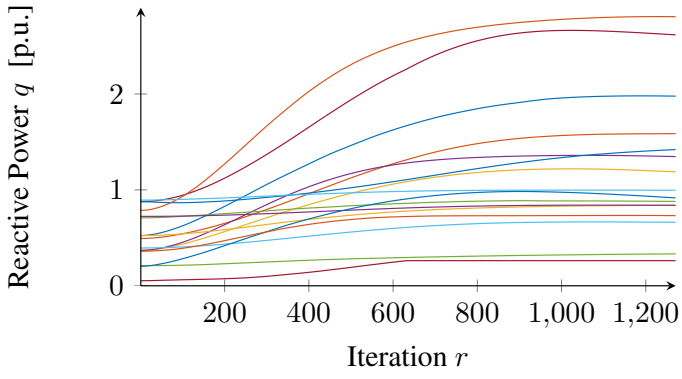

(c) Reactive power support.

Figure 5.11: Convergence of the distributed optimization.

5.6 Summary

In this chapter, we developed a method to optimally regulate bus voltages for unbalanced distribution systems via a convex quadratic optimization program. We showed the potential of the proposed method and ADMM-based algorithm with a 15-bus unbalanced three-phase distribution system.

In the next chapter, we will showcase the system-wide control architecture that arises from combining the ideas put forward in this chapter and those proposed in Chapter 3.

CHAPTER 6

IMPLEMENTATION AND SIMULATION OF THE TWO TIME-SCALE CONTROL

In this chapter, we simulate the two time-scale control architecture described in Chapter 2. We begin with discussion on how to integrate the optimization schemes for the slow and fast time-scales described in Chapters 3 and 5, respectively. Then, we develop the system load models, where we include the active power injections by PV installations and the charging schedules for the electric vehicles (EVs). Finally, we showcase the operation of the two time-scale control architecture in an unbalanced three-phase 123-bus distribution system.

6.1 Introduction

In this thesis, we develop separate optimization-based control methods to dispatch devices that operate at different time scales in unbalanced three-phase distribution networks. We implement the two time-scale control architecture described in Chapter 2, using the results for the slow and fast time-scale optimizations presented in Chapters 3 and 5, respectively. The slow time-scale control will be used to determine TCUL transformer tap settings and set a reference voltage for the fast time-scale control to regulate to. This interaction between the slow time-scale optimization and the fast time-scale regulation creates a challenging problem on how to integrate the two control methods without their solutions being detrimental to one another. For example, how do we balance performance specifications that benefit both the utilities and the customers? What is an appropriate control law during the fast time-scale regulation to signal a redispatch of the TCUL transformer tap positions and reference voltages?

In this chapter, we provide several examples on how to combine the control actions of the two time-scales. While there are a number of policy-based

concerns to address, it is important to examine and understand the operating conditions of the systems that our control architecture will be applied to. In this chapter, we assume that the customers connected to the distribution network in this chapter are exclusively residential. In this regard, a typical American household consumed, on average, 953 kWh and 903 kWh per month in 2010 and 2012, respectively [72]. We can approximate that the average daily energy usage is 30 kWh, which we will use to compare the sizing of the distributed energy resources (DERs) that we include in our model, e.g., residential photovoltaic (PV) installations, electric vehicles (EVs), and plug-in hybrid electric vehicles (PHEVs).

First, we consider the sizing and penetration of residential PV installations. In 2010, the average size residential rooftop PV installation in the US was 5.7 kW [73]. This implies that given ideal solar radiance conditions, it is possible for a customer to inject nearly double their typical energy usage back into the electric grid. For a high penetration of PV installations, a reversal of the flow of active power can occur at the feeder, so we consider a situation where 20% to 30% of the network's customers have PV installed. In certain regions of the country, this level of PV installations is expected; e.g., 12% of the 51,000 customers of Hawaiian Electric have rooftop PV installed as of December 2014. In August 2014, Hawaiian Electric submitted plans to achieve 65% renewable resources by 2030, which exceeds the state minimum requirement of 40%, and intends to triple the amount of distributed rooftop PV systems [74].

We also consider a situation where there is a large number of EVs attached to the network. Table 6.1 shows the battery capacities and onboard charging

Table 6.1: 123-Bus Load Data

Vehicle	Type	Battery Size [kWh]	Charger Size [kW]
Tesla Model S	EV	85	9.6, 19.2
Tesla Roadster	EV	53	16.8
BMW i3	EV	22	7.6
Nissan Leaf	EV	24	6.6
Toyota Prius	PHEV	4.4	3.8
Ford Fusion	PHEV	7.6	3.3
Chevrolet Volt	PHEV	17.1	7.2

Table 6.2: Electric Vehicle Charging Configurations

Configuration	Voltage [V]	Power [kW]
AC Level 1	120	1.92
AC Level 2	240	19.2
DC Level 1	200-500 DC	40
DC Level 2	200-500 DC	100

capabilities of commercially available EVs and PHEVs [75–80]. In Table 6.2, we list the J1772 standards for charging solutions provided by the Hybrid-EV committee of the Society of Automotive Engineers (SAE) [81]. All of the EV manufacturers include an AC level 1 solution for charging; however, an AC level 2 solution is recommended for reasonable charge times. To put the capabilities of the chargers into perspective, a 25 kWh battery with a 20% SOC (state of charge) requires 17 hours for a fully charged battery with the stock AC level 1 charger, whereas an AC level 2 charger can reduce the charging time to 1.2 hours. Furthermore, a fast-charge DC solution, e.g., a DC level 2 charger, can charge the battery in less than 20 minutes [81]. The fast DC charger will have an external inverter for the car, instead of an onboard solution, which suggests that it could provide reactive power support independent of the vehicle location. Currently, there is a very small penetration of EVs; however, it is projected that EVs will account for 24% of the American light-vehicle fleet and 64% of the annual vehicle sales by 2030 [82].

The remainder of this chapter is organized as follows. We discuss the policies and strategies associated with the two time-scale architecture in Section 6.2. Then, Section 6.3.1 introduces the development of the time-dependent loads for the system buses, provides the solar data for the PV installation, and formulates the EV charge schedules. Section 6.4 presents the case studies and the chapter is summarized in Section 6.5.

6.2 Integrating the Two Time-Scale Control

In this section, we discuss important design considerations that need to be taken into account when integrating the slow and fast time-scale optimizations without the methods competing with each other. We restate the optimization problems with a simplified notation to support a high-level discussion about the cost functions and control laws, which we validate with numerical simulations.

6.2.1 Two Time-Scale Optimization-Based Control

The slow time-scale optimization, which is discussed in detail in Chapter 3, has two important roles: (i) it provides a reference voltage, V^r, that meets specific operational objections for the fast time-scale to regulate to, and (ii) it sets the tap positions on the TCUL transformers. Each time the slow time-scale optimization is performed, we will execute it twice. The first run will return the continuous tap positions, which we are required to round to their nearest discrete values. We use these results to determine whether or not we want to dispatch the transformer tap positions. For example, we can have a secondary objective that limits the number of tap changes, so if the most recent optimization requires a single tap change, we may reject the solution. Then, we run the optimization a second time with the fixed tap positions to ensure the solution is feasible and improve its accuracy. The slow time-scale optimization has the form:

$$\min_{V,\, a,\, \tilde{q}} \; f_0(V, a, \tilde{q}) + \sum_i f_i(V, \tilde{q}) \tag{6.1a}$$

such that

$$f_p(V, a) = 0, \tag{6.1b}$$

$$f_q(V, a, \tilde{q}) = 0, \tag{6.1c}$$

and

$$\underline{V} \leq V \leq \overline{V}, \tag{6.1d}$$

$$\underline{q}^r \leq \tilde{q} \leq \overline{q}^r, \tag{6.1e}$$

$$\underline{a}V_p \leq V_{s'} \leq \overline{a}V_p, \tag{6.1f}$$

where $f_p(V, a)$ and $f_q(V, a, \tilde{q})$ represent the active and reactive power flow constraints for the system, respectively. We account for distribution line segment losses with $f_0(V, a, \tilde{q})$, which is required for the rank relaxation that we introduced in Chapter 3, and we will discuss how to handle the additional costs $f_i(V, \tilde{q})$ in Section 6.2.2. Note that on the second run of the optimization, (6.1f) becomes an equality constraint since the taps are fixed, e.g., $aV_{s'} = V_p$ for some specified tap ratio a that defines the relationship between the primary-side and virtual secondary-side voltages V_p and $V_{s'}$, respectively.

After we initialize the reference voltage, V^r with (6.1), we perform the following optimization for the fast time-scale control:

$$\min_{V,P,Q,q} \quad f(V, P, Q, q) \tag{6.2a}$$

such that

$$f_v(V, P, Q) = 0, \tag{6.2b}$$

$$f_p(P, Q) = 0, \tag{6.2c}$$

$$f_q(P, Q, q) = 0, \tag{6.2d}$$

and

$$\underline{q} \leq q \leq \overline{q}, \tag{6.2e}$$

where P and Q are the distribution line segment active and reactive power flows, respectively. The cost function, $f(V, P, Q, q)$, for the fast time-scale regulates the voltage magnitudes to the reference voltage. In Section 6.2.3, we provide operating criteria for the fast time-scale that indicates when to redispatch the system with the slow time-scale optimization.

Table 6.3: Cost Function Data

Figure	α_v	α_p	$f_2(V, \tilde{q})$	Power Factor
6.1(a)	0	0	2.5810	0.846
6.1(b)	15	0	0.0012	0.953
6.1(c)	0	10	0.5837	1.000
6.1(d)	5	50	0.0024	1.000

6.2.2 Slow Time-Scale Cost Functions

In Chapter 3, we defined a number of cost functions by $f_i(V, \tilde{q})$ such that $i \in \{1, 2, 3, 4\}$. We ignore the network losses defined by $f_1(V, \tilde{q})$, since the distribution line segment losses captured by $f_0(V, \tilde{q})$ account for most, if not all, of the network losses. In this section, we primarily consider the voltage regulation and power factor cost functions in the slow time-scale optimization, which are represented by $f_2(V, \tilde{q})$ and $f_3(V, \tilde{q})$, respectively. The final cost function, $f_4(V, \tilde{q})$, will penalize reactive power support usage and is designed to bias the solution of (6.1) to control the system with the TCUL transformers over the reactive power support $\tilde{q}$.

Voltage Regulation and Power Factor Correction

In the slow time-scale optimization, we seek a balance between regulating to some nominal system voltage, V^n, to meet customer needs and maintain the power factor at the feeder head to achieve the utility's desired operational objectives. The cost function will have the form:

$$C(V, a, \tilde{q}) = \underbrace{f_0(V, a, \tilde{q})}_{\text{losses}} + \underbrace{\alpha_v f_2(V, \tilde{q})}_{\text{voltage regulation}} + \underbrace{\alpha_p f_3(V, \tilde{q})}_{\text{power factor}}, \tag{6.3}$$

where $\alpha_v, \alpha_p \geq 0$ are the penalties for regulating voltage and power factor, respectively. In Table 6.3, we list the results of the system responses shown in Fig. 6.1. In Fig. 6.1(b), we found that dispatching system resources to regulate to $V^n = 1$ will improve the power factor dramatically, compared to the uncontrolled case in Fig. 6.1(a). Figure 6.1(c) shows the voltage profile for the 123-bus system operating at unity power factor in the static power flow. In Fig. 6.1(d), we achieve a good balance to satisfy both objectives.

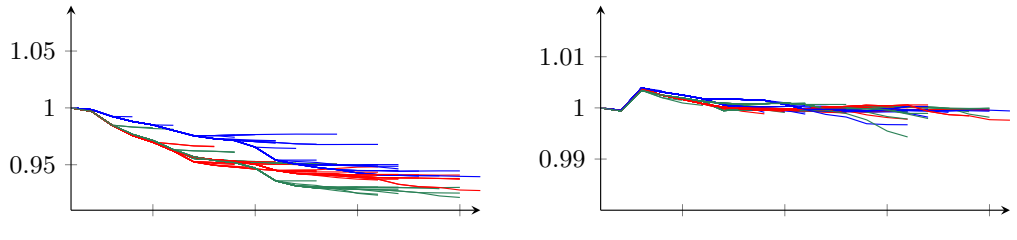

(a) Uncontrolled voltage profile.

(b) Regulating to nominal voltage.

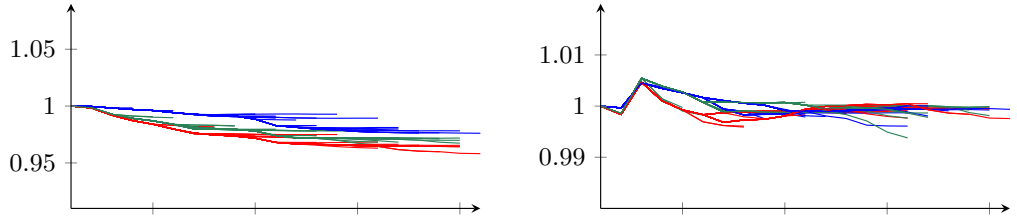

(c) Power factor correction.

(d) Combined voltage regulation and power factor correction.

Figure 6.1: Voltage profiles for various combinations of the penalties α_v, α_p.

Setting TCUL Transformer Tap Positions

Integrating the slow and fast time-scale optimizations creates a challenging problem to simultaneously dispatch both the TCUL transformer tap positions and reactive power support. In Chapter 2, we suggested that the limits on the available reactive power support for the slow and fast time-scale optimizations are not necessarily equal, e.g., we can provide additional up/down regulation in the fast time-scale optimization when $\underline{q} \leq \underline{q}^r$ and $\overline{q}^r \leq \overline{q}$. Figure 6.2 shows the switching behavior of the TCUL transformers and voltage responses of the network with various reactive power strategies.

First, we show in Fig. 6.2(a) the actions of the tap positions when the limits on $\tilde{q}$ in the slow time-scale optimization are 30% that of the fast time-scale limits, e.g., $\underline{q}^r = 0.3\,\underline{q}$ and $\overline{q}^r = 0.3\,\overline{q}$. The voltage response is displayed in Fig. 6.2(d). The controlled system response is an improvement over the uncontrolled case, which has an under-voltage around 18:00 hours, but there are a large number of oscillating single-tap changes, and the limited reactive power support restricts the ability of the system to track the nominal voltage.

Next, we found that if we match the limits, i.e., $\underline{q}^r = \underline{q}$ and $\overline{q}^r = \overline{q}$, then the ability of the system to track the nominal voltage is improved significantly, which is illustrated in Fig. 6.2(e) with the switching actions of the TCUL transformers shown in Fig. 6.2(b). For this case, we found that the optimiza-

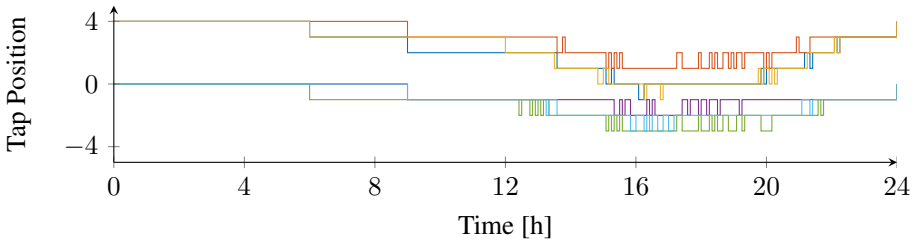

(a) Tap behavior with limited reactive power support.

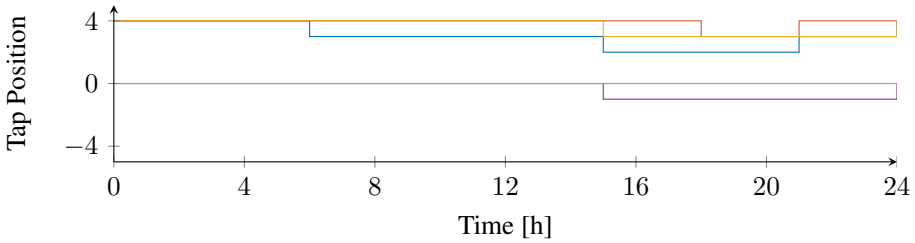

(b) Tap behavior with all available reactive power support.

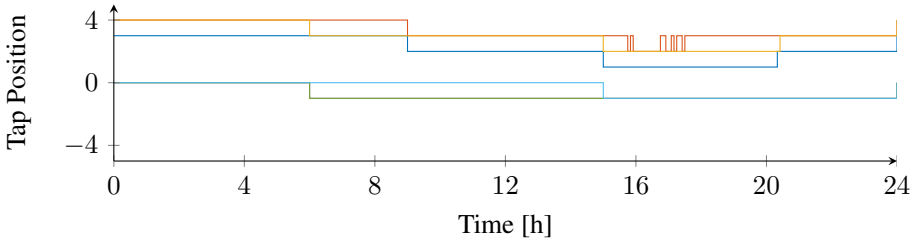

(c) Tap behavior with penalized reactive power support.

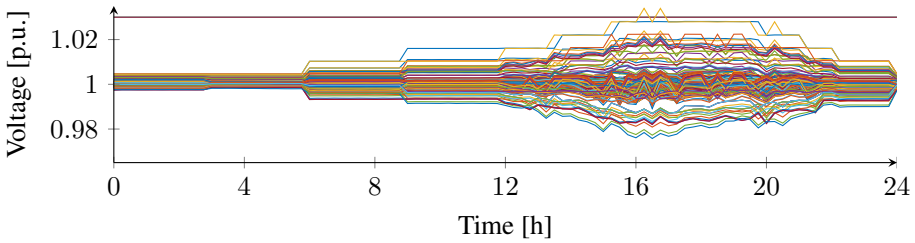

(d) Voltage response with limited reactive power support.

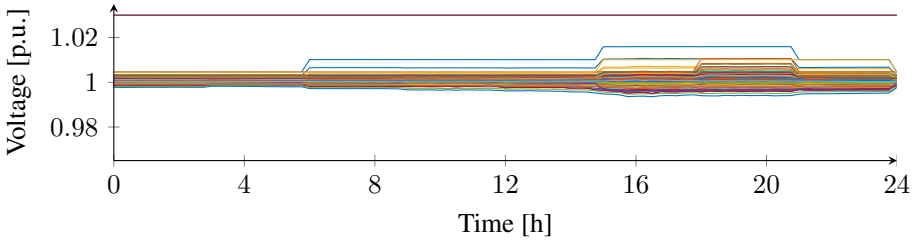

(e) Voltage response to all available reactive power support.

Figure 6.2: TCUL transformer tap behavior.

tion tends to favor the use of reactive power to regulate the bus voltages, thus reducing the number of tap changes. While we achieve a better voltage curve in this case, compared to limiting the reactive power support, we may want to avoid running reactive power resources at their limits, if it can be helped. We can bias the slow time-scale optimization towards moving the TCUL transformer taps by including an additional cost function, $f_4(V, \tilde{q})$, that penalizes the reactive power contributions. Figure 6.2(c) shows that while the control has full access to the network's reactive power capabilities, the dispatch for the transformer taps is more aggressive. There is a mild oscillation that occurs on a single tap between 16:00 and 18:00 hours, but we can easily filter out that behavior when we decide to accept the solution, i.e., we can limit the number of single-tap changes for a certain block of time.

6.2.3 Fast Time-Scale Redispatch Criteria

In the fast time-scale, we explicitly regulate the bus voltages until the current operating conditions fail to meet some performance criteria. In this chapter, we propose the following update rules to determine when a redispatch is necessary:

Designated Dispatch Schedule

In this section, we provide a number of criteria to redispatch the system resources; however, there are situations in which the system is operating within specifications, but we can find a better solution to the optimization. For example, the system can easily maintain the last dispatch after the heavy nighttime loading (after 21:00 hours), but we may want to rerun the optimization to reflect the reduced load, since most of the control rules are designed to combat disturbances. We can schedule the dispatches based on historical data for the time of day.

Power Factor Limits

Utility companies prefer that the feeder head operates with a unity power factor, e.g., no reactive power flow from the (sub)transmission system, since excess reactive power flow on the distribution line segments increases the line currents and limits the transfer of active power. The redispatch criteria that

monitors the phase with the lowest power factor and requires that

$$\min_{i\in\{0_a,0_b,0_c\}} \left\{ \cos\left(\tan^{-1}\left(\frac{Q_i}{P_i} \right) \right) \right\} > \varepsilon_p, \tag{6.4}$$

for some minimum power factor $\varepsilon_p > 0$, e.g., we can maintain a power factor greater than 0.85 with $\varepsilon_p = 0.85$.

Maximum Voltage Error

The fast time-scale optimization regulates the system voltages to V^r; however, $f(V, P, Q, q)$ in (6.2a) is the sum of the voltage errors and will not capture buses with severe deviations from the reference. Thus, we can monitor for the worse-case conditions and enforce

$$\| |V| - V^r \|_\infty < \varepsilon_v, \tag{6.5}$$

for some tolerance $\varepsilon_v > 0$. We can determine ε_v based on historical data or we can compare it to the voltage specifications, e.g.,

$$\varepsilon_v = \min\Big(V^r - 0.95,\ 1.05 - V^r \Big). \tag{6.6}$$

Deviation from Nominal Voltage

The previous rule detects the worst-case conditions for a single bus voltage, which will occur during heavy loading, but does not account for deviations away from the nominal voltage, V^n, since V^r is conditioned on the current operating point. Similar to the scheduled dispatches discussed earlier, this criteria detects situations where the slow time-scale optimization can be rerun after a disturbance has passed, rather than regulating to the reference set during the event. We can detect this with

$$\| \alpha_n \odot (|V| - V^n) \|_2 < \varepsilon_n, \tag{6.7}$$

for some tolerance $\varepsilon_n > 0$. The gain $\alpha_n \geq 0$ is included to filter out buses that can be ignored; i.e., buses directly connected to a feeder with a high voltage should not be considered, since their voltage will deviate very little from the feeder's voltage. It is also worth noting that this condition requires additional logic to be implemented, so a redispatch at every time step during a contingency event is not requested.

Costs to Regulate System Voltages

In addition to tracking the maximum bus voltage deviation, we can monitor the incremental costs to regulate the bus voltages with the dual variables λ_v, λ_q, which are associated with the voltage equality constraint (6.2b) and the reactive power constraint (6.2d) in the fast time-scale optimization, respectively. The desired operating criteria will be

$$\|\lambda_u\|_\infty < \varepsilon_u, \tag{6.8}$$

$$\|\lambda_q\|_\infty < \varepsilon_q, \tag{6.9}$$

for some tolerances $\varepsilon_u, \varepsilon_q > 0$, which can be determined based on the heuristics associated with previous solutions and operating conditions to determine the proper thresholds.

In Fig. 6.3, we show the results of a twenty-four hour simulation with a high penetration of PV installations and EVs. The slow time-scale is executed once at initialization, and then the fast time-scale optimization is performed otherwise to observe the behavior of the system parameters. The uncontrolled and controlled voltage responses are shown in Figs. 6.3(a) and 6.3(b), respectively. The voltage rise centered around 12:00 hours is a result of the active power injections from the PV installations, and the voltage drop in the evening is caused by the base load pickup with additional loading from the EVs. Interestingly, the significant active power generation around noon creates a reversal of the flow of active power at the feeder and causes the power factor shown in Fig. 6.3(c) to reach zero. This suggests that the minimum power factor, ε_p, should be a function of the state of the system rather than being strictly fixed. During time periods where the system is behaving in a conventional way, i.e., a net load without significant PV injections, we fix the power factor at a certain threshold; however, we ignore this criterion entirely as the net load approaches zero. For example, we can set $\varepsilon_p = 0.85$ and ignore the criteria if the power factor drops below $\varepsilon_{p'} = 0.2$ as the active power flow attenuates. Note that the cost function $f_3(V, \tilde{q})$ minimizes the reactive power transfer at the feeder, so it is possible for the power factor to be low as the flow of active power reverses directions and the magnitude of the reactive power transfer is small or negligible.

Figure 6.3(d) shows the signals for the maximum voltage error and deviation from nominal voltage described by (6.5) and (6.7), respectively. Using

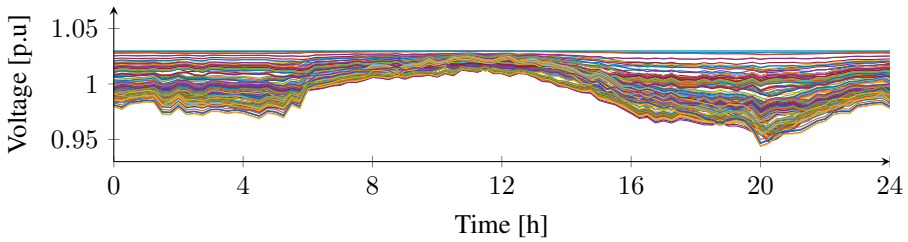

(a) Uncontrolled voltage response to load, PV injections, and EV charging.

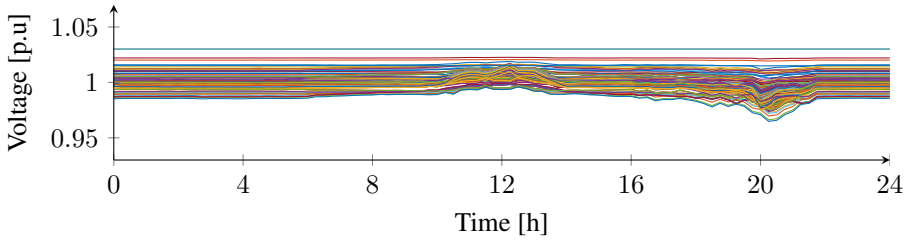

(b) Controlled voltage response to fast time-scale control.

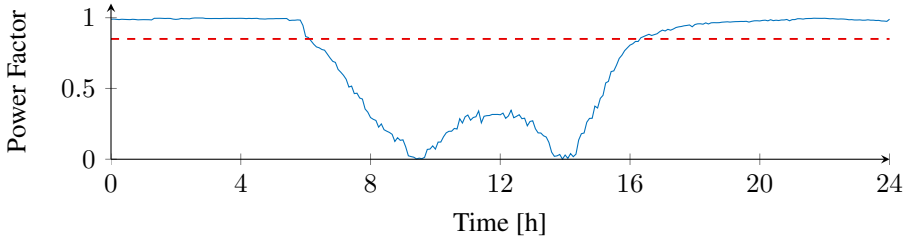

(c) System power factor at the feeder with 0.85 marked.

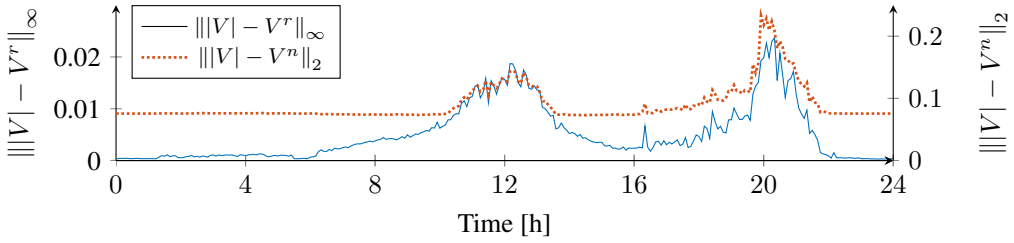

(d) Voltage errors from reference voltage V^r.

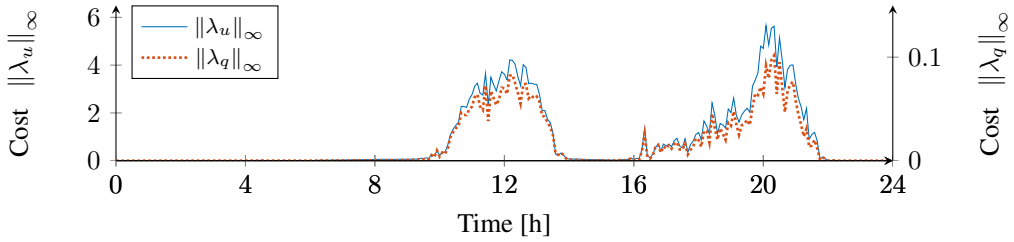

(e) Incremental cost to regulate voltage and reactive power equality constraints.

Figure 6.3: System response to the fast time-scale reactive power control.

the maximum voltage deviation to determine a redispatch of the reference voltage follows naturally since it indicates a disturbance; however, it will not identify when the contingency passes, and the system will continue to regulate to the last dispatch. Thus, the deviation from the nominal voltage is designed to restore the system to its undisturbed state. In practice, we can enforce the condition in (6.5) during a contingency case and monitor that the condition in (6.7) is met during normal operations.

Finally, we show the incremental voltage and reactive power costs from the dual variables in Fig. 6.3(e). Both the incremental costs to meet the voltage equality constraint, λ_u, and the reactive power equality constraint, λ_q, reflect the voltage error curves in Fig. 6.3(d). This result is intuitive in the sense that the reactive power support levels at certain system buses are hitting their limits, which results in higher incremental costs. In Section 6.4, we will monitor several system values and determine when to rerun the slow timescale optimization based on a combination of the desired operating criteria discussed in this section.

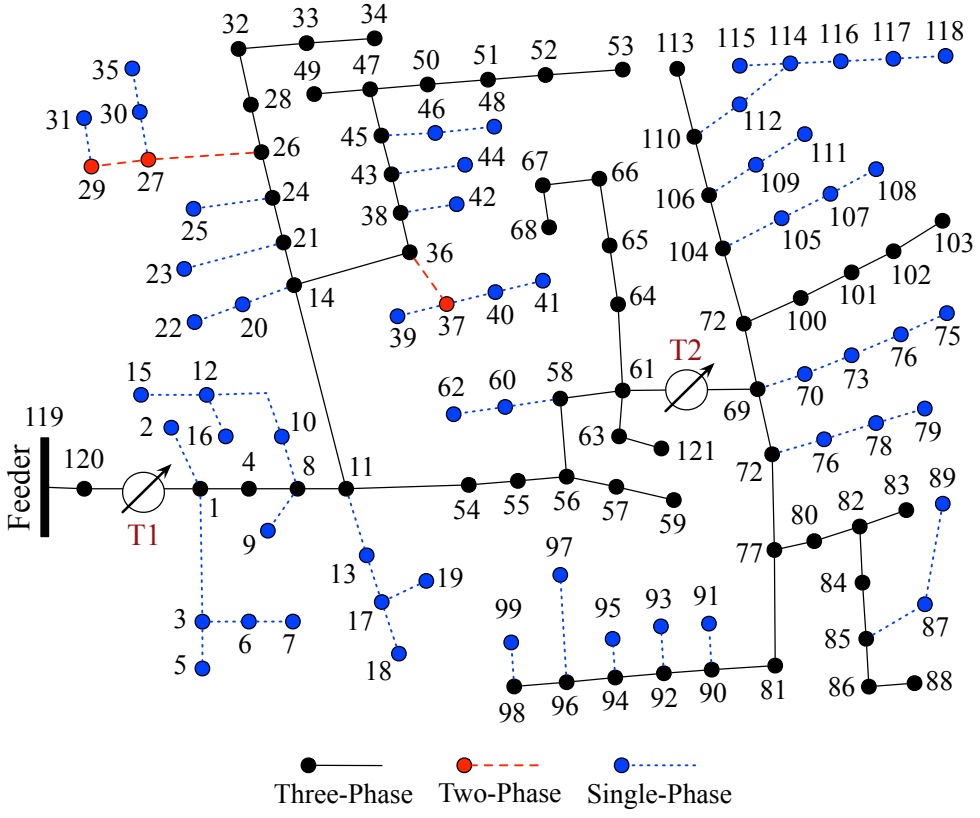

Figure 6.4: Modified IEEE 123-bus distribution system.

6.3 Load Models

In this section, we develop the load models for the system buses, installed PV systems, and EV charging profiles. Figure 6.4 shows the modified IEEE 123-bus test system [58], where we removed the fixed shunt capacitors and the two voltage regulators that were not three phase. We also moved the voltage regulator T1 from the distribution line segment $(119, 120)$ to $(120, 1)$ to simplify tracking the power factor at the feeder head in the slow time-scale optimization. This system contains a combination of single-, two-, and three-phase distribution line segment and system loads, along with two three-phase voltage regulators (the system data is provided in Appendix E.2).

6.3.1 Load Data

In order to develop a realistic loading profile, we utilized distribution-level load data from [83], which offers datasets on commercial and residential energy consumption. We assume that all of the loads in our case studies are residential, so that we can compare the total energy consumed by the network with the average residential energy consumption, in order to determine the number of consumers located at each bus based on the rated bus loads of the 123-bus distribution system. As we mentioned earlier, a typical American household consumed, on average, 953 kWh per month in 2010 and 903 kWh per month in 2012 [72], so we estimate that the average daily energy usage is approximately 30 kWh, since daily behaviors are cyclic.

Figure 6.5 shows a representative day in July for an aggregate residential

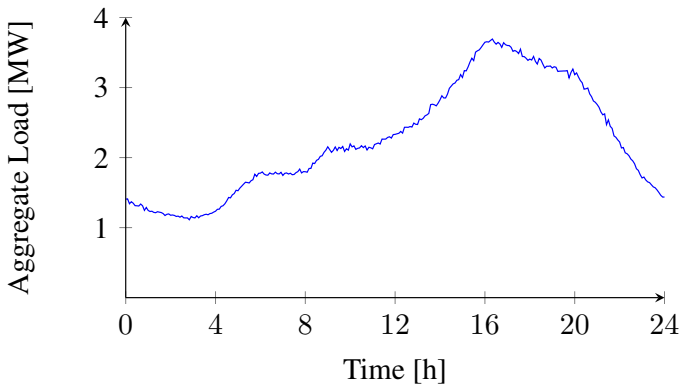

Figure 6.5: Single-day aggregate active power system loading.

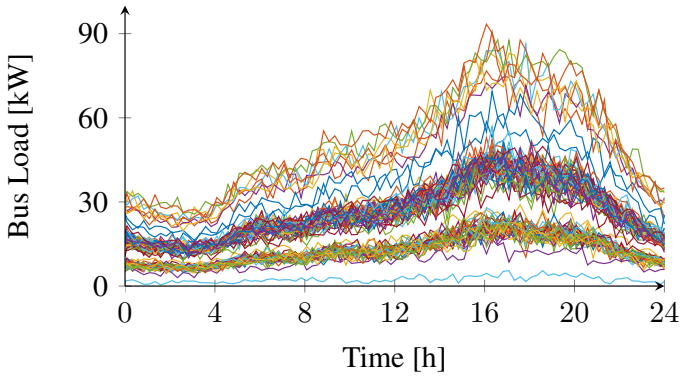

Figure 6.6: Single-day aggregate active power loading per bus.

load profile in Austin, Texas, where we assume that there are 1810 residential customers with a peak load of 3.69 MW based on the system data for IEEE 123-bus system. We increased the granularity of the original load data in [83] from an hourly to a five-minute time period t through a linear interpolation and an added random component. The resulting active power load curve is

$$P(t) = \tilde{P}(t) + \zeta \tilde{P}(t), \tag{6.10}$$

where ζ is a zero-mean normally distributed random variable with a variance of $\sigma = 0.01$ and $\tilde{P}(t)$ is the linear resulting five-minute load data. We generate the load curves for each customer by pseudo-randomly redistributing the total load at the time interval t between the customers, where the customer loads are required to be within specified limits. Then, we assign the number of customers attached to each bus according to the rated loads of the 123-bus system. Figure 6.6 shows the aggregated bus loads that sum to the curve in Fig. 6.5.

6.3.2 Solar Data

For generating realistic PV generation profiles, we used measured solar data from Austin, Texas for the month of July [84]. Figure 6.7 shows the normalized active power injections for a PV system with a five-minute granularity. Figure 6.7(a) provides an ideal generation curve, and Fig. 6.7(b) considers a scenario where shading from cloud cover occurs throughout the day.

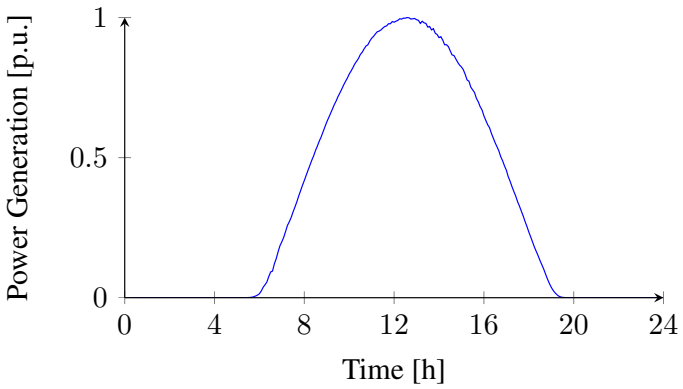

(a) Ideal active power generation.

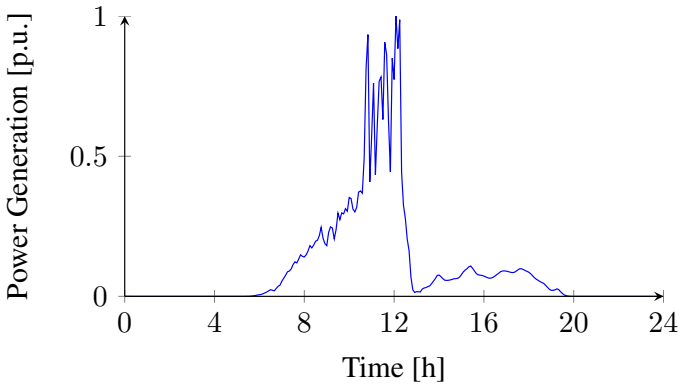

(b) Shaded active power generation.

Figure 6.7: Normalized solar active power generation curves.

6.3.3 EV Charge Schedule Data

We consider three electric vehicle charging scenarios: (i) worst-case EV charging, (ii) delayed-start EV charging, and (iii) optimized EV charging. In the worst-case EV charging scenario, the EVs are all charged with start times distributed between 19:00 and 20:00 hours, i.e., all vehicles are charged immediately upon returning home. In the delayed-start EV charging case, each EV is charged in a contiguous block and the start times of the charging are drawn from a uniform distribution, such that the vehicles' charge times begin between 19:00 hours and 03:00 hours. In the optimized EV charging schedule, the charging of the EVs in the distribution system is optimized to minimize the load increase during the charge period. We assume that the vehicles begin charging with a random SOC in $[0, 0.5]$ and finish with a SOC within $[0.9, 1]$.

Figure 6.8 shows the impact of the three charging schedules on the aggregated system load. In this example, we have 120 residential customers with an average daily energy usage of 30 kWh, and 36 EVs that have a maximum power draw of 7.2 kW and 50 kWh reservoir capacities. Figure 6.8(a) shows the worst-case scenario. We can mitigate the peak loading at 20:00 hours with both the delayed-start and optimal schedules shown in Figs. 6.8(b) and 6.8(c), respectively.

Optimal EV Scheduling

For a given day, we define $\mathcal{K}$ as the set of disjoint time intervals so that $\cup_{k\in\mathcal{K}} k$ accounts for the entire day, and each $k \in \mathcal{K}$ has a length of $\kappa > 0$ hours. Let $\mathcal{K}_c \subset \mathcal{K}$ be the time periods in which EV charging is permitted. Then, we define $\mathcal{R}$ as the set of all EVs, where each $i \in \mathcal{R}$ has a charging efficiency of ξ_i to charge the battery from its initial E_i^o to its final state E_i^f. Within each time period, $k \in \mathcal{K}$, EV i has a constant power draw $P_i^v[k]$ that is constrained by $\underline{P}_i^v$, $\overline{P}_i^v$, e.g., $\underline{P}_i^v = 0$ when the charger is not in use and $\overline{P}_i^v$ can be its rated load.

We create a fictional generator with quadratic generation costs $C\left(P_G[k]\right)$, where $P_G[k]$ is the active power provided by the feeder at time instance $k \in \mathcal{K}$. The generator must produce enough active power to satisfy both the forecasted system demand $P_D[k]$ and EV charging schedules. Thus, we can formulate the optimization problem as

$$\min_{P_G} \sum_{k\in\mathcal{K}_c} C\left(P_G[k]\right) \tag{6.11a}$$

such that

$$\sum_{i\in\mathcal{V}} P_i^v[k] = P_G[k] - P_D[k], \qquad \forall k \in \mathcal{K}_c, \tag{6.11b}$$

$$\kappa \sum_{k\in\mathcal{K}_c} P_i^v[k] = \frac{1}{\xi_i}\left(E_i^f - E_i^o\right), \qquad \forall i \in \mathcal{R}, \tag{6.11c}$$

and

$$\underline{P}_i^v \;\le\; P_i^v[k] \;\le\; \overline{P}_i^v, \qquad \forall i \in \mathcal{R}, \;\; \forall k \in \mathcal{K}_c, \tag{6.11d}$$

where the EV energy charge constraint in (6.11c) accounts for the energy required to charge EV $i \in \mathcal{R}$ and its losses.

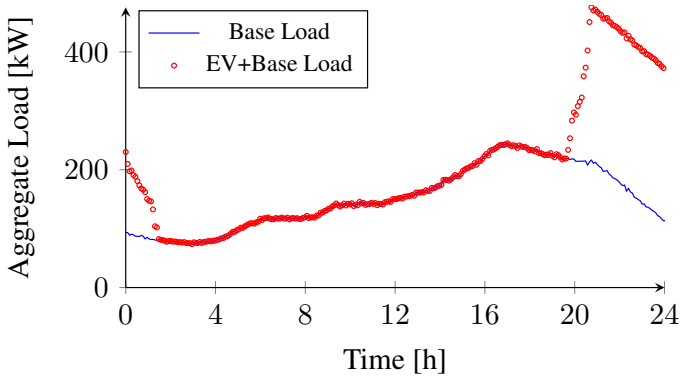

(a) Worst-case EV charging schedule.

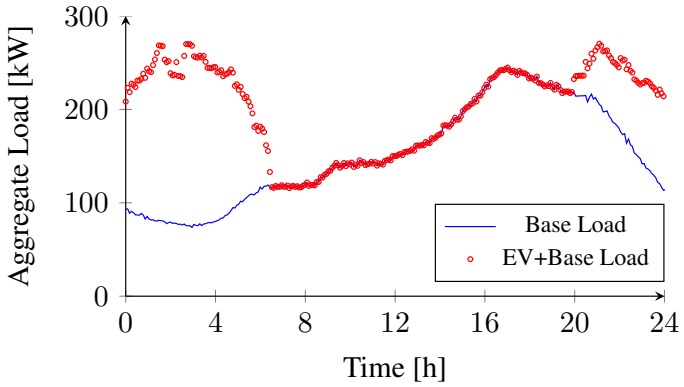

(b) Delayed-start EV charging schedule.

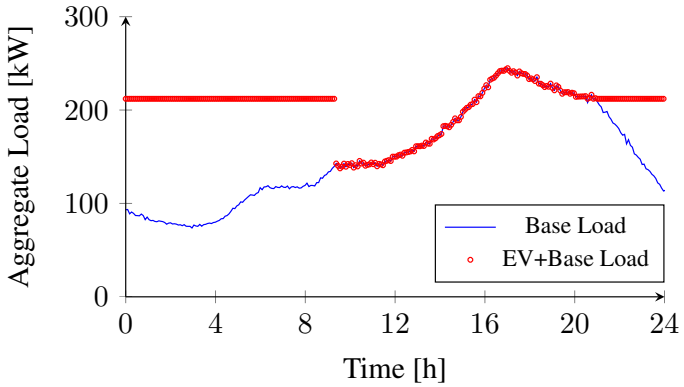

(c) Optimized EV charging schedule.

Figure 6.8: Impacts on system load by the EV charging schedules.

6.4 Case Studies

In this section, we demonstrate the ability of the two time-scale control architecture to optimize and regulate the modified IEEE 123-bus unbalanced three-phase distribution system with a significant number of DERs attached.

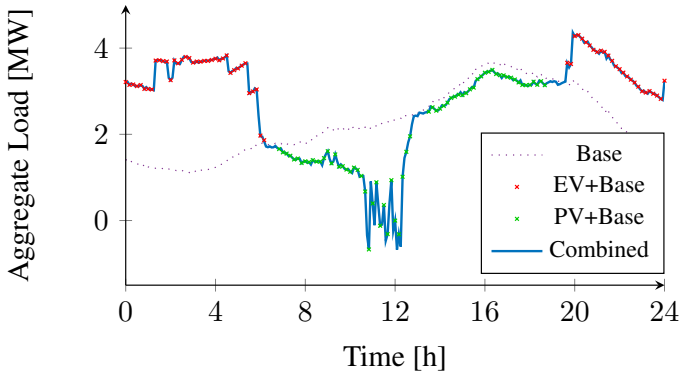

(a) 123-bus aggregate load curve.

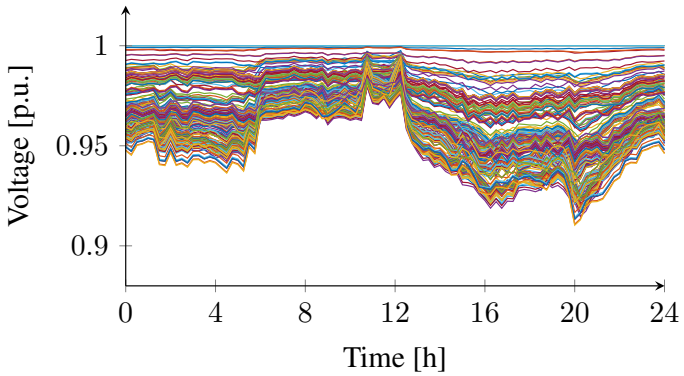

(b) 123-bus uncontrolled voltage response.

Figure 6.9: Uncontrolled 123-bus system values.

We use the base load described in Section 6.3.1 and assume that there is a 30% penetration of both PV installations and EVs. The PV installations are assigned the shaded active power generation curve shown in Fig. 6.7(b) and have a capacity of 5.7 kW. The EVs will follow the delayed charging schedule shown in Fig. 6.8(b). We assume that all of the EVs have a 50 kWh battery and either an AC level 2 or a DC level 1 solution that have a peak charging capacity of 7.2 kW. Figure 6.9 shows the aggregated load and the uncontrolled voltage response of the system. We fix the feeder's voltage at 1 p.u. and the system experiences an under-voltage of 0.91 p.u., which is outside of the required $\pm 5\%$ of the nominal voltage specification.

We assume that all of the inverters used for the PV installations and the DC EV chargers are capable of providing reactive power support for the slow and fast time-scale optimizations. Suppose that 20% of the owners with EVs have DC chargers, then the available reactive power support will be

$$\overline{q}(t) = \sum_{i \in \mathcal{N}} \sqrt{S_i^2(t) - P_i^2(t)} + 0.2 \sum_{r \in \mathcal{R}} \overline{P}_r^v, \tag{6.12}$$

$$\underline{q}(t) = -\overline{q}(t), \tag{6.13}$$

where the reactive power capabilities of PV inverters are a function of their power injection, and we assume DC charger solutions can provide $\overline{P}_r^v$ of reactive power support at all times.

We perform two case studies in this section: (i) the slow time-scale optimization tracks the nominal voltage, and (ii) the slow time-scale also provides power factor correction in addition to tracking the voltage. Algorithm 2 provides the control logic to redispatch the system during the voltage regulation stage (fast time-scale). We will always rerun the slow time-scale optimization if the system fails to regulate the bus voltages to V^r in the fast time-scale control; otherwise, we monitor the voltage deviation from the nominal voltage, V^n, and the power factor. In the case that the system is operating outside of a desired tolerance from V^n, we check the current and previous

Algorithm 2: Signal a Redispatch of the Slow Time-Scale Control

Input : $V(t)$, $V^r(t)$, $\lambda_u(t)$, $P_0(t)$, $Q_0(t)$
Output: s_s
Data: V^n, $\varepsilon_v = 0.01$, $\varepsilon_n = 0.065$, $\varepsilon_u = 0.05$, $\varepsilon_p = 0.85$, $\varepsilon_{p'} = 0.2$, α_p
begin
initialize:

$$s = false[5]$$
$$p_f = \cos\left(\tan^{-1}\left(Q_0(t)/P_0(t)\right)\right), \quad P_0(t) \neq 0$$

if $\left\| |V(t)| - V^r(t) \right\|_\infty > \varepsilon_v$ **then** $s[0] = true$;

if $\left\| |V(t)| - V^n \right\|_2 > \varepsilon_n$ **then** $s[1] = true$;

if $\left\| \lambda_u(t) \right\|_\infty < \varepsilon_u$ **then** $s[2] = true$;

if $\left\| \lambda_u(t-1) \right\|_\infty < \varepsilon_u$ **then** $s[3] = true$;

if $(\alpha_p \neq 0) \wedge (p_f < \varepsilon_p) \wedge (p_f > \varepsilon_{p'})$ **then** $s[4] = true$;

return : $s_s = s[0] \vee \left(\bigwedge_{i=1}^{3} s[i]\right) \vee s[4]$

incremental costs to regulate the bus voltages with dual variables from the fast time-scale optimization, e.g., $\lambda_u(t)$ and $\lambda_u(t-1)$, since comparing multiple time steps acts as a filter. The intuition behind this is that most of the criteria described in Section 6.2.3 react to disturbances and (6.7) restores the system to a nominal state. We reference the incremental costs to detect if the disturbance has passed because λ_u will be large when the reactive power resources are expensive to maintain V^r. The logic to detect the power factor will attempt to keep the system above $\varepsilon_p = 0.85$; however, we ignore this rule when the power factor drops below $\varepsilon_{p'} = 0.2$, which occurs when there is a large amount of active power generation present in the system. Note that we can achieve similar results to detect when to ignore the power factor as $\varepsilon_{p'}$ by monitoring the active power flow at the feeder.

6.4.1 Voltage Regulation

In this case study, we select the cost function of the slow time-scale optimization to track V^n and penalize the usage of reactive power to bias the solution toward using the TCUL transformers to control the system. Figure 6.10 shows the system response to our proposed control architecture. The bus voltages in Fig. 6.10(a) are centered around 1 p.u., with $V_i \in [0.980, 1.018]$ for all $i \in \mathcal{N}$. The control actions for the reactive power support and the TCUL transformer taps are shown in Figs. 6.10(b) and 6.10(c), respectively.

6.4.2 Power Factor Correction and Voltage Regulation

Next, we include a penalty for power factor correction in the slow time-scale optimization. Figure 6.11 shows the controlled system responses to the new cost function. The bus voltages are maintained within $V_i \in [0.975, 1.018]$ for all $i \in \mathcal{N}$. The power factors for both cases are shown in Fig. 6.12, where the overall power factor is improved in the presence of significant active power generation around 12:00 hours; otherwise, the curves are similar when power factor correction is less critical.

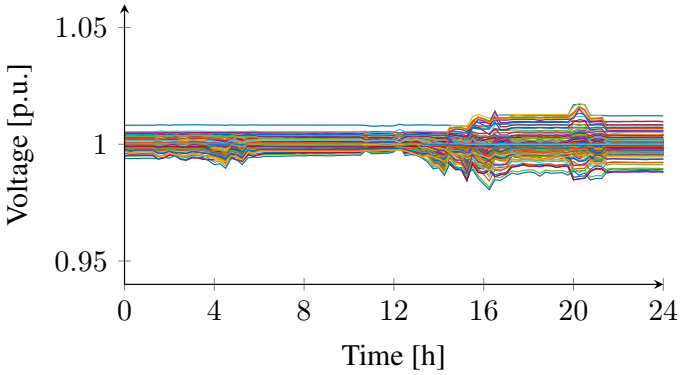

(a) 123-bus controlled voltage response.

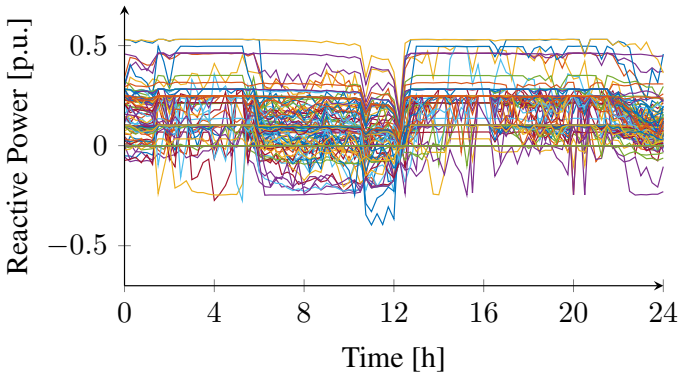

(b) 123-bus reactive power support.

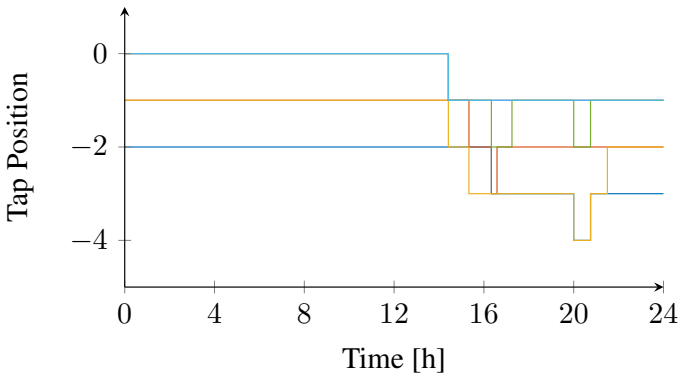

(c) 123-bus TCUL transformer tap changing behavior.

Figure 6.10: Controlled 123-bus system for strictly voltage regulation.

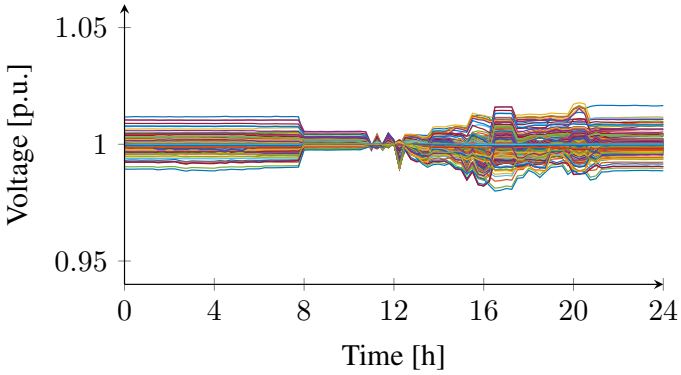

(a) 123-bus controlled voltage response.

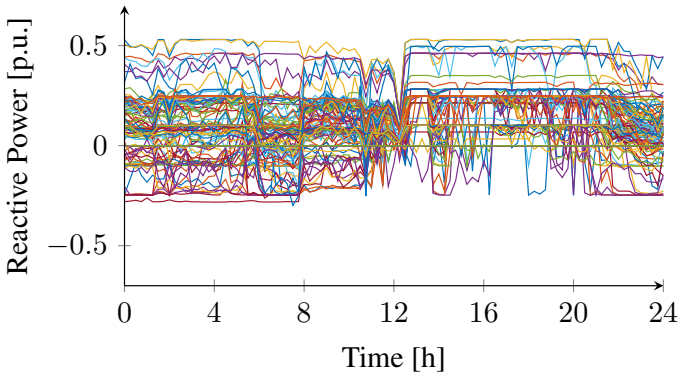

(b) 123-bus reactive power support.

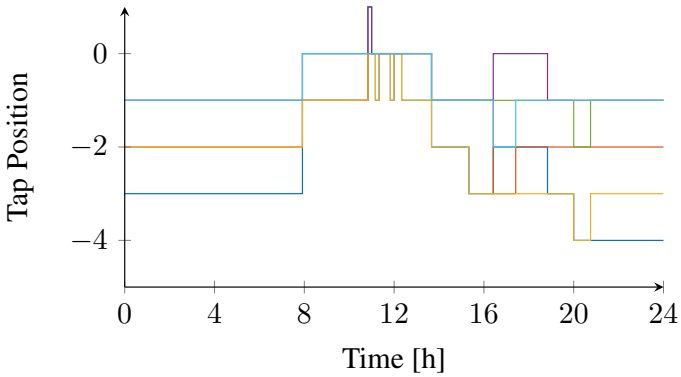

(c) 123-bus TCUL transformer tap changing behavior.

Figure 6.11: Controlled 123-bus system for both voltage regulation and power factor correction.

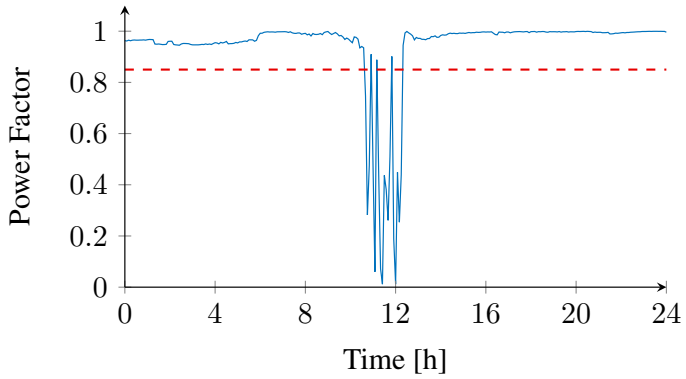

(a) Uncontrolled power factor curve ($\alpha_p = 0$).

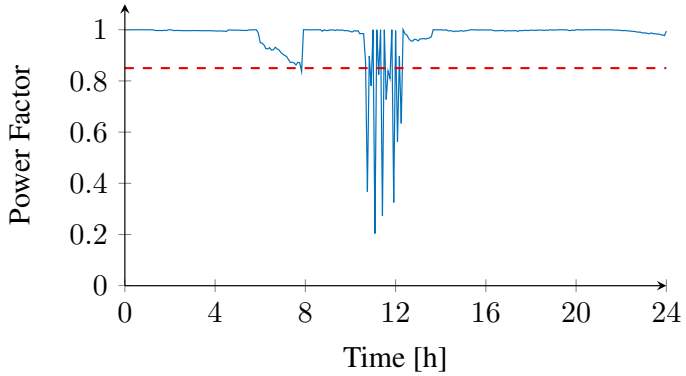

(b) Controlled power factor curve.

Figure 6.12: A comparison between the power factors for the two cases.

6.5 Summary

In this chapter, we implement the two time-scale control architecture introduced in Chapter 2. We provided a number of examples to demonstrate how to choose the cost function for the slow time-scale optimization, and we discussed several possible operational criteria to determine the control law that redispatches the system based on the results of the fast time-scale optimization. Then, we described how to generate the system data using a number of parameters for the rated load and the DERs present in the network. Finally, we presented several case studies that demonstrate the two time-scale architecture's ability to control a 123-bus unbalanced three-phase distribution network.

CHAPTER 7

CONCLUDING REMARKS

In this chapter, we present a summary of the thesis and highlight its main contribution towards achieving optimal voltage control in unbalanced three-phase distribution systems. This chapter (and thesis) concludes with the author's final thoughts and observations.

7.1 Thesis Summary and Contributions

Chapter 2. In this chapter, we described our hierarchical control architecture in which we perform separate optimizations for the slow and fast time-scale control of the system devices, and we provided a high-level overview of the optimization- and feedback-based control methods proposed in this thesis. The slow time-scale actuators will, in general, be existing devices, e.g., the tap positions of tap-changing under load (TCUL) transformers, that will be dispatched at appropriate time intervals to reduce the wear on their mechanical parts. In contrast, the fast time-scale resources are considered to be devices that connect to the grid through power electronics, e.g., the inverters on photovoltaic (PV) installations, and will be used to mitigate the variability introduced by the distributed energy resources (DERs) and flatten the voltage profile of the distribution network.

Chapter 3. In this chapter, we formulated the slow time-scale control problem with the objective to optimally set the tap position of voltage regulation transformers in distribution systems. We cast the problem as a rank-constrained semidefinite program (SDP), where the transformer tap ratios are captured by (i) introducing a secondary-side 'virtual' bus per transformer, and (ii) constraining the values that these virtual bus voltages can take according to the limits on the tap positions. We use the solution of the relaxed SDP to compute the tap positions with the ratios between the primary-side

bus voltages and the secondary-side virtual bus voltages. In order to solve the problem, we introduced a distributed algorithm based on the Alternating Direction Method of Multipliers (ADMM).

Chapter 4. This chapter was the first of the two chapters that focused on voltage regulation for the fast time-scale control. In this chapter, we provided a feedback-based approach where the local controller at each bus of the network monitors the bus voltage, and whenever there is a voltage violation, locally available information is used to estimate the amount of reactive power that needs to be injected into the bus to correct the violation. Then, if the DERs fail to correct all of the limit violations, we provided a secondary control action that requests additional reactive power support from other controllers at neighboring buses through a distributed algorithm, which relies on a local exchange of information among neighboring controllers. The strength of this approach is that it requires very little information about the network in order to operate, and it has a simple communication infrastructure for the secondary control. While this method was able to clear faults, the reactive power support problem is a regional problem and is better suited for an optimization-based approach.

Chapter 5. In this chapter, we advanced the ideas presented in Chapter 4 and developed an optimization-based fast time-scale control that optimally sets the reactive power contributions of DERs with the goal of regulating bus voltages. We formulated the problem as an optimal power flow (OPF) with the branch flow modeling approach and relaxed the nonlinear terms of the equality constraints, based on the operating conditions and desired voltage profile. Similar to the slow time-scale optimization, we leveraged the ADMM algorithm introduced in Chapter 3 to efficiently solve the convex quadratic program (QP).

Chapter 6. Finally, we combined the slow and fast time-scale optimization-based controls proposed in Chapters 2 and 5, respectively. The focus of this chapter was: (i) to discuss the intuition behind defining the multi-objective cost function for the slow time-scale optimization, (ii) to define several control laws to determine when to switch between the optimizations, and (iii) to develop an accurate system model where we generated the aggregate load models of the system buses, the active power injections of photo-

voltaic (PV) installations, and uncontrolled/controlled electric vehicle (EV) charging schedules. We conclude the chapter by simulating the proposed architecture in an unbalanced three-phase distribution system for a twenty-four hour period.

7.2 Conclusion

In this thesis, we proposed several approaches to control devices in unbalanced three-phase distribution networks with the objectives of regulating voltage. In Chapter 3, we formulated an SDP-based optimization problem to optimally dispatch the system, based on several performance criteria. While this approach captures the nonlinearities that the reduced model in Chapter 5 estimates, it is not a practical approach for fast regulation, since the complexity of the problem scales exponentially.

To address the fast voltage regulation in an optimal manner, we developed the approximate model in Chapter 5, which can quickly and accurately regulate to a desired set-point, but it is not designed to consider the entire solution space. This interaction of the slow time-scale optimization versus the fast time-scale regulation has an interesting dichotomy that merits more research. For example, how do we balance performance specifications that benefit both the utilities and the customers? What is an appropriate control action to switch between the time-scale optimizations? In Chapter 6, we provided intuition and preliminary results to explore these questions. We can also incorporate additional cost functions, i.e., we could potentially include optimization variables for active injections/loads to provide demand response and balance the perceived load at the feeder.

We envision that the control and optimization of future distribution systems will require a number of control and optimization routines that operate at different time-scales working in tandem with each other to reach both mutual and time-scale specific goals. This thesis provides a number of tools to develop a basis for this approach to control unbalanced three-phase distribution systems, but there is still a lot more work required to realize this vision in a physical system. The proposed control architecture and algorithms will require real-time monitoring equipment, and there are several computational and communication aspects to consider for the control hardware.

APPENDIX A

RELAXATION AND DEVELOPMENT OF THE SDP FORMULATION

In this appendix, we provide the proof for the global optimality of the relaxed SDP formulation and give a numerical example to motivate the formulate of the non-ideal transformer model.

A.1 Global Optimality of the Relaxed SDP

In this section, we provide a proof that the rank relaxation can achieve the global optimum of the non-convex formulation. The latter refers to the original optimization problem which only augments the relaxed one (3.18a) with an additional constraint $\text{rank}(W) = 1$.

The sketch proof leverages the earlier results in [31]. To this end, we define regarding the set of two-way real power flow along line $(i, k) \in \mathcal{E}$ with fixed bus voltage magnitudes $\boldsymbol{\upsilon}$, as

$$\mathcal{F}_{ik}(\boldsymbol{\upsilon}) := \left\{ (P_{ik}, P_{ki}) \ : \ \begin{array}{c} |V_i| = \upsilon_i, \\ |V_k| = \upsilon_k \end{array} \right\}, \quad \forall (i,k) \in \mathcal{E}. \tag{A.1}$$

Furthermore, additional line thermal limits are needed to characterize the power flow region, as given by

$$\mathcal{F}^{\theta}_{ik}(\boldsymbol{\upsilon}) := \left\{ (P_{ik}, P_{ki}) \ : \ \begin{array}{c} |V_i| = \upsilon_i, |V_k| = \upsilon_k, \\ \underline{\theta}_{ik} \leq \theta_{ik} \leq \bar{\theta}_{ik} \end{array} \right\}, \tag{A.2}$$

for all $(i, k) \in \mathcal{E}$. The upper and lower bounds of the thermal limits are set depending on the line admittance values, as

$$-\tan^{-1}\left(\frac{b_{ik}}{g_{ik}}\right) < \underline{\theta}_{ik} < \bar{\theta}_{ik} < \tan^{-1}\left(\frac{b_{ik}}{g_{ik}}\right). \tag{A.3}$$

It is known that the phase difference along any line is practically close to 0, and thus the thermal limit conditions are fairly reasonable.

Leveraging the arguments in [31], it can be shown that the relaxed SDP method essentially replaces the non-convex power flow region by its convex hull,[1] i.e., $(P_{ik}, P_{ki}) \in \text{conv}(\mathcal{F}_{ik}^{\theta}(\boldsymbol{v}))$. Using [31, Lemma 1], it is possible to further argue that

$$\mathcal{O}(\mathcal{F}_{ik}^{\theta}(\boldsymbol{v})) = \mathcal{O}(\text{conv}(\mathcal{F}_{ik}^{\theta}(\boldsymbol{v}))). \tag{A.4}$$

Notice this also applies to the virtual line (p_t, s_t'). Since there is no power loss, the two-way real power flow simply needs to satisfy $P_{p_t s_t'} + P_{s_t' p_t} = 0$. Hence, the power flow region $\mathcal{F}_{p_t s_t'}^{\theta}$ is just a line, and it would be exactly the same as its convex hull.

To account for the variable voltage levels, one needs to define the set of voltage magnitude values for all buses

$$\mathcal{V} := \left\{ [|V_i|]_{i\in\mathcal{N}} \ : \ \begin{array}{c} \underline{V} \le |V_i| \le \overline{V}, \ \forall i \in \mathcal{N}_b, \\ \underline{a}|V_{p_t}| \le |V_{s_t'}| \le \overline{a}|V_{p_t}| \end{array} \right\}. \tag{A.5}$$

With this, the overall set of bus power injection is given by

$$\mathcal{P} := \bigcup_{\boldsymbol{v}\in\mathcal{V}} \left\{ \left[\sum_{k\in\mathcal{N}_i} P_{ik} \right]_{i\in\bar{\mathcal{N}}}, (P_{ik}, P_{ki}) \in \mathcal{F}_{ik}^{\theta}(\boldsymbol{v}) \right\}. \tag{A.6}$$

As mentioned earlier, the relaxed SDP approach would essentially relax $\mathcal{P}$ to its convex hull. Furthermore, $\mathcal{P}$ is a linear combination of all the power flow regions, and the union operator does maintain the linearity of this mapping. This is leads to the fact that $\mathcal{P}$ and $\text{conv}(\mathcal{P})$ have the same Pareto-optimal points; i.e., $\mathcal{O}(\mathcal{P}) = \mathcal{O}(\text{conv}(\mathcal{P}))$. Hence, the relaxed problem (3.18a) is guaranteed with be a valid power flow solution, which is also the global optimum to the original problem.

[1] In fact, the second-order cone program (SOCP) relaxation would actually convex all the power flow region on the line-by-line basis, but the relaxed SDP can be shown equivalent to the SOCP relaxation.

A.2 Development of the Non-Ideal Transformer Model

The transformer constraints originally proposed in [54] for a balanced network are given by

$$\underline{a}^2 \left|V_{p_t}\right|^2 \leq \left|V_{s'_t}\right|^2 \leq \overline{a}^2 \left|V_{p_t}\right|^2 \tag{A.7a}$$

$$\mathrm{Re}\left\{V_{p_t}\right\} \times \mathrm{Im}\left\{V_{s'_t}\right\} = \mathrm{Re}\left\{V_{s'_t}\right\} \times \mathrm{Im}\left\{V_{p_t}\right\} \tag{A.7b}$$

$$\mathrm{Re}\left\{V_{p_t}\right\} \times \mathrm{Re}\left\{V_{s'_t}\right\} \geq 0 \tag{A.7c}$$

$$\mathrm{Im}\left\{V_{p_t}\right\} \times \mathrm{Im}\left\{V_{s'_t}\right\} \geq 0, \tag{A.7d}$$

which are equivalent to

$$\underline{a}^2 \left[W\right]_{p_t p_t} \leq \left[W\right]_{s'_t s'_t} \leq \overline{a}^2 \left[W\right]_{p_t p_t} \tag{A.8a}$$

$$\left[W\right]_{p_t s'_t} - \left[W\right]_{s'_t p_t} = 0 \tag{A.8b}$$

$$\left[W\right]_{p_t s'_t} \geq 0 \text{ and } \left[W\right]_{s'_t p_t} \geq 0 \tag{A.8c}$$

for the SDP formulation based on complex vectors/matrices.

A.2.1 Single-Phase Symbolic Example

Consider a radial, single-phase 3-bus network that contains an ideal TCUL transformer between buses 1 and 2. Let bus 1 be the reference bus and have a fixed voltage of $V_1 \angle \theta_1$. Thus, the voltages are given by

$$V = \begin{bmatrix} V_1\angle\theta_1 \\ V_2\angle\theta_2 \\ V_3\angle\theta_3 \end{bmatrix} = \begin{bmatrix} V_1\angle\theta_1 \\ aV_1\angle\theta_1 \\ V_3\angle\theta_3 \end{bmatrix}, \tag{A.9}$$

where a is the tap ratio of the transformer. Note that in (A.9), we define $V_2 = aV_1$ instead of $V_2 = \frac{1}{a}V_1$ as in Chapter 3. The outer product of the voltages is given by

$$VV^H = W = \begin{bmatrix} V_1^2 & V_1V_2\angle(\theta_1-\theta_2) & V_1V_3\angle(\theta_1-\theta_3) \\ V_1V_2\angle(\theta_2-\theta_1) & V_2^2 & V_2V_3\angle(\theta_2-\theta_3) \\ V_1V_3\angle(\theta_3-\theta_1) & V_2V_3\angle(\theta_3-\theta_2) & V_3^2 \end{bmatrix}. \tag{A.10}$$

The desired rank-1 solution will be

$$W = \begin{bmatrix} V_1^2 & aV_1^2 & V_1V_3\angle(\theta_1-\theta_3) \\ aV_1^2 & a^2V_1^2 & aV_1V_3\angle(\theta_1-\theta_3) \\ V_1V_3\angle(\theta_3-\theta_1) & aV_1V_3\angle(\theta_3-\theta_1) & V_3^2 \end{bmatrix}; \tag{A.11}$$

however, the solution from the SDP problem with the constraints in (A.7a)–(A.7d) will have the form

$$W = \begin{bmatrix} V_1^2 & w_{12} & w_{13} \\ w_{21} & a^2V_1^2 & aV_1V_3\angle(\theta_2-\theta_3) \\ w_{31} & aV_1V_3\angle(\theta_3-\theta_2) & V_3^2 \end{bmatrix}, \tag{A.12}$$

where $w_{12} = w_{21}$ and $w_{13} = w_{31}^*$ can vary as long as the positive semidefinite (PSD) constraint is met and W will satisfy the power flow constraints in the SDP OPF since the underlying graph is disconnected between buses 1 and 2 (i.e., the relationship between buses 1 and 3 is irrelevant in terms of the power flow constraints).

From this example, it is clear why the solution to the SDP, $W \in \mathbb{C}^{3\times3}$, can and will return a solution with rank higher than 1. We can recover the rank-1 solution by finding the relative voltage magnitude/angle per partition and setting $\theta_2 = \theta_1$. In a larger system, the r transformers disconnect the network graph and create $r + 1$ partitions where the secondary-side virtual bus in each partition will behave as a local reference bus. Thus, the phase of the buses located in that partition are defined relative to the secondary side of the transformer and not the feeder. We can recover the rank-1 solution by starting with the partition that contains the feeder and recursively adjust the phase angles in the downstream partitions.

The non-ideal transformer model can address the higher-rank since: (i) it connects the network so that $w_{13} = w_{31}^*$ is no longer ambiguous, and (ii) it ensures that $\theta_2 \approx \theta_1$. This will return a rank-1 solution to the SDP OPF with the caveat that the solution is sensitive to the choice of z_t. For the single-phase case, the non-ideal transformer is not necessary to find a rank-1 solution or determine other control variables such as reactive power support or the optimal tap ratio.

A.2.2 Multi-Phase Symbolic Example

Next, we consider a 2-bus, two-phase system with an ideal TCUL transformer connecting the buses. The bus voltages for the primary and secondary sides of the TCUL transformer are

$$\boldsymbol{V} = \begin{bmatrix} V_a\angle\theta_a \\ V_b\angle\theta_b \\ \tilde{V}_a\angle\tilde{\theta}_a \\ \tilde{V}_b\angle\tilde{\theta}_b \end{bmatrix} = \begin{bmatrix} V_a\angle\theta_a \\ V_b\angle\theta_b \\ a_aV_a\angle\theta_a \\ a_bV_b\angle\theta_b \end{bmatrix}, \tag{A.13}$$

and the outer product of the voltages is

$$\boldsymbol{W} = \left[\begin{array}{cc|cc} V_a^2 & V_aV_b\angle\theta_{ab} & V_a\tilde{V}_a\angle\theta_{a\tilde{a}} & V_a\tilde{V}_b\angle\theta_{a\tilde{b}} \\ V_aV_b\angle\theta_{ba} & V_b^2 & V_b\tilde{V}_a\angle\theta_{b\tilde{a}} & V_b\tilde{V}_b\angle\theta_{b\tilde{b}} \\ \hline V_a\tilde{V}_a\angle\theta_{\tilde{a}a} & V_b\tilde{V}_a\angle\theta_{\tilde{a}b} & \tilde{V}_a^2 & \tilde{V}_a\tilde{V}_b\angle\theta_{\tilde{a}\tilde{b}} \\ V_a\tilde{V}_b\angle\theta_{\tilde{b}a} & V_b\tilde{V}_b\angle\theta_{\tilde{b}b} & \tilde{V}_a\tilde{V}_b\angle\theta_{\tilde{b}a} & \tilde{V}_b^2 \end{array}\right], \tag{A.14}$$

where $\theta_{ik} = \theta_i - \theta_k$. The desired rank-1 solution of $\boldsymbol{W}$ is

$$\boldsymbol{W} = \left[\begin{array}{cc|cc} V_a^2 & V_aV_b\angle\theta_{ab} & a_aV_a^2 & a_bV_aV_b\angle\theta_{ab} \\ V_aV_b\angle\theta_{ba} & V_b^2 & a_aV_aV_b\angle\theta_{ba} & a_bV_b^2 \\ \hline a_aV_a^2 & a_aV_aV_b\angle\theta_{ab} & a_a^2V_a^2 & a_aa_bV_aV_b\angle\theta_{ab} \\ a_bV_aV_b\angle\theta_{ba} & a_bV_b^2 & a_aa_bV_aV_b\angle\theta_{ba} & a_b^2V_b^2 \end{array}\right], \tag{A.15}$$

but the solutions to the SDP will have the form

$$\boldsymbol{W} = \left[\begin{array}{cc|cc} V_a^2 & V_aV_b\angle\theta_{ab} & w_{13} & w_{14} \\ V_aV_b\angle\theta_{ba} & V_b^2 & w_{23} & w_{24} \\ \hline w_{31} & w_{32} & a_a^2V_a^2 & a_aa_bV_aV_b\angle\theta_{\tilde{a}\tilde{b}} \\ w_{41} & w_{42} & a_aa_bV_aV_b\angle\theta_{\tilde{b}\tilde{a}} & a_b^2V_b^2 \end{array}\right], \tag{A.16}$$

where $w_{13} = w_{31}$, $w_{14} = w_{41}^*$, $w_{23} = w_{32}^*$, and $w_{24} = w_{42}$ are unused by the power flow constraints and can vary while still satisfying the PSD condition. The problem in the multi-phase case becomes how to enforce the phase separation when the tap ratios a_a and a_b are unknown; i.e., the issue is how to relate the color coded terms in (A.15) and (A.16). There are two possibilities:

(i) We can reconnect the network so that $\theta_a \approx \tilde{\theta}_a$ and $\theta_b \approx \tilde{\theta}_b$, which allows us to enforce $\theta_a - \theta_b \approx \tilde{\theta}_a - \tilde{\theta}_b$. This is the approach that we proposed in Chapter 3 with the non-ideal transformer model.

(ii) We can include the tap ratios as optimization variables and define the necessary constraints. Unfortunately, the optimization problem would involve product of variables, which results in nonlinearities in the constraints. With this approach, the rank relaxation no longer suffices to obtain a convex problem. Similarly, our constraints will be nonlinear if we include the tap ratios indirectly as a function of $\boldsymbol{W}$.

A.2.3 Numerical Example

We decided to omit the single-phase numerical results for brevity; however, by using the ideal transformer constraints in (A.7a)–(A.7d) and running a second simulation for the constraints in (A.8a)-(A.8c), we get a rank-2 matrix and can recover the same solution obtained with the non-ideal TCUL transformer model in the single-phase case.

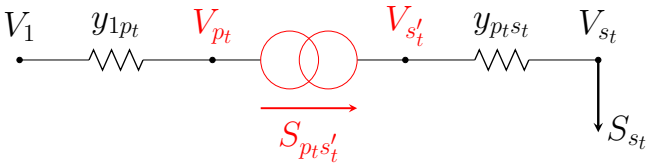

Figure A.1: 2-bus network with an ideal TCUL transformer.

Figure A.1 shows a 4-bus, two-phase, network we use for our numerical example. It contains a single TCUL transformer that we hold the tap ratio at $a = a_a = a_b = 1$ so that we can easily compare the results (i.e., we turn (A.8a) into an equality constraint). The system parameters for the two-phase case are given by

$$\boldsymbol{V}_1 = \begin{bmatrix} 1\angle 0 \\ 1\angle -120^\circ \end{bmatrix} \text{ and } \boldsymbol{S}_{s_t} = \begin{bmatrix} 2.35 + j1.90 \\ 1.17 + j0.68 \end{bmatrix}$$

and

$$\boldsymbol{z}_{1p_t} = \boldsymbol{z}_{p_t s_t} = \begin{bmatrix} 0.0012 + j0.0089 & 0.0003 + j0.0011 \\ 0.0003 + j0.0011i & 0.0012 + j0.0090 \end{bmatrix} \text{ and } \boldsymbol{z}_t = 0.1 \times \boldsymbol{I}_2.$$

First, we run the SDP OPF with the ideal TCUL transformer model from Fig. 1(b) in the manuscript with the constraints in (A.8a)–(A.8c). The solver returns a solution with a rank of 2. Specifically, the submatrix associated with the transformer is

$$\boldsymbol{W}_{p_t s'_t} = \left[\begin{array}{cc|cc} 0.96 & \text{-}0.48 + j0.85 & \text{5e-4} & \text{-3e-4} + j\text{5e-4} \\ \text{-}0.48 - j0.85 & 0.99 & \text{-3e-4} - j\text{5e-4} & \text{6e-4} \\ \hline \text{5e-4} & \text{-3e-4} + j\text{5e-4} & 0.96 & \text{-}0.96 - j0.17 \\ \text{-3e-4} - j\text{5e-4} & \text{6e-4} & \text{-}0.96 + j0.17 & 0.99 \end{array}\right],$$

which matches the phase orientation of (A.14). The angles of the entries will be

$$\angle\boldsymbol{W}_{p_t s'_t} = \left[\begin{array}{cc|cc} 0 & 119.64^\circ & 0 & 119.64^\circ \\ -119.64^\circ & 0 & -119.66^\circ & 0 \\ \hline 0 & 119.66^\circ & 0 & -170.14^\circ \\ -119.64^\circ & 0 & 170.14^\circ & 0 \end{array}\right],$$

and the entry-wise magnitudes are

$$|\boldsymbol{W}_{p_t s'_t}| = \left[\begin{array}{cc|cc} 0.96 & 0.97 & \text{5e-4} & \text{5e-4} \\ 0.97 & 0.99 & \text{5e-4} & \text{6e-4} \\ \hline \text{5e-4} & \text{5e-4} & 0.96 & 0.97 \\ \text{5e-4} & \text{6e-4} & 0.97 & 0.99 \end{array}\right].$$

We divide $\boldsymbol{W}_{p_t s'_t}$ into quadrants such that

$$\boldsymbol{W}_{p_t s'_t} = \left[\begin{array}{c|c} \boldsymbol{W}_{pp} & \boldsymbol{W}_{ps'} \\ \hline \boldsymbol{W}_{s'p} & \boldsymbol{W}_{s's'} \end{array}\right]. \tag{A.17}$$

The intuition from the discussion earlier pertaining to (A.15) and (A.16) above is verified by the numerical results presented in this example. The off-diagonals $\boldsymbol{W}_{ps'}$ and $\boldsymbol{W}_{s'p}$ are irrelevant for the power flow constraints, and the magnitudes reflect this with the phase constraints enforced accordingly. The problem is that $\boldsymbol{W}_{s's'}$, which acts as the reference for the downstream partition of buses $\{s'_t, s_t\}$, is incorrect. The off-diagonals of $\boldsymbol{W}_{s's'}$ should be

$$[\boldsymbol{W}_{s's'}]_{12} = [\boldsymbol{W}_{s's'}]^*_{21} = \left(\sqrt{0.96} \times \sqrt{0.99}\right) \angle 119.64^\circ = 0.97 \angle 119.64^\circ.$$

While the magnitude is correct, the relative phase difference between phases

A and B on the secondary side of the transformer are not; and we can cannot recover the correct solution.

Next, we perform the same simulation with the non-ideal TCUL transformer. The optimization returns a rank-1 matrix and we find (using the notation in (A.14)) that

$$\theta_a = -1.001^\circ,\ \theta_b = -120.65^\circ,\ \tilde{\theta}_a = -1.00^\circ,\ \tilde{\theta}_b = -120.65^\circ,$$

with all of the correct magnitudes. The connected network also enforces the correct values for $\boldsymbol{W}_{ps'}$ and $\boldsymbol{W}_{s'p}$ since z_t couples the power flow constraints between the two partitions.

APPENDIX B

LINEAR REFORMULATION OF THE OPF FOR THE CONVEX SOLVER

This appendix provides the necessary derivation to formulate the linear problem with SOCP and SDP constraints for the optimizations in Chapters 3 and 5 to implement the SeDuMi solver.

B.1 Linear Reformulation

We would like to hardcode a variant of the relax SDP OPF developed in Chapter 3. Consider the minimization problem

$$\min_{W \succeq \mathbf{0},\, q,\, S_{ps'}} \sum_{(i,k)\in\mathcal{E}} \mathrm{Re}\left\{\mathrm{Tr}\left(A_{ik}W\right)\right\} + \sum_{i\in\mathcal{N}} w_i \left([W]_{ii} - (V_i^r)^2\right)^2 \tag{B.1a}$$

such that

$$\mathrm{Tr}\left(H_i W\right) - S_i - jq_i = 0, \qquad \forall i \in \mathcal{N}\backslash\mathcal{N}_p \tag{B.1b}$$

$$\mathrm{Tr}\left(H_{p_t} W\right) - S_{p_t} + S_{p_t s'_t} - jq_i = 0, \qquad \forall t \in \mathcal{T} \tag{B.1c}$$

$$\mathrm{Tr}\left(H_{s'_t} W\right) - S_{p_t s'_t} = 0, \qquad \forall t \in \mathcal{T} \tag{B.1d}$$

and

$$\underline{V}^2 \leq \ [W]_{ii} \ \leq \overline{V}^2, \qquad \forall i \in \mathcal{N} \tag{B.1e}$$

$$\underline{a}^2 [W]_{p_t p_t} \leq [W]_{s'_t s'_t} \leq \overline{a}^2 [W]_{p_t p_t}, \qquad \forall t \in \mathcal{T} \tag{B.1f}$$

$$\underline{q}_i \leq \quad q_i \quad \leq \overline{q}_i, \qquad \forall i \in \mathcal{N} \tag{B.1g}$$

where $w_i \geq 0$ is a weight associated with the voltage regulation. The current representation presents a couple problems. First, the matrices defined here are complex and we want to operate in the real domain. Second, the solver

requires the problem to be posed in the form

$$\min_x c^{\mathrm{T}} x$$

such that

$$Ax = b$$

$$x \in \mathbb{R}^n \text{ or } x \geq 0$$

for $A \in \mathbb{R}^{m \times n}$, $b \in \mathbb{R}^m$, and $c \in \mathbb{R}^n$. Finally, the solvers require the problem to be linear, which the objective function clearly is not. We can linearize by introducing new optimization variables and leverage Schur's complement; however, SeDuMi provides functions to handle (Rotated) Lorentz (quadratic, second-order cone) constraints to handle this for us [61]. We will address this in the next section.

B.1.1 Power Flow Equations

We motivate the formulation of the power flow constraints with a two bus example represented in rectangular coordinates.

Example 3 (Two Bus Example) *Consider a system that contains two buses and a transmission line. Then, it follows from our definitions in Chapter 3 that*

$$\begin{aligned}\mathrm{Tr}(H_1 W) &= \mathrm{Tr}\left(\begin{bmatrix} Y_{11}^* & 0 \\ Y_{12}^* & 0 \end{bmatrix} \begin{bmatrix} |V_1|^2 & V_1 V_2^* \\ V_1^* V_2 & |V_2|^2 \end{bmatrix}\right) \\ &= Y_{11}^* |V_1|^2 + Y_{12}^* V_1 V_2^*,\end{aligned}$$

where $y_{ik} = g_{ik} + j b_{ik}$ for the distribution line segment $(i,k) \in \mathcal{E}$. We would would like to reformulate the problem where

$$\tilde{V} = \begin{bmatrix} e_1 \\ e_2 \\ f_1 \\ f_2 \end{bmatrix} \quad \textit{and} \quad \tilde{W} = \tilde{V}\tilde{V}^{\mathrm{T}} = \begin{bmatrix} e_1^2 & e_1 e_2 & e_1 f_1 & e_1 f_2 \\ e_1 e_2 & e_2^2 & e_2 f_1 & e_2 f_2 \\ e_1 f_1 & e_2 f_1 & f_1^2 & f_1 f_2 \\ e_1 f_2 & e_2 f_2 & f_1 f_2 & f_2^2 \end{bmatrix}.$$

The active power flow at bus 1 in rectangular coordinates will be

$$P_1 = g_{11}\left(e_1^2 + f_1^2\right) + g_{12}\left(e_1 e_2 + f_1 f_2\right) + b_{12}\left(e_2 f_1 - e_1 f_2\right), \tag{B.2}$$

and similarly for the reactive power

$$Q_1 = -b_{11}\left(e_1^2 + f_1^2\right) + g_{12}\left(e_2 f_1 - e_1 f_2\right) - b_{12}\left(e_1 e_2 + f_1 f_2\right). \tag{B.3}$$

We can rewrite (B.2) *as*

$$\begin{aligned} P_1 &= Tr\left(\tilde{H}_1 \tilde{W}\right) \\ &= \mathrm{Tr}\left(\begin{bmatrix} g_{11} & 0 & b_{11} & 0 \\ g_{12} & 0 & b_{12} & 0 \\ -b_{11} & 0 & g_{11} & 0 \\ -b_{12} & 0 & g_{12} & 0 \end{bmatrix} \tilde{W}\right) \\ &= \mathrm{Tr}\left(\begin{bmatrix} \mathrm{Re}\{H_1\} & -\mathrm{Im}\{H_1\} \\ \mathrm{Im}\{H_1\} & \mathrm{Re}\{H_1\} \end{bmatrix} \tilde{W}\right), \end{aligned}$$

and similarly for the reactive power

$$\begin{aligned} Q_1 &= \mathrm{Tr}\left(M_1 \tilde{W}\right) \\ &= \mathrm{Tr}\left(\begin{bmatrix} \mathrm{Im}\{H_1\} & \mathrm{Re}\{H_1\} \\ -\mathrm{Re}\{H_1\} & \mathrm{Im}\{H_1\} \end{bmatrix} \tilde{W}\right); \end{aligned}$$

this concludes the example.

■

Following Example 3, we can remove complex numbers by defining our matrices as follows:

$$\tilde{V} = \begin{bmatrix} \mathrm{Re}\{V\} \\ \mathrm{Im}\{V\} \end{bmatrix}, \tag{B.4}$$

$$\tilde{W} = \tilde{V}\tilde{V}^{\mathrm{T}}, \tag{B.5}$$

$$\tilde{H}_i = \begin{bmatrix} \mathrm{Re}\{H_i\} & -\mathrm{Im}\{H_i\} \\ \mathrm{Im}\{H_i\} & \mathrm{Re}\{H_i\} \end{bmatrix}, \tag{B.6}$$

$$M_i = \begin{bmatrix} \mathrm{Im}\{H_i\} & \mathrm{Re}\{H_i\} \\ -\mathrm{Re}\{H_i\} & \mathrm{Im}\{H_i\} \end{bmatrix}, \tag{B.7}$$

$$\tilde{A}_{ik} = \begin{bmatrix} \mathrm{Re}\{A_{ik}\} & -\mathrm{Im}\{A_{ik}\} \\ \mathrm{Im}\{A_{ik}\} & \mathrm{Re}\{A_{ik}\} \end{bmatrix}. \tag{B.8}$$

B.1.2 Inequality Constraints

SeDuMi requires the uses an equality constraint where the optimization variables are either free (unsigned) or nonnegative. Consider the inequality constraint

$$a \leq x \leq b,$$

where $x \in \mathbb{R}$ is a free variable. We can rewrite this expression as

$$\begin{aligned} a - x + s_1 &= 0, \\ -b + x + s_2 &= 0, \end{aligned}$$

where $s_1, s_2 \geq 0$ are nonnegative slack variables.

B.1.3 Equivalent Problem

Albeit a slight abuse of notation, i.e., we refer to $\tilde{W}$ as W, etc., we incorporate all the changes discussed above and the equivalent problem for SeDuMi is

$$\min_{W \succeq \mathbf{0},\, q,\, S_{ps'}} \sum_{(i,k)\in\mathcal{E}} \mathrm{Tr}\left(A_{ik}W\right) + \sum_{i\in\mathcal{N}} w_i \left| [W]_{ii} + [W]_{\widetilde{i}\widetilde{i}} - (V_i^r)^2 \right|^2 \tag{B.9a}$$

such that

$$\begin{aligned}
\operatorname{Tr}(H_i W) - P_i &= 0, && \forall i \in \mathcal{N} \backslash \mathcal{N}_p && \text{(B.9b)}\\
\operatorname{Tr}(M_i W) - Q_i &= 0, && \forall i \in \mathcal{N} \backslash \mathcal{N}_p && \text{(B.9c)}\\
\operatorname{Tr}(H_{p_t} W) - P_{p_t} + P_{p_t s'_t} &= 0, && \forall t \in \mathcal{T} && \text{(B.9d)}\\
\operatorname{Tr}(M_{p_t} W) - Q_{p_t} + Q_{p_t s'_t} &= 0, && \forall t \in \mathcal{T} && \text{(B.9e)}\\
\operatorname{Tr}\left(H_{s'_t} W\right) - P_{p_t s'_t} &= 0, && \forall t \in \mathcal{T} && \text{(B.9f)}\\
\operatorname{Tr}\left(M_{s'_t} W\right) - Q_{p_t s'_t} &= 0, && \forall t \in \mathcal{T} && \text{(B.9g)}
\end{aligned}$$

and

$$\begin{aligned}
\underline{V}^2 - [W]_{ii} - [W]_{\tilde{i}\tilde{i}} + l_i &= 0, \quad \forall i \in \mathcal{N} && \text{(B.9h)}\\
-\overline{V}^2 + [W]_{ii} + [W]_{\tilde{i}\tilde{i}} + u_i &= 0, \quad \forall i \in \mathcal{N} && \text{(B.9i)}\\
\underline{a}^2 \left([W]_{p_t p_t} + [W]_{\tilde{p}_t \tilde{p}_t}\right) - [W]_{s'_t s'_t} - [W]_{\tilde{s}'_t \tilde{s}'_t} + l_t &= 0, \quad \forall t \in \mathcal{T} && \text{(B.9j)}\\
-\overline{a}^2 \left([W]_{p_t p_t} + [W]_{\tilde{p}_t \tilde{p}_t}\right) + [W]_{s'_t s'_t} + [W]_{\tilde{s}'_t \tilde{s}'_t} + u_t &= 0, \quad \forall t \in \mathcal{T} && \text{(B.9k)}\\
\overline{q}_i - q_i + \tilde{l}_i &= 0, \quad \forall i \in \mathcal{N} && \text{(B.9l)}\\
-\overline{q}_i + q_i + \tilde{u}_i &= 0, \quad \forall i \in \mathcal{N}, && \text{(B.9m)}
\end{aligned}$$

and

$$l_i \geq 0, \quad u_i \geq 0, \quad \tilde{l}_i \geq 0, \quad \tilde{u}_i \geq 0, \quad \forall i, \qquad \text{(B.9n)}$$

where $\tilde{i}, \tilde{p}_t, \tilde{s}'_t$ are the entries in the lower block diagonal entries of W corresponding to the imaginary components.

B.2 SeDuMi Remarks

In this section, we provide a few useful tips on how to solve (B.9) with SeDuMi. The constraints in (B.9b)–(B.9n) are linear and straight forward to implement.

B.2.1 Trace Operational Equivalent

In Matlab we can convert a matrix to a vector with the **`vec(x)`**. Similarly, we can return to a matrix with the command **`mat(x)`**. For example

$$\mathbf{vec}\left(\begin{bmatrix} 1 & 3 \\ 2 & 4 \end{bmatrix}\right) = \begin{bmatrix} 1 \\ 2 \\ 3 \\ 4 \end{bmatrix} \quad \text{and} \quad \mathbf{mat}\left(\begin{bmatrix} 1 \\ 2 \\ 3 \\ 4 \end{bmatrix}\right) = \begin{bmatrix} 1 & 3 \\ 2 & 4 \end{bmatrix}.$$

Thus, the following expressions are equivalent

$$\mathrm{Tr}\left(H_i W\right) = \mathbf{vec}\left(H_i^{\mathrm{T}}\right)^{\mathrm{T}} \mathbf{vec}\left(W\right).$$

B.2.2 Rotated Lorentz Constraint

In SeDuMi we can leverage second-order cone program (SOCP) to handle both the boundary constraints in the distributed solver (e.g., see Chapters 3 and 5) and the voltage regulation penalty term in (B.9a). The rotated Lorentz constraint has the following form:

$$2x_1x_2 \geq \|y\|_2^2,$$

for $x_1, x_2 \in \mathbb{R}$ and $y \in \mathbb{R}^n$. Thus, the voltage regulation component of (B.9a) will be

$$\min x_1 \tag{B.10a}$$

such that

$$2x_1x_2 \geq \|y\|_2^2 \tag{B.10b}$$

$$x_2 = 0.5 \tag{B.10c}$$

$$y_i = \sqrt{w_i}\left([W]_{ii} + [W]_{\bar{i}\bar{i}} - (V_i^r)^2\right), \quad \forall i \in \mathcal{N}. \tag{B.10d}$$

APPENDIX C

TWO-STAGE VOLTAGE REGULATION

In this appendix, we provide additional support for two key results in Chapter 4, as well as the system data for the 8-bus example.

C.1 Stage One Stability Analysis

Consider the system in (4.7); in order to ensure its stability, we need to ensure that $|\sigma_i(I - \alpha SD)| < 1,\ \forall i$, where $\sigma_i(I - \alpha SD)$ denotes the i^{th} eigenvalue of $I - \alpha SD$. Let $\lambda_i = \mathrm{Re}\{\lambda_i\} + j\,\mathrm{Im}\{\lambda_i\}$ denote the i^{th} eigenvalue of the matrix SD. Then, it follows that every $\sigma_i(I-\alpha SD)$ is given by $\sigma_i = 1-\alpha\lambda_i$. Therefore, $\sigma_i = (1-\alpha\,\mathrm{Re}\{\lambda_i\})+j\alpha\,\mathrm{Im}\{\lambda_i\}$, and $|\sigma_i|^2 = 1-2\alpha\,\mathrm{Re}\{\lambda_i\}+\alpha^2|\lambda_i|^2$. Then, $|\sigma_i|^2 < 1$, if $\alpha < 2\,\mathrm{Re}\{\lambda_i\}/|\lambda_i|^2$. Thus, $|\sigma_i(I - \alpha SD)| < 1,\ \forall i$, if $\alpha < \alpha_c = \min_i \left\{ \frac{2\,\mathrm{Re}\{\lambda_i\}}{|\lambda_i|^2} \right\}$.

C.2 Stage Two Convergence Analysis

Let $\mu[k] = [\mu_1[k], \mu_2[k], \ldots, \mu_n[k]]^T$, $\overline{\nu}[k] = [\overline{\nu}_1[k], \overline{\nu}_2[k], \ldots, \overline{\nu}_n[k]]^T$, and $\underline{\nu}[k] = [\underline{\nu}_1[k], \underline{\nu}_2[k], \ldots, \underline{\nu}_n[k]]^T$. Then the iterations in (4.10)—(4.12) can be rewritten in matrix form as

$$\mu[k+1] = P\mu[k], \tag{C.1}$$

$$\overline{\nu}[k+1] = P\overline{\nu}[k], \tag{C.2}$$

$$\underline{\nu}[k+1] = P\underline{\nu}[k], \tag{C.3}$$

where $P \in \mathbb{R}^{n\times n}$ is a primitive column stochastic matrix. Primitivity follows since P is (i) a nonnegative matrix, (ii) the assumption that the graph of P is strongly connected implies that P is irreducible, and (iii) P is aperiodic since it contains at least one $p_{jj} > 0$ [65]. This ensures that (C.1)–(C.3)

converge to the unique solutions $\mu = \lim_{k\to\infty} \mu[k] = (\sum_{i=1}^{n} \mu_i[0])\pi$, $\overline{\nu} = \lim_{k\to\infty} \overline{\nu}[k] = (\sum_{i=1}^{n} \overline{\nu}_i[0])\pi$, and $\underline{\nu} = \lim_{k\to\infty} \underline{\nu}[k] = (\sum_{i=1}^{n} \underline{\nu}_i[0])\pi$, where $\pi = [\pi_1, \pi_2, \ldots, \pi_n]^T$ is the unique solution of $\pi = P\pi$ satisfying $\sum_{i=1}^{n} \pi_i = 1$, and $\pi_i > 0$, $\forall i$, (see, e.g., [65]). If $\sum_{i=1}^{n} \mu_i[0] \geq 0$, then $\lim_{k\to\infty} \mu_j[k] \geq 0$ $\forall j$, and therefore

$$\lim_{k\to\infty} \frac{\mu_j[k]}{\overline{\nu}_k[k]} = \frac{\sum_{i=1}^{n} \mu_i[0]}{\sum_{i=1}^{n} \overline{\nu}_i[0]}, \tag{C.4}$$

from which it follows that

$$\eta_j = \lim_{k\to\infty} \eta_j[k] = \frac{\sum_{i=1}^{n} \mu_i[0]}{\sum_{i=1}^{n} \overline{\nu}_i[0]} \overline{\nu}_j[0], \ \forall j. \tag{C.5}$$

A similar reasoning can be used to establish that, whenever $\sum_{i=1}^{n} \mu_i[0] \leq 0$, $\eta_j = (\sum_{i=1}^{n} \mu_i[0] / \sum_{i=1}^{n} \underline{\nu}_i[0])\underline{\nu}_j[0]$, $\forall j$.

C.3 Data for 8-bus System Example

For the topology shown in Fig. 4.3(a), the transition matrix P that results from the set of weights that define the distributed algorithm is given

$$P = \begin{bmatrix} 1/2 & 1/3 & 0 & 0 & 0 & 0 & 0 \\ 1/2 & 1/3 & 1/4 & 0 & 0 & 0 & 0 \\ 0 & 1/3 & 1/4 & 1/3 & 0 & 1/3 & 0 \\ 0 & 0 & 1/4 & 1/3 & 1/2 & 0 & 0 \\ 0 & 0 & 0 & 1/3 & 1/2 & 0 & 0 \\ 0 & 0 & 1/4 & 0 & 0 & 1/3 & 1/2 \\ 0 & 0 & 0 & 0 & 0 & 1/3 & 1/2 \end{bmatrix}, \tag{C.6}$$

whereas for the topology shown in Fig. 4.3(b) is given by

$$P = \begin{bmatrix} 1/3 & 0 & 0 & 0 & 0 & 0 & 1/4 \\ 1/3 & 1/2 & 1/4 & 0 & 0 & 0 & 0 \\ 0 & 1/2 & 1/4 & 1/3 & 0 & 1/3 & 0 \\ 0 & 0 & 1/4 & 1/3 & 0 & 0 & 0 \\ 0 & 0 & 0 & 1/3 & 1/2 & 0 & 1/4 \\ 0 & 0 & 1/4 & 0 & 0 & 1/3 & 1/4 \\ 1/3 & 0 & 0 & 0 & 1/2 & 1/3 & 1/4 \end{bmatrix}. \tag{C.7}$$

The load and DER capacity data for the example in Section 4.4 are listed in Table C.1. Note that the capacities are denoted by *under* and *over* for the under-voltage and over-voltage examples, respectively. Line parameters are listed in Table C.2.

Table C.1: 8-Bus Load Data

Bus	P_L	Q_L	$\overline{q}^{over}$	$\underline{q}^{over}$	$\overline{q}^{under}$	$\underline{q}^{under}$
1	0.70	0.10	1.000	-1.000	0.20	-0.20
2	0.85	0.25	0.7 00	-0.700	0.20	-0.20
3	0.60	0.15	0.625	-0.625	0.30	-0.20
4	1.25	0.50	0.500	-0.500	0.50	-0.50
5	0.90	0.30	0.425	-0.425	0.35	-0.35
6	0.10	0.10	0.650	-0.650	0.40	-0.40
7	1.00	0.35	0.625	-0.625	0.20	-0.20

Table C.2: 8-Bus Distribution Line Segment Data

From Bus	To Bus	R [p.u.]	X [p.u.]	B [p.u.]
1	2	0.0010	0.0077	0.0158
2	3	0.0029	0.0145	0.0275
3	4	0.0015	0.0083	0.0142
4	5	0.0035	0.0153	0.0322
3	6	0.0015	0.0065	0.0134
6	7	0.0011	0.0091	0.0188

APPENDIX D

LINEARIZATION OF THE FAST TIME-SCALE OPTIMIZATION

This appendix provides the derivation of the linear approximation of the nonlinear elements of the unbalanced three-phase optimization problem formulated in Section 5.3.2.

D.1 Bus Voltage Approximation

First, we define to $\boldsymbol{a}_i \in \mathbb{C}^3$ represent the element-wise inverse voltage of bus i. We can use two approaches to approximate $\boldsymbol{a}_i$ in the unbalanced three-phase case, (i) treat $\boldsymbol{a}_i$ as a constant, which is similar to the approach we took in Section 5.3.2, or (ii) we sample the bus voltages when we update the power flow constraints for the next optimization. Thus, we can approximate $\boldsymbol{a}_i$ as

$$\boldsymbol{a}_i = \begin{bmatrix} 1 & e^{j2\pi/3} & e^{-j2\pi/3} \end{bmatrix}^{\mathrm{T}} \oslash \boldsymbol{V}_i^r,$$

which will result in the equality constraints having the form $Ax(t) = b(t)$, where t is a time dependence; otherwise, we can choose $\boldsymbol{a}_i$ to be

$$\boldsymbol{a}_i(t) = \mathbf{1} \oslash \boldsymbol{V}_i(t),$$

which gives us equality constraints that the form $A(t)x(t) = b(t)$. The advantage of (i) is that it is fairly accurate and we compute the coefficient matrix A once.

D.2 Nonlinear Voltage Drop Term

In Section 5.3.2, the nonlinear term in the voltage drop equation is

$$\boldsymbol{c}_{ik}^{v}\left(\boldsymbol{P}_{ik},\boldsymbol{Q}_{ik}\right)=\left[\boldsymbol{z}_{ik}\left(\left(\boldsymbol{P}_{ik}-j\boldsymbol{Q}_{ik}\right)\odot\boldsymbol{a}_{i}^{*}\right)\right]\odot\left[\boldsymbol{z}_{ik}^{*}\left(\left(\boldsymbol{P}_{ik}+j\boldsymbol{Q}_{ik}\right)\odot\boldsymbol{a}_{i}\right)\right]. \quad \text{(D.1)}$$

Let the updated distribution line segment impedance be

$$\bar{\boldsymbol{z}}_{ik}=\boldsymbol{z}_{ik}\,\mathrm{diag}\left(\boldsymbol{a}_{i}^{*}\right)=\bar{\boldsymbol{r}}_{ik}+j\bar{\boldsymbol{x}}_{ik}. \quad \text{(D.2)}$$

Then, (D.1) will become

$$\begin{aligned}\boldsymbol{c}_{ik}^{v}\left(\boldsymbol{P}_{ik},\boldsymbol{Q}_{ik}\right)=&\left[\bar{\boldsymbol{r}}_{ik}\boldsymbol{P}_{ik}\right]\odot\left[\bar{\boldsymbol{r}}_{ik}\boldsymbol{P}_{ik}\right]+\left[\bar{\boldsymbol{x}}_{ik}\boldsymbol{Q}_{ik}\right]\odot\left[\bar{\boldsymbol{x}}_{ik}\boldsymbol{Q}_{ik}\right]\\&+\left[\bar{\boldsymbol{x}}_{ik}\boldsymbol{P}_{ik}\right]\odot\left[\bar{\boldsymbol{x}}_{ik}\boldsymbol{P}_{ik}\right]+\left[\bar{\boldsymbol{r}}_{ik}\boldsymbol{Q}_{ik}\right]\odot\left[\bar{\boldsymbol{r}}_{ik}\boldsymbol{Q}_{ik}\right]\\&+2\left[\bar{\boldsymbol{r}}_{ik}\boldsymbol{P}_{ik}\right]\odot\left[\bar{\boldsymbol{x}}_{ik}\boldsymbol{Q}_{ik}\right]-2\left[\bar{\boldsymbol{x}}_{ik}\boldsymbol{P}_{ik}\right]\odot\left[\bar{\boldsymbol{r}}_{ik}\boldsymbol{Q}_{ik}\right].\end{aligned} \quad \text{(D.3)}$$

We can approximate the curve linearly around the point $\left(\boldsymbol{P}_{ik_o},\boldsymbol{Q}_{ik_o}\right)$ as

$$\begin{aligned}\boldsymbol{c}_{ik}^{v}\left(\boldsymbol{P}_{ik_o},\boldsymbol{Q}_{ik_o}\right)\approx&\ f_p\left(\boldsymbol{P}_{ik_o},\boldsymbol{Q}_{ik_o}\right)\left[\boldsymbol{P}_{ik}-\boldsymbol{P}_{ik_o}\right]+\\&f_q\left(\boldsymbol{P}_{ik_o},\boldsymbol{Q}_{ik_o}\right)\left[\boldsymbol{Q}_{ik}-\boldsymbol{Q}_{ik_o}\right]+\boldsymbol{c}_{ik}^{v}\left(\boldsymbol{P}_{ik_o},\boldsymbol{Q}_{ik_o}\right),\end{aligned} \quad \text{(D.4)}$$

where the partial derivatives are

$$\begin{aligned}f_p=\frac{\partial\boldsymbol{c}_{ik}^{v}}{\partial\boldsymbol{P}_{ik}}=&\ h_{xx}\left(\bar{\boldsymbol{r}}_{ik},\boldsymbol{P}_{ik}\right)+h_{xx}\left(\bar{\boldsymbol{x}}_{ik},\boldsymbol{P}_{ik}\right)\\&+2h_{xy}\left(\bar{\boldsymbol{r}}_{ik},\bar{\boldsymbol{x}}_{ik},\boldsymbol{P}_{ik},\boldsymbol{Q}_{ik}\right)-2h_{xy}\left(\bar{\boldsymbol{x}}_{ik},\bar{\boldsymbol{r}}_{ik},\boldsymbol{P}_{ik},\boldsymbol{Q}_{ik}\right),\\f_q=\frac{\partial\boldsymbol{c}_{ik}^{v}}{\partial\boldsymbol{Q}_{ik}}=&\ h_{xx}\left(\bar{\boldsymbol{r}}_{ik},\boldsymbol{Q}_{ik}\right)+h_{xx}\left(\bar{\boldsymbol{x}}_{ik},\boldsymbol{Q}_{ik}\right)\\&+2h_{xy}\left(\bar{\boldsymbol{x}}_{ik},\bar{\boldsymbol{r}}_{ik},\boldsymbol{Q}_{ik},\boldsymbol{P}_{ik}\right)-2h_{xy}\left(\bar{\boldsymbol{r}}_{ik},\bar{\boldsymbol{x}}_{ik},\boldsymbol{Q}_{ik},\boldsymbol{P}_{ik}\right),\end{aligned}$$

and

$$\begin{aligned}h_{xx}\left(\boldsymbol{A},\boldsymbol{x}\right)&=2\boldsymbol{A}\,\mathrm{diag}\left(\boldsymbol{A}\boldsymbol{x}\right),\\h_{xy}\left(\boldsymbol{A},\boldsymbol{B},\boldsymbol{x},\boldsymbol{y}\right)&=\boldsymbol{A}\,\mathrm{diag}\left(\boldsymbol{B}\boldsymbol{y}\right).\end{aligned}$$

D.3 Nonlinear Power Loss Terms

The loss power across the distribution line segment $(i,k) \in \mathcal{E}$ is given by

$$\boldsymbol{S}_{ik}^{\ell} = [\boldsymbol{S}_{ik} \oslash \boldsymbol{V}_i] \odot [\boldsymbol{z}_{ik} (\boldsymbol{S}_{ik}^{*} \oslash \boldsymbol{V}_i^{*})], \tag{D.5}$$

where we follow the same notation as Section 5.3.2. We update the distribution line segment impedance to be

$$\tilde{\boldsymbol{z}}_{ik} = \tilde{\boldsymbol{r}}_{ik} + j\tilde{\boldsymbol{x}}_{ik} = \boldsymbol{z}_{ik} \odot \left(\boldsymbol{a}_i \boldsymbol{a}_i^{\mathrm{H}}\right), \tag{D.6}$$

such that

$$\tilde{\boldsymbol{r}}_{ik} = \mathrm{Re}\left\{\boldsymbol{a}_i \boldsymbol{a}_i^{\mathrm{H}}\right\} \odot \boldsymbol{r}_{ik} - \mathrm{Im}\left\{\boldsymbol{a}_i \boldsymbol{a}_i^{\mathrm{H}}\right\} \odot \boldsymbol{x}_{ik}, \tag{D.7}$$

$$\tilde{\boldsymbol{x}}_{ik} = \mathrm{Re}\left\{\boldsymbol{a}_i \boldsymbol{a}_i^{\mathrm{H}}\right\} \odot \boldsymbol{x}_{ik} + \mathrm{Im}\left\{\boldsymbol{a}_i \boldsymbol{a}_i^{\mathrm{H}}\right\} \odot \boldsymbol{r}_{ik}. \tag{D.8}$$

Thus, we can rewrite (D.5) as

$$\boldsymbol{S}_{ik}^{\ell} = [\boldsymbol{P}_{ik} + j\boldsymbol{Q}_{ik}] \odot [\tilde{\boldsymbol{z}}_{ik} (\boldsymbol{P}_{ik} - j\boldsymbol{Q}_{ik})], \tag{D.9}$$

where we separate the active and reactive power losses along the distribution line segment to compute the nonlinear power loss terms

$$\boldsymbol{c}_{ik}^{p} (\boldsymbol{P}_{ik}, \boldsymbol{Q}_{ik}) = \boldsymbol{P}_{ik} \odot [\tilde{\boldsymbol{r}}_{ik} \boldsymbol{P}_{ik} + \tilde{\boldsymbol{x}}_{ik} \boldsymbol{Q}_{ik}] + \boldsymbol{Q}_{ik} \odot [\tilde{\boldsymbol{r}}_{ik} \boldsymbol{Q}_{ik} - \tilde{\boldsymbol{x}}_{ik} \boldsymbol{P}_{ik}], \tag{D.10}$$

and

$$\boldsymbol{c}_{ik}^{q} (\boldsymbol{P}_{ik}, \boldsymbol{Q}_{ik}) = \boldsymbol{P}_{ik} \odot [\tilde{\boldsymbol{x}}_{ik} \boldsymbol{P}_{ik} - \tilde{\boldsymbol{r}}_{ik} \boldsymbol{Q}_{ik}] + \boldsymbol{Q}_{ik} \odot [\tilde{\boldsymbol{r}}_{ik} \boldsymbol{P}_{ik} + \tilde{\boldsymbol{x}}_{ik} \boldsymbol{Q}_{ik}], \tag{D.11}$$

respectively. The linear approximate of (D.10) and (D.11) will be

$$\begin{aligned} \boldsymbol{c}_{ik}^{p} \left(\boldsymbol{P}_{ik_o}, \boldsymbol{Q}_{ik_o}\right) \approx\ & f_p \left(\boldsymbol{P}_{ik_o}, \boldsymbol{Q}_{ik_o}\right) \left[\boldsymbol{P}_{ik} - \boldsymbol{P}_{ik_o}\right] + \\ & f_q \left(\boldsymbol{P}_{ik_o}, \boldsymbol{Q}_{ik_o}\right) \left[\boldsymbol{Q}_{ik} - \boldsymbol{Q}_{ik_o}\right] + \boldsymbol{c}_{ik}^{p} \left(\boldsymbol{P}_{ik_o}, \boldsymbol{Q}_{ik_o}\right) \end{aligned} \tag{D.12}$$

and

$$\begin{aligned} \boldsymbol{c}_{ik}^{q} \left(\boldsymbol{P}_{ik_o}, \boldsymbol{Q}_{ik_o}\right) \approx\ & g_p \left(\boldsymbol{P}_{ik_o}, \boldsymbol{Q}_{ik_o}\right) \left[\boldsymbol{P}_{ik} - \boldsymbol{P}_{ik_o}\right] + \\ & g_q \left(\boldsymbol{P}_{ik_o}, \boldsymbol{Q}_{ik_o}\right) \left[\boldsymbol{Q}_{ik} - \boldsymbol{Q}_{ik_o}\right] + \boldsymbol{c}_{ik}^{q} \left(\boldsymbol{P}_{ik_o}, \boldsymbol{Q}_{ik_o}\right), \end{aligned} \tag{D.13}$$

where the partial derivatives are

$$
\begin{aligned}
f_p &= \frac{\partial \boldsymbol{c}_{ik}^p}{\partial \boldsymbol{P}_{ik}} = h_{xx}\left(\tilde{\boldsymbol{r}}_{ik}, \boldsymbol{P}_{ik}\right) + h_{xy}\left(\tilde{\boldsymbol{x}}_{ik}, \boldsymbol{P}_{ik}, \boldsymbol{Q}_{ik}\right) - h_{yx}\left(\tilde{\boldsymbol{x}}_{ik}, \boldsymbol{Q}_{ik}, \boldsymbol{P}_{ik}\right), \\
f_q &= \frac{\partial \boldsymbol{c}_{ik}^p}{\partial \boldsymbol{Q}_{ik}} = h_{xx}\left(\tilde{\boldsymbol{r}}_{ik}, \boldsymbol{Q}_{ik}\right) - h_{xy}\left(\tilde{\boldsymbol{x}}_{ik}, \boldsymbol{Q}_{ik}, \boldsymbol{P}_{ik}\right) + h_{yx}\left(\tilde{\boldsymbol{x}}_{ik}, \boldsymbol{P}_{ik}, \boldsymbol{Q}_{ik}\right), \\
g_p &= \frac{\partial \boldsymbol{c}_{ik}^q}{\partial \boldsymbol{P}_{ik}} = h_{xx}\left(\tilde{\boldsymbol{x}}_{ik}, \boldsymbol{P}_{ik}\right) - h_{xy}\left(\tilde{\boldsymbol{r}}_{ik}, \boldsymbol{P}_{ik}, \boldsymbol{Q}_{ik}\right) + h_{yx}\left(\tilde{\boldsymbol{r}}_{ik}, \boldsymbol{Q}_{ik}, \boldsymbol{P}_{ik}\right), \\
g_q &= \frac{\partial \boldsymbol{c}_{ik}^q}{\partial \boldsymbol{Q}_{ik}} = h_{xx}\left(\tilde{\boldsymbol{x}}_{ik}, \boldsymbol{Q}_{ik}\right) + h_{xy}\left(\tilde{\boldsymbol{r}}_{ik}, \boldsymbol{Q}_{ik}, \boldsymbol{P}_{ik}\right) + h_{yx}\left(\tilde{\boldsymbol{r}}_{ik}, \boldsymbol{P}_{ik}, \boldsymbol{Q}_{ik}\right),
\end{aligned}
$$

and

$$
\begin{aligned}
h_{xx}\left(\boldsymbol{A}, \boldsymbol{x}\right) &= \operatorname{diag}\left(\boldsymbol{A}\boldsymbol{x}\right) + \operatorname{diag}\left(\boldsymbol{x}\right)\boldsymbol{A}, \\
h_{xy}\left(\boldsymbol{A}, \boldsymbol{x}, \boldsymbol{y}\right) &= \operatorname{diag}\left(\boldsymbol{A}\boldsymbol{y}\right), \\
h_{yx}\left(\boldsymbol{A}, \boldsymbol{x}, \boldsymbol{y}\right) &= \operatorname{diag}\left(\boldsymbol{x}\right)\boldsymbol{A}.
\end{aligned}
$$

APPENDIX E

DISTRIBUTION SYSTEM PARAMETER DATA SETS

This appendix lists the system data for the 15-bus and 123-bus systems used throughout this thesis.

E.1 15-Bus Distribution System

The system values are listed in Tables E.1 and E.2, where the base power is 100 kVA. The impedance matrices for the line configurations are the following:

Configuration L601

$$\boldsymbol{Z} = \begin{bmatrix} 0.347+j1.018 & 0.156+j0.502 & 0.158+j0.424 \\ 0.156+j0.502 & 0.338+j1.048 & 0.154+j0.385 \\ 0.158+j0.424 & 0.154+j0.385 & 0.341+j1.035 \end{bmatrix} \ \Omega/\text{mi}$$

$$\boldsymbol{B} = j \begin{bmatrix} 6.3 & -1.996 & -1.259 \\ -1.996 & 5.96 & -0.742 \\ -1.259 & -0.742 & 5.639 \end{bmatrix} \ \mu\text{S/mi}$$

Configuration L602

$$\boldsymbol{Z} = \begin{bmatrix} 0.753+j1.181 & 0.158+j0.424 & 0.156+j0.502 \\ 0.158+j0.424 & 0.748+j1.198 & 0.154+j0.385 \\ 0.156+j0.502 & 0.154+j0.385 & 0.744+j1.211 \end{bmatrix} \ \Omega/\text{mi}$$

$$\boldsymbol{B} = j \begin{bmatrix} 5.699 & -1.082 & -1.691 \\ -1.082 & 5.179 & -0.659 \\ -1.691 & -0.659 & 5.425 \end{bmatrix} \ \mu\text{S/mi}$$

Configuration L603

$$\boldsymbol{Z} = \begin{bmatrix} 0 & 0 & 0 \\ 0 & 1.329+j1.347 & 0.207+j0.459 \\ 0 & 0.207+j0.459 & 1.324+j1.357 \end{bmatrix} \ \Omega/\text{mi}$$

$$\boldsymbol{B} = j \begin{bmatrix} 0 & 0 & 0 \\ 0 & 4.71 & -0.9 \\ 0 & -0.9 & 4.666 \end{bmatrix} \ \mu\text{S/mi}$$

Configuration L604

$$\boldsymbol{Z} = \begin{bmatrix} 1.324{+}j1.357 & 0 & 0.207{+}j0.459 \\ 0 & 0 & 0 \\ 0.207{+}j0.459 & 0 & 1.329{+}j1.347 \end{bmatrix} \ \Omega\text{/mi}$$

$$\boldsymbol{B} = j \begin{bmatrix} 4.666 & 0 & -0.9 \\ 0 & 0 & 0 \\ -0.9 & 0 & 4.71 \end{bmatrix} \ \mu\text{S/mi}$$

Configuration L605

$$\boldsymbol{Z} = \begin{bmatrix} 0 & 0 & 0 \\ 0 & 0 & 0 \\ 0 & 0 & 1.329{+}j1.347 \end{bmatrix} \ \Omega\text{/mi}$$

$$\boldsymbol{B} = j \begin{bmatrix} 0 & 0 & 0 \\ 0 & 0 & 0 \\ 0 & 0 & 4.519 \end{bmatrix} \ \mu\text{S/mi}$$

Configuration L606

$$\boldsymbol{Z} = \begin{bmatrix} 0.7982{+}j0.446 & 0.319{+}j0.033 & 0.285{+}j0.014 \\ 0.3192{+}j0.033 & 0.789{+}j0.404 & 0.319{+}j0.033 \\ 0.2849{+}j0.014 & 0.319{+}j0.033 & 0.798{+}j0.446 \end{bmatrix} \ \Omega\text{/mi}$$

$$\boldsymbol{B} = j \begin{bmatrix} 96.61 & 0 & 0 \\ 0 & 96.61 & 0 \\ 0 & 0 & 96.61 \end{bmatrix} \ \mu\text{S/mi}$$

Configuration L607

$$\boldsymbol{Z} = \begin{bmatrix} 1.343{+}j0.512 & 0 & 0 \\ 0 & 0 & 0 \\ 0 & 0 & 0 \end{bmatrix} \ \Omega\text{/mi}$$

$$\boldsymbol{B} = j \begin{bmatrix} 89.32 & 0 & 0 \\ 0 & 0 & 0 \\ 0 & 0 & 0 \end{bmatrix} \ \mu\text{S/mi}$$

Configuration LXFM1

$$\boldsymbol{Z} = \begin{bmatrix} 0.011{+}j0.02 & 0 & 0 \\ 0 & 0.011{+}j0.02i & 0 \\ 0 & 0 & 0.011{+}j0.02 \end{bmatrix} \text{ p.u.}$$

Table E.1: 15-Bus Load Data

Bus	Phases	V_{ll} [kV]	Cap [kVAr]	Load [kVA]
1	A B C	4.16	0, 0, 0	0, 0, 0
2	B C	4.16	0, 0, 0	0, 170+j125, 0
3	A B C	4.16	0, 0, 0	0, 0, 0
4	A B C	0.48	0, 0, 0	160+j110, 120+j90, 120+j90
5	B C	4.16	0, 0, 0	0, 230+j132, 0
6	A B C	4.16	0, 0, 0	0, 0, 0
7	A C	4.16	0, 0, 0	0, 0, 0
8	A	4.16	0, 0, 0	128+j86, 0, 0
9	A B C	4.16	0, 0, 0	285+j170, 285+j170, 255+j171
10	A B C	4.16	0, 0, 0	0, 0, 0
11	C	4.16	0, 0, 100	0, 0, 170+j80
12	A B C	4.16	200, 200, 200	235+j190, 68+j60, 290+j150
13	A B C	4.16	0, 0, 0	0, 0, 0
14	A B C	4.16	0, 0, 0	0, 0, 0
15	A B C	4.16	0, 0, 0	17+j10, 66+j38, 117+j68

Table E.2: 15-Bus Distribution Line Segment Data

Line	From	To	Length [ft]	Config.
1	1	2	500	L603
2	1	3	500	L602
3	3	4	0	LXFM1
4	2	5	300	L603
5	6	1	2000	L601
6	7	8	800	L607
7	9	7	300	L604
8	9	10	1000	L601
9	7	11	300	L605
10	9	12	500	L606
11	13	6	500	L602
12	14	13	500	L602
13	1	15	667	L601
14	15	9	1333	L601

E.2 123-Bus Distribution System

The system values are listed in Tables E.3 through E.4, where the base power is 100 kVA. The impedance matrices for the line configurations are the following:

Configuration 1

$$\boldsymbol{Z} = \begin{bmatrix} 0.458+j1.078 & 0.156+j0.502 & 0.153+j0.385 \\ 0.156+j0.502 & 0.467+j1.048 & 0.158+j0.424 \\ 0.153+j0.385 & 0.158+j0.424 & 0.461+j1.065 \end{bmatrix} \ \Omega/\text{mi}$$

$$\boldsymbol{B} = j \begin{bmatrix} 5.677 & -1.832 & -0.698 \\ -1.832 & 5.981 & -1.165 \\ -0.698 & -1.165 & 5.397 \end{bmatrix} \ \mu\text{S/mi}$$

Configuration 2

$$\boldsymbol{Z} = \begin{bmatrix} 0.467+j1.048 & 0.158+j0.424 & 0.156+j0.502 \\ 0.158+j0.424 & 0.461+j1.065 & 0.153+j0.385 \\ 0.156+j0.502 & 0.153+j0.385 & 0.458+j1.078 \end{bmatrix} \ \Omega/\text{mi}$$

$$\boldsymbol{B} = j \begin{bmatrix} 5.981 & -1.165 & -1.832 \\ -1.165 & 5.397 & -0.698 \\ -1.832 & -0.698 & 5.677 \end{bmatrix} \ \mu\text{S/mi}$$

Configuration 3

$$\boldsymbol{Z} = \begin{bmatrix} 0.461{+}j1.065 & 0.153{+}j0.385 & 0.158{+}j0.424 \\ 0.153{+}j0.385 & 0.458{+}j1.078 & 0.156{+}j0.502 \\ 0.158{+}j0.424 & 0.156{+}j0.502 & 0.467{+}j1.048 \end{bmatrix} \ \Omega/\text{mi}$$

$$\boldsymbol{B} = j \begin{bmatrix} 5.397 & -0.698 & -1.165 \\ -0.698 & 5.677 & -1.832 \\ -1.165 & -1.832 & 5.981 \end{bmatrix} \ \mu\text{S/mi}$$

Configuration 4

$$\boldsymbol{Z} = \begin{bmatrix} 0.461{+}j1.065 & 0.158{+}j0.424 & 0.153{+}j0.385 \\ 0.158{+}j0.424 & 0.467{+}j1.048 & 0.156{+}j0.502 \\ 0.153{+}j0.385 & 0.156{+}j0.502 & 0.458{+}j1.078 \end{bmatrix} \ \Omega/\text{mi}$$

$$\boldsymbol{B} = j \begin{bmatrix} 5.397 & -1.165 & -0.698 \\ -1.165 & 5.981 & -1.832 \\ -0.698 & -1.832 & 5.677 \end{bmatrix} \ \mu\text{S/mi}$$

Configuration 5

$$\boldsymbol{Z} = \begin{bmatrix} 0.467{+}j1.048 & 0.156{+}j0.502 & 0.158{+}j0.424 \\ 0.156{+}j0.502 & 0.458{+}j1.078 & 0.153{+}j0.385 \\ 0.158{+}j0.424 & 0.153{+}j0.385 & 0.461{+}j1.065 \end{bmatrix} \ \Omega/\text{mi}$$

$$\boldsymbol{B} = j \begin{bmatrix} 5.981 & -1.832 & -1.165 \\ -1.832 & 5.677 & -0.698 \\ -1.165 & -0.698 & 5.397 \end{bmatrix} \ \mu\text{S/mi}$$

Configuration 6

$$\boldsymbol{Z} = \begin{bmatrix} 0.458{+}j1.078 & 0.153{+}j0.385 & 0.156{+}j0.502 \\ 0.153{+}j0.385 & 0.461{+}j1.065 & 0.158{+}j0.424 \\ 0.156{+}j0.502 & 0.158{+}j0.424 & 0.467{+}j1.048 \end{bmatrix} \ \Omega/\text{mi}$$

$$\boldsymbol{B} = j \begin{bmatrix} 5.677 & -0.698 & -1.832 \\ -0.698 & 5.397 & -1.165 \\ -1.832 & -1.165 & 5.981 \end{bmatrix} \ \mu\text{S/mi}$$

Configuration 7

$$\boldsymbol{Z} = \begin{bmatrix} 0.458{+}j1.078 & 0 & 0.153{+}j0.385 \\ 0 & 0 & 0 \\ 0.153{+}j0.385 & 0 & 0.461{+}j1.065 \end{bmatrix} \ \Omega/\text{mi}$$

$$\boldsymbol{B} = j \begin{bmatrix} 5.115 & 0 & -1.055 \\ 0 & 0 & 0 \\ -1.055 & 0 & 5.170 \end{bmatrix} \mu\text{S/mi}$$

Configuration 8

$$\boldsymbol{Z} = \begin{bmatrix} 0.458+j1.078 & 0.153+j0.385 & 0 \\ 0.153+j0.385 & 0.461+j1.065 & 0 \\ 0 & 0 & 0 \end{bmatrix} \Omega\text{/mi}$$

$$\boldsymbol{B} = j \begin{bmatrix} 5.115 & -1.055 & 0 \\ -1.055 & 5.170 & 0 \\ 0 & 0 & 0 \end{bmatrix} \mu\text{S/mi}$$

Configuration 9

$$\boldsymbol{Z} = \begin{bmatrix} 1.329+j1.347 & 0 & 0 \\ 0 & 0 & 0 \\ 0 & 0 & 0 \end{bmatrix} \Omega\text{/mi}$$

$$\boldsymbol{B} = j \begin{bmatrix} 4.519 & 0 & 0 \\ 0 & 0 & 0 \\ 0 & 0 & 0 \end{bmatrix} \mu\text{S/mi}$$

Configuration 10

$$\boldsymbol{Z} = \begin{bmatrix} 0 & 0 & 0 \\ 0 & 1.329+j1.347 & 0 \\ 0 & 0 & 0 \end{bmatrix} \Omega\text{/mi}$$

$$\boldsymbol{B} = j \begin{bmatrix} 0 & 0 & 0 \\ 0 & 4.519 & 0 \\ 0 & 0 & 0 \end{bmatrix} \mu\text{S/mi}$$

Configuration 11

$$\boldsymbol{Z} = \begin{bmatrix} 0 & 0 & 0 \\ 0 & 0 & 0 \\ 0 & 0 & 1.329+j1.347 \end{bmatrix} \Omega\text{/mi}$$

$$\boldsymbol{B} = j \begin{bmatrix} 0 & 0 & 0 \\ 0 & 0 & 0 \\ 0 & 0 & 4.519 \end{bmatrix} \mu\text{S/mi}$$

Configuration 12

$$\boldsymbol{Z} = \begin{bmatrix} 1.521{+}j0.752 & 0.520{+}j0.277 & 0.492{+}j0.216 \\ 0.520{+}j0.277 & 1.533{+}j0.716 & 0.520{+}j0.277 \\ 0.492{+}j0.216 & 0.520{+}j0.277 & 1.521{+}j0.752 \end{bmatrix} \ \Omega/\text{mi}$$

$$\boldsymbol{B} = j \begin{bmatrix} 67.030 & 0 & 0 \\ 0 & 67.030 & 0 \\ 0 & 0 & 67.030 \end{bmatrix} \ \mu\text{S/mi}$$

Configuration LXFM1

$$\boldsymbol{Z} = \begin{bmatrix} 0.011{+}j0.02 & 0 & 0 \\ 0 & 0.011{+}j0.02i & 0 \\ 0 & 0 & 0.011{+}j0.02 \end{bmatrix} \ \text{p.u.}$$

Table E.3: 123-Bus Load Data

Bus	Phases	V_{ll} [kV]	Load [kVA]	Bus	Phases	V_{ll} [kV]	Load [kVA]
1	A B C	4.16	$40+j20,\quad 0,\quad 0$	32	A B C	4.16	$40+j20,\quad 0,\quad 0$
2	B	4.16	$0,\quad 21+j11,\quad 0$	33	A B C	4.16	$0,\quad 0,\quad 40+j20$
3	C	4.16	$0,\quad 0,\quad 0$	34	A B C	4.16	$0,\quad 0,\quad 0$
4	A B C	4.16	$20+j10,\quad 0,\quad 0$	35	C	4.16	$0,\quad 0,\quad 20+j10$
5	C	4.16	$0,\quad 0,\quad 40+j20$	36	A B C	4.16	$26-j2,\quad 14+j22,\quad 0$
6	C	4.16	$0,\quad 0,\quad 20+j10$	37	A B	4.16	$0,\quad 0,\quad 0$
7	C	4.16	$0,\quad 0,\quad 40+j20$	38	A B C	4.16	$0,\quad 0,\quad 0$
8	A B C	4.16	$0,\quad 0,\quad 0$	39	A	4.16	$40+j20,\quad 0,\quad 0$
9	B	4.16	$0,\quad 21+j11,\quad 0$	40	B	4.16	$0,\quad 21+j11,\quad 0$
10	A	4.16	$40+j20,\quad 0,\quad 0$	41	B	4.16	$0,\quad 21+j11,\quad 0$
11	A B C	4.16	$0,\quad 0,\quad 0$	42	C	4.16	$0,\quad 0,\quad 20+j10$
12	A	4.16	$0,\quad 0,\quad 0$	43	A B C	4.16	$20+j10,\quad 0,\quad 0$
13	C	4.16	$0,\quad 0,\quad 40+j20$	44	B	4.16	$0,\quad 42+j21,\quad 0$
14	A B C	4.16	$0,\quad 0,\quad 0$	45	A B C	4.16	$0,\quad 0,\quad 0$
15	A	4.16	$40+j20,\quad 0,\quad 0$	46	A	4.16	$20+j10,\quad 0,\quad 0$
16	A	4.16	$20+j10,\quad 0,\quad 0$	47	A B C	4.16	$35+j25,\quad 37+j26,\quad 35+j25$
17	C	4.16	$0,\quad 0,\quad 0$	48	A	4.16	$20+j10,\quad 0,\quad 0$
18	C	4.16	$0,\quad 0,\quad 40+j20$	49	A B C	4.16	$70+j50,\quad 74+j53,\quad 70+j50$
19	C	4.16	$0,\quad 0,\quad 20+j10$	50	A B C	4.16	$35+j25,\quad 74+j53,\quad 35+j20$
20	A	4.16	$40+j20,\quad 0,\quad 0$	51	A B C	4.16	$0,\quad 0,\quad 40+j20$
21	A B C	4.16	$0,\quad 0,\quad 0$	52	A B C	4.16	$20+j10,\quad 0,\quad 0$
22	A	4.16	$40+j20,\quad 0,\quad 0$	53	A B C	4.16	$0,\quad 0,\quad 0$
23	B	4.16	$0,\quad 42+j21,\quad 0$	54	A B C	4.16	$40+j20,\quad 0,\quad 0$
24	A B C	4.16	$0,\quad 0,\quad 0$	55	A B C	4.16	$40+j20,\quad 0,\quad 0$
25	C	4.16	$0,\quad 0,\quad 40+j20$	56	A B C	4.16	$0,\quad 0,\quad 0$
26	A B C	4.16	$0,\quad 0,\quad 0$	57	A B C	4.16	$20+j10,\quad 0,\quad 0$
27	A C	4.16	$0,\quad 0,\quad 0$	58	A B C	4.16	$0,\quad 0,\quad 0$
28	A B C	4.16	$40+j20,\quad 0,\quad 0$	59	A B C	4.16	$0,\quad 21+j11,\quad 0$
29	A C	4.16	$0,\quad 0,\quad 0$	60	B	4.16	$0,\quad 21+j11,\quad 0$
30	C	4.16	$0,\quad 0,\quad 20+j10$	61	A B C	4.16	$20+j10,\quad 0,\quad 0$
31	A	4.16	$40+j20,\quad 0,\quad 0$	62	B	4.16	$0,\quad 21+j11,\quad 0$

Table E.3: 123-Bus Load Data (Continued)

Bus	Phases	V_{ll} [kV]	Load [kVA]	Bus	Phases	V_{ll} [kV]	Load [kVA]
63	A B C	4.16	$0, \quad 0, \quad 0$	93	B	4.16	$0, \quad 42 + j21, \quad 0$
64	A B C	4.16	$0, \quad 0, \quad 40 + j20$	94	A B C	4.16	$0, \quad 0, \quad 0$
65	A B C	4.16	$40 + j20, \quad 0, \quad 0$	95	C	4.16	$0, \quad 0, \quad 40 + j20$
66	A B C	4.16	$0, \quad 79 + j37, \quad 0$	96	A B C	4.16	$0, \quad 0, \quad 0$
67	A B C	4.16	$4 - j43, \quad 36 + j25, \quad 60 + j29$	97	A	4.16	$40 + j20, \quad 0, \quad 0$
68	A B C	4.16	$0, \quad 0, \quad 75 + j35$	98	A B C	4.16	$0, \quad 21 + j11, \quad 0$
69	A B C	4.16	$0, \quad 0, \quad 0$	99	B	4.16	$0, \quad 21 + j11, \quad 0$
70	A	4.16	$20 + j10, \quad 0, \quad 0$	100	A B C	4.16	$40 + j20, \quad 0, \quad 0$
71	A B C	4.16	$0, \quad 0, \quad 0$	101	A B C	4.16	$0, \quad 42 + j21, \quad 0$
72	A B C	4.16	$0, \quad 0, \quad 0$	102	A B C	4.16	$0, \quad 0, \quad 40 + j20$
73	A	4.16	$40 + j20, \quad 0, \quad 0$	103	A B C	4.16	$0, \quad 0, \quad 0$
74	A	4.16	$20 + j10, \quad 0, \quad 0$	104	A B C	4.16	$0, \quad 0, \quad 0$
75	A	4.16	$40 + j20, \quad 0, \quad 0$	105	C	4.16	$0, \quad 0, \quad 20 + j10$
76	C	4.16	$0, \quad 0, \quad 40 + j20$	106	A B C	4.16	$0, \quad 0, \quad 0$
77	A B C	4.16	$55 - j36, \quad 81 + j75, \quad 71 + j52$	107	C	4.16	$0, \quad 0, \quad 40 + j20$
78	C	4.16	$0, \quad 0, \quad 40 + j20$	108	C	4.16	$0, \quad 0, \quad 40 + j20$
79	C	4.16	$0, \quad 0, \quad 40 + j20$	109	B	4.16	$0, \quad 42 + j21, \quad 0$
80	A B C	4.16	$0, \quad 42 + j21, \quad 0$	110	A B C	4.16	$0, \quad 0, \quad 0$
81	A B C	4.16	$0, \quad 21 + j11, \quad 0$	111	B	4.16	$0, \quad 42 + j21, \quad 0$
82	A B C	4.16	$0, \quad 0, \quad 0$	112	A	4.16	$40 + j20, \quad 0, \quad 0$
83	A B C	4.16	$40 + j20, \quad 0, \quad 0$	113	A B C	4.16	$0, \quad 0, \quad 0$
84	A B C	4.16	$0, \quad 42 + j21, \quad 0$	114	A	4.16	$0, \quad 0, \quad 0$
85	A B C	4.16	$0, \quad 0, \quad 0$	115	A	4.16	$20 + j10, \quad 0, \quad 0$
86	A B C	4.16	$40 + j20, \quad 0, \quad 0$	116	A	4.16	$20 + j10, \quad 0, \quad 0$
87	C	4.16	$0, \quad 0, \quad 20 + j10$	117	A	4.16	$40 + j20, \quad 0, \quad 0$
88	A B C	4.16	$0, \quad 0, \quad 20 + j10$	118	A	4.16	$20 + j10, \quad 0, \quad 0$
89	C	4.16	$0, \quad 0, \quad 40 + j20$	119	A B C	4.16	$0, \quad 0, \quad 0$
90	A B C	4.16	$0, \quad 42 + j21, \quad 0$	120	A B C	4.16	$0, \quad 0, \quad 0$
91	A	4.16	$40 + j20, \quad 0, \quad 0$	121	A B C	0.48	$0, \quad 0, \quad 0$
92	A B C	4.16	$0, \quad 0, \quad 0$				

Table E.4: 123-Bus Distribution Line Segment Data

Line	From	To	Length [ft]	Config.	Line	From	To	Length [ft]	Config.	Line	From	To	Length [ft]	Config.
1	1	2	175	L10	41	38	43	250	L1	81	84	85	475	L6
2	1	3	250	L11	42	43	44	500	L10	82	85	86	250	L6
3	1	4	300	L1	43	43	45	200	L1	83	85	87	675	L11
4	3	5	200	L11	44	45	46	200	L9	84	86	88	250	L6
5	3	6	325	L11	45	45	47	250	L1	85	87	89	475	L11
6	6	7	250	L11	46	46	48	300	L9	86	81	90	450	L6
7	4	8	200	L1	47	47	49	150	L4	87	90	91	175	L9
8	8	9	225	L10	48	47	50	250	L4	88	90	92	275	L6
9	8	10	225	L9	49	50	51	250	L4	89	92	93	225	L10
10	8	11	300	L1	50	51	52	250	L4	90	92	94	225	L6
11	10	12	425	L9	51	52	53	750	L4	91	94	95	300	L11
12	11	13	150	L11	52	54	55	200	L1	92	94	96	225	L6
13	11	14	825	L2	53	55	56	125	L1	93	96	97	275	L9
14	12	15	250	L9	54	56	57	275	L1	94	96	98	300	L6
15	12	16	250	L9	55	56	58	350	L3	95	98	99	200	L10
16	17	18	375	L11	56	57	59	275	L1	96	72	100	275	L3
17	17	19	350	L11	57	58	60	250	L10	97	100	101	550	L3
18	14	20	250	L9	58	58	61	750	L3	98	101	102	300	L3
19	14	21	300	L2	59	60	62	250	L10	99	102	103	800	L3
20	20	22	325	L9	60	61	63	550	L5	100	104	105	225	L11
21	21	23	525	L10	61	61	64	250	L12	101	104	106	275	L3
22	21	24	250	L2	62	64	65	175	L12	102	105	107	325	L11
23	24	25	550	L11	63	65	66	350	L12	103	107	108	700	L11
24	24	26	275	L2	64	66	67	425	L12	104	106	109	225	L10
25	26	27	350	L7	65	67	68	325	L12	105	106	110	325	L3
26	26	28	200	L2	66	69	70	200	L9	106	109	111	575	L10
27	27	29	275	L7	67	69	71	275	L3	107	110	112	450	L9
28	27	30	225	L11	68	69	72	250	L3	108	110	113	1000	L3
29	29	31	500	L9	69	70	73	275	L9	109	112	114	300	L9
30	28	32	300	L2	70	73	74	325	L9	110	114	115	575	L9
31	32	33	350	L2	71	74	75	275	L9	111	114	116	125	L9
32	33	34	200	L2	72	71	76	275	L11	112	116	117	525	L9
33	30	35	300	L11	73	71	77	200	L3	113	117	118	325	L9
34	13	17	100	L11	74	76	78	350	L11	114	14	36	375	L4
35	36	37	650	L8	75	78	79	400	L11	115	119	120	100	L1
36	36	38	250	L1	76	77	80	400	L6	116	120	1	400	L1
37	37	39	300	L9	77	77	81	700	L3	117	11	54	400	L1
38	37	40	250	L10	78	80	82	100	L6	118	61	69	350	L6
39	40	41	325	L10	79	82	83	225	L6	119	72	104	250	L3
40	38	42	325	L11	80	82	84	475	L6	120	63	121	0	LXFM1

REFERENCES

[1] W. A. Wulf, "Great achievements and grand challenges," *The Bridge*, vol. 30, no. 3/4, pp. 5–10, 2010.

[2] "U.S. department of energy — smart grid," May 2013. [Online]. Available: http://www.oe.energy.gov/smartgrid.htm

[3] "European technology platform for the electricity networks of the future," 2013 May. [Online]. Available: http://www.smartgrids.eu

[4] "IEEE application guide for IEEE Std 1547, IEEE standard for interconnecting distributed resources with electric power systems," *IEEE Std. 1547.2-2008*, pp. 1–207, Apr. 2009.

[5] K. Turitsyn, P. Sulc, S. Backhaus, and M. Chertkov, "Distributed control of reactive power flow in a radial distribution circuit with high photovoltaic penetration," in *Proc. of IEEE Power and Energy Society General Meeting, 2010*, Minneapolis, MN, Jul. 2010, pp. 1–6.

[6] P. Carvalho, P. Correia, and L. Ferreira, "Distributed reactive power generation control for voltage rise mitigation in distribution networks," *IEEE Trans. Power Sys.*, vol. 23, no. 2, pp. 766–772, May 2008.

[7] W. H. Kersting, *Distribution System Modeling and Analysis*. New York, NY: CRC Press, 2001.

[8] A. Keane, L. Ochoa, E. Vittal, C. Dent, and G. Harrison, "Enhanced utilization of voltage control resources with distributed generation," *IEEE Trans. Power Sys.*, vol. 26, no. 1, pp. 252–260, Feb. 2011.

[9] S. V. Dhople, J. L. Ehlmann, C. J. Murray, S. T. Cady, and P. Chapman, "Engineering systems in the Gable home: A passive, net-zero, solar-powered house for the U. S. Department of Energy's 2009 Solar Decathlon," in *Proc. of Power and Energy Conference at Illinois, 2010*, Feb. 2010, pp. 58–62.

[10] Newell Instruments, "Equinox house," Jan. 2012. [Online]. Available: http://newellinstruments.com/equinox

[11] C. Guille and G. Gross, "A conceptual framework for the vehicle-to-grid (V2G) implementation," *Energy Policy*, vol. 37, no. 11, pp. 4379–4390, Nov. 2009.

[12] D. Schooley, Written communication from ComEd, Mar. 2011.

[13] P. W. Sauer and M. A. Pai, "A comparison of discrete vs continuous dynamic models of tap-changing-under-load transformers," in *Proc. of Bulk Power System Voltage Phenomena III: Voltage Stability, Security, and Control*, Davos, Switzerland, Aug. 1994.

[14] G. Joos, B. T. Ooi, D. McGillis, F. D. Galiana, and R. Marceau, "The potential of distributed generation to provide ancillary services," in *Proc. of 2000 IEEE Power Engineering Society Summer Meeting*, vol. 3, Jul. 2000, pp. 1762 –1767.

[15] A. D. Domínguez-García, C. N. Hadjicostis, P. T. Krein, and S. T. Cady, "Small inverter-interfaced distributed energy resources for reactive power support," in *Proc. of the IEEE Applied Power Electronics Conference and Exposition*, Fort Worth, TX, Feb. 2011, pp. 1616 –1621.

[16] Petra Solar, "SunWave Communications System," 2009, South Plainfield, NJ. [Online]. Available: http://www.petrasolar.com/

[17] SolarBridge Technologies, "Pantheon Microinverter," 2009, South Plainfield, NJ. [Online]. Available: http://www.petrasolar.com/

[18] B. A. Robbins, H. Zhu, and A. D. Domínguez-García, "Optimal tap setting of voltage regulation transformers in unbalanced distribution systems," *IEEE Trans. on Power Systems*, to appear.

[19] S. Boyd and L. Vandenberghe, *Convex Optimization*, 7th ed. New York, NY: Cambridge University Press, 2009.

[20] S. Boyd, N. Parikh, E. Chu, B. Peleato, and J. Eckstein, "Distributed optimization and statistical learning via the alternating direction method of multipliers," *Foundations and Trends in Machine Learning*, vol. 3, no. 1, pp. 1–122, 2011.

[21] M. E. Baran and I. M. El-Markabi, "A multiagent-based dispatching scheme for distributed generators for voltage support on distribution feeders," *IEEE Trans. Power Sys.*, vol. 22, no. 1, pp. 52–59, Feb. 2007.

[22] K. Rogers, R. Klump, H. Khurana, A. Aquino-Lugo, and T. Overbye, "An authenticated control framework for distributed voltage support on the smart grid," *IEEE Trans. Smart Grid*, vol. 1, no. 1, pp. 40–47, Jun. 2010.

[23] D. Villacci, G. Bontempi, and A. Vaccaro, "An adaptive local learning-based methodology for voltage regulation in distribution networks with dispersed generation," *IEEE Trans. Power Sys.*, vol. 21, no. 3, pp. 1131–1140, Aug. 2006.

[24] M. Farivar and S. H. Low, "Branch flow model: Relaxations and convexification," *IEEE Trans. on Power Systems*, vol. 28, no. 3, pp. 2554–2564, Aug. 2013.

[25] K. Turitsyn, P. Šulc, S. Backhaus, and M. Chertkov, "Distributed control of reactive power flow in a radial distribution circuit with high photovoltaic penetration," in *Proc. of IEEE Power and Energy Society General Meeting*, Jul. 2010, pp. 1–6.

[26] P. Šulc, S. Backhaus, and M. Chertkov, "Optimal distributed control of reactive power via the alternating direction method of multipliers," *IEEE Trans. on Energy Conversion*, vol. 29, no. 4, pp. 968–977, Dec. 2014.

[27] L. Gan and S. H. Low, "Convex relaxations and linear approximation for optimal power flow in multiphase radial networks," [Available]: arXiv:1406.3054, Jun. 2014.

[28] J. Lavaei and S. H. Low, "Zero duality gap in optimal power flow problem," *IEEE Trans. on Power Systems*, vol. 27, no. 1, pp. 92–107, 2012.

[29] B. Zhang, A. Lam, A. Domínguez-García, and D. Tse, "An optimal and distributed method for voltage regulation in power distribution systems," *IEEE Trans. on Power Systems*, to appear.

[30] E. Dall'Anese, S. Dhople, and G. B. Giannakis, "Optimal dispatch of photovoltaic inverters in residential distribution systems," *IEEE Trans. on Sustainable Energy*, vol. 5, no. 2, pp. 487–497, Apr. 2014.

[31] J. Lavaei, D. Tse, and B. Zhang, "Geometry of power flows in tree networks," in *Proc. of IEEE Power and Energy Society General Meeting*, 2012, pp. 1–8.

[32] S. Bose, D. F. Gayme, S. H. Low, and K. M. Chandy, "Optimal power flow over tree networks," in *Proc. of Allerton Conf. on Comm., Control, & Computing*, 2011, pp. 1342–1348.

[33] Q. Peng and S. H. Low, "Distributed algorithm for optimal power flow on a radial network," [Available]: arXiv:1404.0700, Apr. 2014.

[34] P. Vovos, A. Kiprakis, A. Wallace, and G. Harrison, "Centralized and distributed voltage control: Impact on distributed generation penetration," *IEEE Trans. Power Sys.*, vol. 22, no. 1, pp. 476–483, Feb. 2007.

[35] T. Sansawatt, J. O'Donnell, L. F. Ochoa, and G. P. Harrison, "Decentralised voltage control for active distribution networks," in *Proc. of the 44th International Universities Power Engineering Conference (UPEC)*, Sept. 2009, pp. 1–5.

[36] B. A. Robbins, C. N. Hadjicostis, and A. D. Dominguez-Garcia, "A two-stage distributed architecture for voltage control in power distribution systems," *IEEE Trans. on Power Systems*, vol. 28, no. 2, pp. 1470–1482, May 2013.

[37] B. Zhang, A. D. Domínguez-García, and D. Tse, "A local control approach to voltage regulation in distribution networks," in *Proc. of North American Power Symposium*, Sep. 2013, pp. 1–6.

[38] B. A. Robbins, H. Zhu, and A. D. Domínguez-García, "Distributed and resilient voltage control in power distribution networks," ABB, Tech. Rep., 2014.

[39] B. A. Robbins, K. E. Van Horn, and A. D. Domínguez-García, "Policies and implementation of a two time-scale approach for regulation in unbalanced distribution systems," In preparation for journal publication.

[40] B. A. Robbins, H. Zhu, and A. D. Dominguez-Garcia, "Optimal tap settings for voltage regulation transformers in distribution networks," in *Proc. of North American Power Symposium (NAPS)*, 2013, pp. 1–6.

[41] B. A. Robbins and A. D. Domínguez-García, "Optimal reactive power dispatch for voltage tracking in unbalanced distribution systems," submitted, 2015.

[42] B. A. Robbins, A. D. Dominguez-Garcia, and C. N. Hadjicostis, "Control of distributed energy resources for reactive power support," in *Proc. of 2011 North American Power Symposium (NAPS)*, 2011, pp. 1–5.

[43] B. Zhang, "Control and optimization of power systems with renewables: Voltage regulation and generator dispatch," Ph.D. dissertation, University of California at Berkeley, Aug. 2013.

[44] M. Farivar, C. R. Clarke, S. H. Low, and K. M. Chandy, "Inverter var control for distribution systems with renewables," in *Proc. of IEEE Conf. on Smart Grid Communications*, Oct. 2011, pp. 457–462.

[45] A. D. Dominguez-Garcia and C. N. Hadjicostis, "Coordination and control of distributed energy resources for provision of ancillary services," in *Proc. of IEEE International Conference on Smart Grid Communications*, Gaithersburg, MD, Oct. 2010, pp. 537–542.

[46] B. A. Robbins, A. D. Dominguez-Garcia, and C. N. Hadjicostis, "Control of distributed energy resources for reactive power support," in *Proc. of North American Power Symposium*, Boston, MA, Aug. 2011.

[47] W. H. Kersting, *Distribution System Modeling and Analysis.* New York, NY: CRC Press, 2001.

[48] P. W. Sauer and M. A. Pai, "A comparison of discrete vs continuous dynamic models of tap-changing-under-load transformers," in *Proc. Bulk Power System Voltage Phenomena III: Voltage Stability, Security, & Control*, Davos, Switzerland, Aug 1994.

[49] W.-H. E. Liu, A. D. Papalexopoulos, and W. F. Tinney, "Discrete shunt controls in a Newton optimal power flow," *IEEE Trans. on Power Systems*, vol. 7, no. 4, pp. 1509–1518, 1992.

[50] E. Acha, H. Ambriz-Perez, and C. R. Fuerte-Esquivel, "Advanced transformer control modeling in an optimal power flow using Newton's method," *IEEE Trans. on Power Systems*, vol. 15, no. 1, pp. 290–298, 2000.

[51] M. M. Adibi, R. A. Polyak, I. A. Griva, L. Mili, and S. Ammari, "Optimal transformer tap selection using modified barrier-augmented lagrangian method," in *Proc. IEEE Power Engineering Society General Meeting*, vol. 2, 2003.

[52] E. Dall'Anese, H. Zhu, and G. Giannakis, "Distributed optimal power flow for smart microgrids," *IEEE Trans. on Smart Grid*, vol. 4, no. 3, pp. 1464–1475, Sep. 2013.

[53] R. A. Jabr, "Optimal power flow using an extended conic quadratic formulation," *IEEE Trans. on Power Systems*, vol. 23, no. 3, pp. 1000–1008, Aug. 2008.

[54] J. Lavaei, "Zero duality gap for classical opf problem convexifies fundamental nonlinear power problems," in *Proc. American Control Conference (ACC)*, 2011, pp. 4566–4573.

[55] J. Lavaei and S. H. Low, "Convexification of optimal power flow problem," in *Proc. of Allerton Conf. on Communication, Control, & Computing*, 2010, pp. 223–232.

[56] M. Kraning, E. Chu, J. Lavaei, and S. Boyd, "Dynamic network energy management via proximal message passing," *Foundations and Trends in Optimization*, vol. 1, no. 2, pp. 1–54, 2013.

[57] H. Zhu and G. B. Giannakis, "Multi-area state estimation using distributed SDP for nonlinear power systems," in *Proc. of IEEE Conference on Smart Grid Communications*, Nov. 2012, pp. 623–628.

[58] IEEE Power and Energy Society, "Distribution test feeders," Sep. 2010. [Online]. Available: http://www.ewh.ieee.org/soc/pes/dsacom/testfeeders/index.html

[59] Y. Ye, "Linear conic programming," Dec. 2004, Stanford MS&E314/CME336 Course Notes.

[60] S. Boyd, "CVX: Matlab software for disciplined convex programming," Mar. 2014. [Online]. Available: http://cvxr.com/cvx/

[61] CORAL Lab, "Sedumi," Mar. 2014. [Online]. Available: http://sedumi.ie.lehigh.edu

[62] R. Olfati-Saber, J. A. Fax, and R. M. Murray, "Consensus and cooperation in networked multi-agent systems," *Proc. of the IEEE*, vol. 95, no. 1, pp. 215 –233, Jan. 2007.

[63] A. Bergen and V. Vittal, *Power System Analysis*. Upper Saddle River, NJ: Prentice Hall, 2000.

[64] E. D. Sontag, "On the input-to-state stability property," *Systems & Control Letters*, vol. 24, pp. 351–359, 1995.

[65] R. A. Horn and C. R. Johnson, *Matrix Analysis*, 23rd ed. New York, NY: Cambridge University Press, 2010.

[66] A. D. Domínguez-García and C. N. Hadjicostis, "Distributed algorithms for control of demand response and distributed energy resources," in *Proc. of the IEEE Control and Decision Conference*, Orlando, FL, Dec. 2011.

[67] C. Godsil and G. Royle, *Algebraic Graph Theory*. New York, NY: Springer, 2001.

[68] S. T. Cady, A. D. Domínguez-García, and C. N. Hadjicostis, "Robust implementation of distributed algorithms for control of distributed energy resources," in *Proc. of North American Power Symposium*, Boston, MA, Aug. 2011.

[69] M. Baran and F. Wu, "Optimal capacitor placement on radial distribution systems," *IEEE Trans. on Power Delivery*, vol. 4, no. 1, pp. 725–734, Jan. 1989.

[70] M. Baran and F. Wu, "Optimal sizing of capacitors placed on a radial distribution system," *IEEE Trans. on Power Delivery*, vol. 4, no. 1, pp. 735–743, Jan. 1989.

[71] D. Wang, K. Turitsyn, and M. Chertkov, "Distflow ode: Modeling, analyzing and controlling long distribution feeder," in *Proc. of IEEE Conf. on Decision and Control (CDC)*, Dec. 2012, pp. 5613–5618.

[72] Energy Information Agency, Jan. 2012. [Online]. Available: http://www.eia.gov/electricity/data.cfm

[73] S. Speer, "Residential solar photovoltaics: Comparison of financing benefits, innovations, and options," NREL, Tech. Rep. NREL/TP-6A20-51644, Oct. 2012.

[74] "Hawaiian electric," Feb. 2015. [Online]. Available: http://www.hawaiianelectric.com/

[75] "Tesla motors," Feb. 2015. [Online]. Available: http://www.teslamotors.com/support/model-s-specifications

[76] "BMW USA," Feb. 2015. [Online]. Available: http://www.bmwusa.com

[77] "Nissan USA," Feb. 2015. [Online]. Available: http://www.nissanusa.com/electric-cars/leaf/

[78] "Toyota," Feb. 2015. [Online]. Available: http://www.toyota.com/prius-plug-in-hybrid/

[79] "Ford," Feb. 2015. [Online]. Available: http://www.ford.com/

[80] "Chevrolet," 2015.

[81] H. Committee, "SAE electric vehicle and plug in hybrid electric vehicle conductive charge coupler," SAE, Tech. Rep. j1772_201210, Oct. 2012.

[82] T. Becker, "Electric vehicles in the united states a new model with forecasts to 2030," University of California, Berkeley, Tech. Rep. 2009.1.v.2.0, Aug. 2009.

[83] "Commercial and residential hourly load profiles for all TMY3 locations in the united states," Jul. 2013. [Online]. Available: http://en.openei.org/doe-opendata/dataset/

[84] "CONFRRM solar energy resource data," Jan. 2000. [Online]. Available: http://rredc.nrel.gov/solar/new_data/confrrm/